DEVELOPMENT OF A SPLIT HOPKINSON TENSION BAR FOR TESTING

STRESS-STRAIN RESPONSE OF PARTICULATE COMPOSITES

UNDER HIGH RATES OF LOADING

Except where reference is made to the work of others, the work described in this thesis is my own or was done in collaboration with my advisory committee. This thesis does not include proprietary or classified information.

_____
Anthony Taylor Owens

Certificate of Approval:

_____   _____
Jeffrey C. Suhling   Hareesh V. Tippur, Chair
Quina Professor   Alumni Professor
Mechanical Engineering   Mechanical Engineering

_____   _____
Bart Prorok   Joe F. Pittman
Assistant Professor   Interim Dean
Materials Engineering   Graduate School

DEVELOPMENT OF A SPLIT HOPKINSON TENSION BAR FOR TESTING

STRESS-STRAIN RESPONSE OF PARTICULATE COMPOSITES

UNDER HIGH RATES OF LOADING

Anthony Taylor Owens

A Thesis

Submitted to

the Graduate Faculty of

Auburn University

in Partial Fulfillment of the

Requirements for the

Degree of

Master of Science

Auburn, Alabama
August 4, 2007

DEVELOPMENT OF A SPLIT HOPKINSON TENSION BAR FOR TESTING

STRESS-STRAIN RESPONSE OF PARTICULATE COMPOSITES

UNDER HIGH RATES OF LOADING

Anthony Taylor Owens

_____
Signature of Author

_____
Date of Graduation

VITA

Anthony Taylor Owens was born the son of Anthony Fred Owens and Jane St. John Owens on November 10, 1980. He graduated from Guntersville High School in Guntersville, AL in 1999, ranking 4th out of his graduating class of 83. After attending Snead State Community College in Boaz, AL for one year, he transferred to Auburn University in August of 2000. In August of 2004, he graduated magna cum laude with a Bachelor of Mechanical Engineering degree from Auburn University. Upon graduation, he entered graduate school at Auburn University to pursue his Master of Science degree in the field of Mechanical Engineering.

THESIS ABSTRACT

DEVELOPMENT OF A SPLIT HOPKINSON TENSION BAR FOR TESTING

STRESS-STRAIN RESPONSE OF PARTICULATE COMPOSITES

UNDER HIGH RATES OF LOADING

Anthony Taylor Owens

Master of Science, August 4, 2007
(B.S., Auburn University, 2004)

145 Typed Pages

Directed by Hareesh V. Tippur

Mechanical structures and their material constituents undergo an expansive range of loading conditions. Specifically, the rate at which the loading takes place can vary from being virtually static to being almost instantaneous. This presents an interesting and challenging problem of understanding the way a material will respond to various loading rates. In terms of mechanical behavior, it has been observed that the stress-strain response is elementally linked to this variation in loading rates. Due to this, it is imperative that the response for a particular material be known for the loading rates it will experience in service. Over the last half century, many investigators have studied this effect for different materials under compressive high strain rate loading conditions. In more recent decades, this research area has been extended to study the responses of materials in tension and in shear.

One class of materials, particulate composites, is of specific interest in this research. Particulate composites have become progressively more popular in recent years, finding applications ranging from aerospace to electronics. Much research has been focused on studying their dynamic stress-strain behavior in compression. However, these materials are often employed under conditions that require an understanding of their dynamic tensile behavior. For instance, material fracture can often be driven by local maximum tensile stresses.

The focus of this work is thus to design a split Hopkinson tension bar to be used for studying the dynamic tensile behavior of polymers and polymer-matrix particulate composites. This apparatus is designed using finite element analysis coupled with experimentation. A mechanism capable of producing a square loading pulse and transferring that loading pulse into the test specimens is developed. A data acquisition and post processing system is devised to capture and analyze the necessary data. A series of tests is then completed to demonstrate the validity and repeatability of the results. Next, the effect of filler particle diameter and filler volume fraction on dynamic tensile stress-strain response is investigated. The results from the filler volume fraction study are compared with those from predictions and various empirical models. Finally, a brief study of the effects of loading rate on a commercially available polymer biocement is undertaken. In general, the polymers and filled-polymer composites exhibit a stiffer response under the dynamic conditions. The dynamic material strength is typically higher than its quasi-static counterpart. Often, there is a reduction in strain at failure for the dynamic loads. All of these items are quantified in the present work.

ACKNOWLEDGEMENTS

Most of all, I want to thank Jesus Christ, my Lord and Savior. He is the source of my joy and my hope. "I can do all things through Christ who gives me strength," Philippians 4:13.

Style manual or journal used Discrete Mathematics (together with the style known as "auphd"). Bibliography follows van Leunen's *A Handbook for Scholars.*

Computer software used The document preparation package Microsoft Word 2002. Microsoft Excel 2002 was used for preparing the graphs.

TABLE OF CONTENTS

LIST OF FIGURES

LIST OF TABLES

CHAPTER 1

INTRODUCTION

1.1   Background of the problem

In many circumstances, materials are subjected to loads that are highly transient in nature. These dynamic loads can produce a wide range of mechanical responses. Possibly one of the most illustrative examples of loading rate effects can be seen in Silly Putty®. This material will undergo large displacements under slowly acting forces such as gravitational pull; however, when impacted with a hard item, it will maintain its shape as if it is an elastic object. Many engineering materials exhibit this behavior to some extent. Researchers as early as the early 20th century have demonstrated that material behavior is fundamentally linked to the rate at which the material is loaded. The loading rate, commonly identified in terms of strain rate, can have a wide range of effects on critical material properties such as elastic modulus, yield stress, failure stress, and failure strain.

Gray [1] outlined several specific examples where materials are employed under high strain rate conditions. Automotive crashworthiness is one such example. Several areas of the vehicle are designed to function as energy absorbing mechanisms in the event of a crash, such that the decelerations seen by the driver are not so harsh that they cause

severe bodily injury. Even though the body is constrained by a harness, the head and neck of the driver is still susceptible to injury. In order to design structures that will absorb energy properly, the material behavior must be understood and characterized for conditions similar to the actual loading conditions.

Figure 1.1: Possible scenarios where materials encounter high strain rate conditions

The second group of examples is in the aerospace industry. Often, spacecraft or other orbital bodies come into contact with foreign debris that may be traveling at high relative velocities. Also, jet engines, which have extremely high operating speeds, may ingest foreign objects, causing severe shock loads. Containment of debris in the event of

catastrophic engine failure is another issue in jet engine design that involves highly transient loading. In some cases, fragments have pierced the engine casing and severely damaged hydraulic components that are vital for aircraft control.

Other examples include turbine blade design where cavitation is a concern, protective armor in defense applications, as well as ballistic devices where propellants and explosives interact with casings. There are many more real life applications where materials are deployed and expected to perform under high strain rate conditions.

1.2   Composite materials

The primary group of materials that is of interest in this particular work is composite materials. Jones [2] identifies a composite material as one that is created by combining two or more different materials on a macroscopic scale. He also classifies these into four major types: fibrous, laminate, particulate, and combinations. One of the most archaic forms of composite materials is recorded in the book of Exodus in the Bible when the Israelites were forced to make bricks without straw. The straw was used as a second phase material to enhance the properties of the clay bricks.

Fibrous composites consist of fibers embedded in a matrix. The working principle of this type is that a fiber or whisker that has extremely high strength and stiffness is embedded in a matrix of some other material that serves to both protect the fibers as well as transfer loads between the fibers. Fiber types include glass, carbon, and boron, as well as others. The resultant material usually has high strength and stiffness derived from the fibers and low density derived from the matrix.

Laminate composites are basically layers of certain materials combined to create one material. An example is clad metals, such as copper clad aluminum wire. Formica is another form of laminate, where kraft paper is layered and impregnated with a phenolic resin. Plywood is also a laminate where several plies of wood veneer are glued together. The grain direction is altered with each layer to enhance the strength of the overall laminate.

Particulate composites are a third type of composite material where some type of particle or aggregate, which may be metallic or nonmetallic, is embedded in either a metallic or nonmetallic matrix. Syntactic foams are one common type of particulate composite where hollow glass microspheres are embedded in a polymer. These materials exhibit excellent compressive properties for undersea applications, and their density and thermal properties make them attractive for certain aerospace and military applications. The automotive industry also uses many types of filled plastic, such as particle reinforced acrylonitrile butadiene styrene (ABS).

Figure 1.2: Example of an autonomous underwater vehicle with syntactic foam structural and buoyancy applications

The electronics industry often makes use of particle-filled composites as underfill materials. In this case, ball grid arrays, chip scale packages, and flip chip on board assemblies use epoxies filled with silica or some other type of particle to improve reliability as well as to provide environmental protection for solder joints. These materials may be used to carry mechanical loads as well as to enhance the thermal performance.
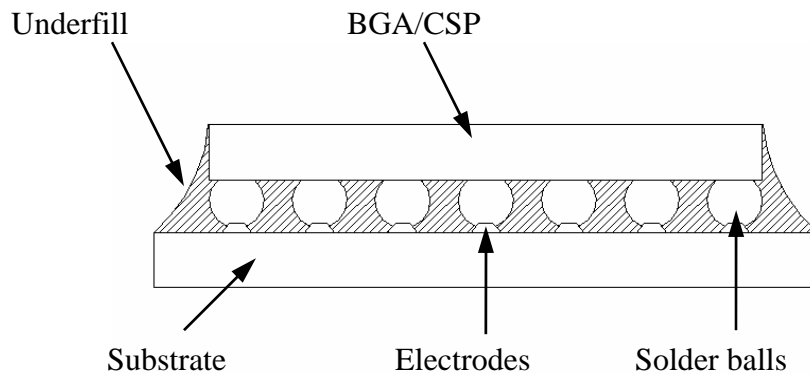
Figure 1.3: Schematic of underfill in an electronic package
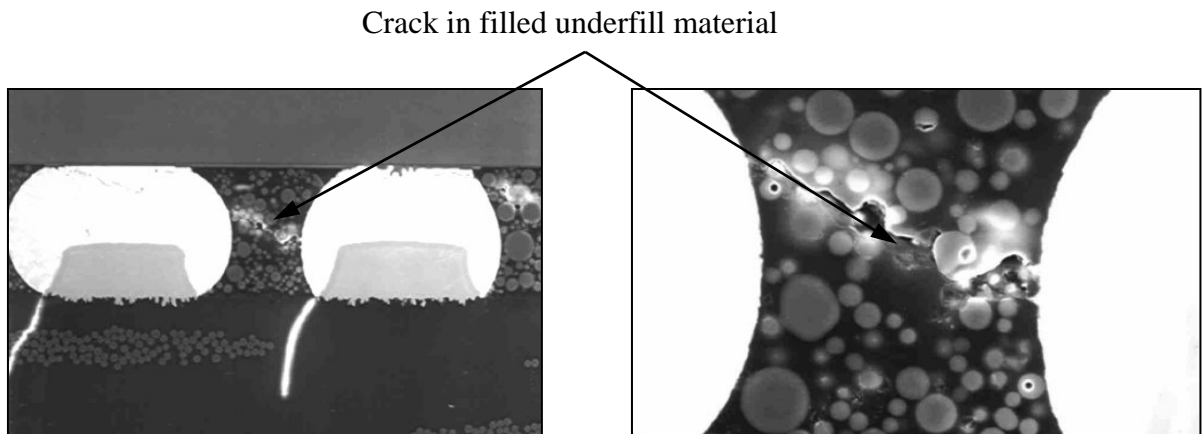
Figure 1.4: Failure in particle-filled underfill material

1.3   Motivation and objectives

There have been many techniques developed for studying dynamic material behavior. A great deal of research has been carried out in the area of compressive stress-strain response under dynamic loading, and a less amount of research work has been conducted in the area of tensile and shear material responses under high strain rate conditions.

For certain types of materials, there is a great deal of difference between the tensile and compressive behaviors. Concrete is an excellent example of a particulate composite whose performance in compression is far superior to that in tension. In terms of polymers, Chen [3] did a comparative study of two polymers under both tension and compression at high strain rates. The results showed significantly different responses under the two types of loading. For instance, the poly(methyl methacrylate) used in the tests failed at approximately 0.11 true strain and 120 MPa true stress under compression and failed at approximately 0.03 true strain and 75 MPa true stress under tension. This difference in material response coupled with the fact that fractures are most easily driven by local tensile stresses demands that there be a better understanding of the tensile stress-strain response. In terms of specific materials, a recent work by Kitey [4,5] has indicated significant loading rate effects on fracture characteristics of glass-filled epoxy particulate composites. The research shows that under dynamic loading conditions, the mean particle size has a considerable effect on the fracture toughness.

The objective of this work is thus to design an apparatus for testing materials in tension and demonstrate its capabilities by studying the stress strain behavior for different

materials under dynamic loading conditions. A set of benchmarking experiments are done using a popular commercially available epoxy system. The effect of glass particle volume fraction on filled epoxies is then investigated.

1.4　Literature review

1.4.1　General split Hopkinson bar testing

Many techniques have been devised in attempts to study material behavior at high rates of loading. Of these, the split Hopkinson pressure bar (SHPB) technique is probably the most prominent. The concept behind the mechanism was initially introduced by Bertram Hopkinson [6] in 1914. Hopkinson developed a method to measure the pressure produced by a blow such as that produced by a bullet or the detonation of an explosive.
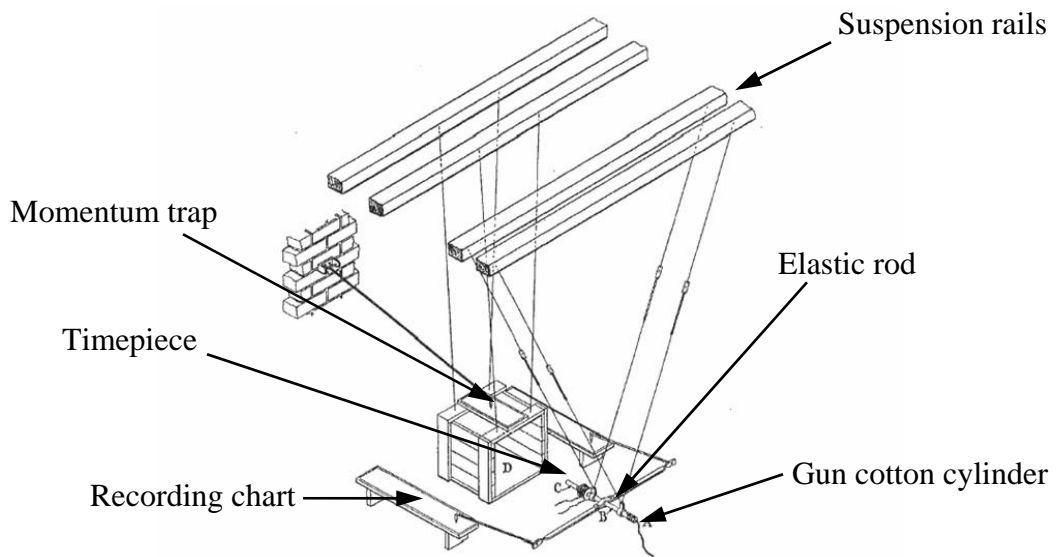
Figure 1.5: Setup used by Hopkinson

In his experiment, a bar was suspended ballistically as shown in Fig. 1.5. A detonation event occurred at one end of the bar and at the other end of the bar was a timepiece (a short cylinder). The timepiece was attached to the end of the bar with a small magnetic field, just enough to keep it from detaching. When the detonation occurred, the compressive pressure wave traveled the length of the bar and passed into the timepiece. At the free end of the timepiece, the wave reflected as a tensile wave, and as it reached back to the interface between the timepiece and the bar, it caused the timepiece to separate and fly into a momentum trapping mechanism. The energy recorded by the momentum trap corresponded to the amount of energy in a section of pulse which is twice as long as the wave transit time in the timepiece. By varying the length of the timepiece, the energy associated with the pressure wave could be related to time.

The work done by Hopkinson was revisited by Robertson [7] in 1921 and later by Landon and Quinney [8] in 1923. Eventually in 1948, Davies [9] modified the technique to use condensers for measuring the displacements in the pressure bar. These could be related to the pressures in the explosion given that the elastic limit of the bar was not exceeded. This advancement made significant improvement in the certainties of the pressure histories.

In 1948, Kolsky [10] added a second pressure bar to the setup. Between two bars, he sandwiched a thin specimen. On the input bar, he used a cylindrical condenser microphone to measure the amplitude of the pressure pulse produced by firing a detonator at the free end of the input bar. The schematic of the setup is shown in Fig. 1.6.
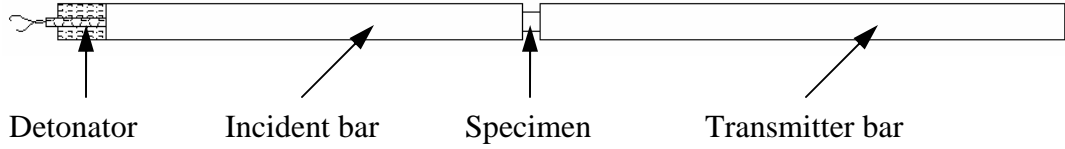
Figure 1.6: Schematic of Kolsky's setup

On the free end of the second bar, a parallel plate condenser microphone was used to measure the displacement. This could then be related to the pressure observed by the specimen. Using the signals from the two condensers, the stress-strain behavior could be obtained for different materials. This would become known as the Kolsky bar or more commonly as the split Hopkinson pressure bar (SHPB). Later the detonator was replaced by a striker bar as shown in Fig. 1.7. As will be shown later in this thesis, for a striker bar of length, *L*, and bar wave speed, C_0, the duration of the loading pulse will be $t = \dfrac{2L}{C_0}$.
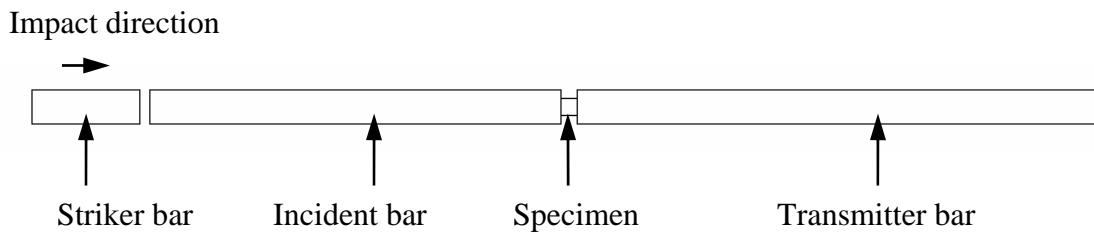
Figure 1.7: Typical split Hopkinson pressure bar setup

In addition to the introduction of a technique to study strain rate effects, several other notable works were completed that aided in the understanding of wave propagation for cylindrical bars. Pochhammer [11] and Chree [12] independently studied the

9

equations governing axial vibrations in bars in 1876 and 1889 respectively. These equations were later presented by Love [13] in 1927, and solved numerically by Bancroft [14] in 1941. Bancroft plotted the ratio of actual wave speed to bar wave speed as a function of the ratio of wavelength to bar diameter, where bar wave speed is the speed at which a wave of minimum frequency propagates. This gave a better idea as to how higher frequency, lower wavelength waves travel slower and result in dispersion. More attention is given to this later in this thesis. Davies [9] also studied the effect of distortion of a pulse due to propagation and under what conditions these distortions become too severe to yield accurate results.

1.4.2 Tension split Hopkinson bar testing

Since Kolsky's addition of the second bar to the setup, many different configurations have been used to study compression, tension, and shear behaviors of materials. This section highlights some of the setups used specifically for studying the tensile behavior. These devices are commonly called split Hopkinson tension bars or SHTB.

Several mechanisms were developed initially including those by Harding *et al.* [18] which could apply loads in very short time durations. However, Lindholm and Yeakley [16] were possibly the first to publish any work in the open literature where a modified SHPB setup was used to study materials in tension. Their setup utilized a "hat" type specimen sandwiched between a solid incident bar and a tubular transmitter bar as

shown in Fig. 1.8. The loading wave was generated in the same way as that of the compression SHPB. They used this setup to study aluminum.
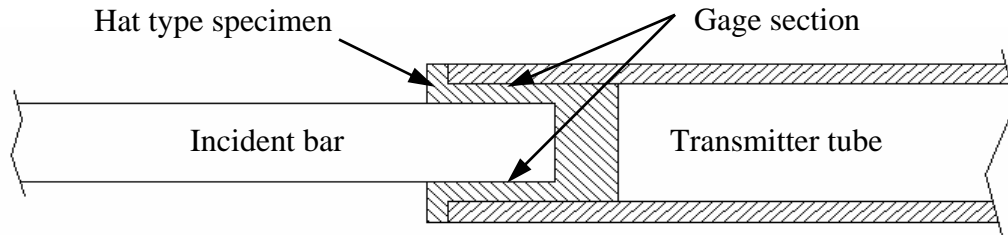
Figure 1.8: Schematic of setup used by Lindholm and Yeakley [16]

Another technique was developed by Nicholas [17] who used a threaded specimen placed in between the two bars (Fig. 1.9). A compression collar was placed around the specimen, and the threads were tightened until the collar was slightly preloaded. The wave was generated by a compressive impact and first passed through the collar as a compressive wave, leaving the specimen unloaded initially. At the end of the transmitter bar, the wave reflected as a tensile wave. The compression collar, being unable to resist the tensile wave, allowed the specimen to be loaded in tension.
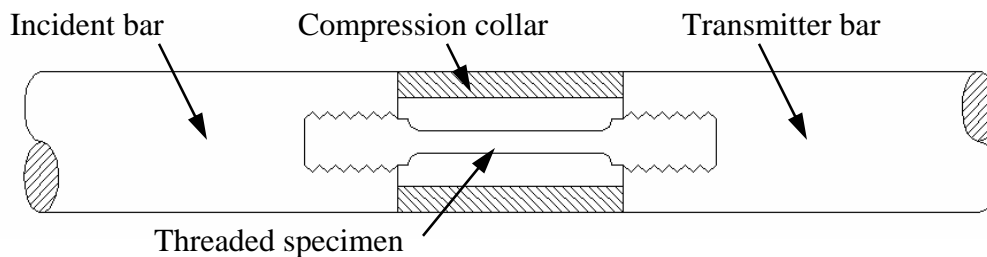
Figure 1.9: Schematic of setup used by Nicholas [17]

Harding and Welsh [15] developed a setup for testing fiber-reinforced composites at high rates of strain. Their mechanism (Fig. 1.10) used a weighbar tube striking a yoke and input bar which loaded the specimen. Strain gages were used to record incident and transmitted strains.

Inertia bar   Input bar

Weighbar tube   Specimen   Yoke
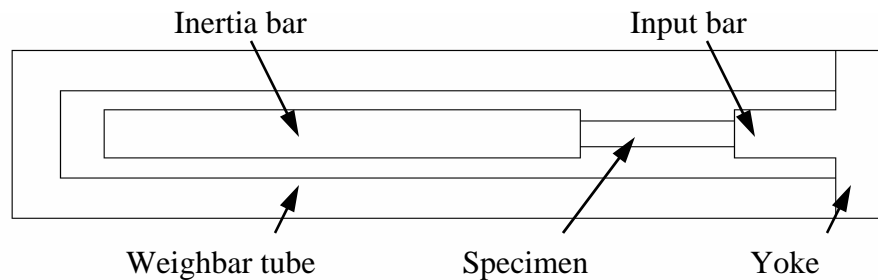
Figure 1.10: Schematic of setup used by Harding and Welsh [15]

Another setup, used by Staab and Gilat [19], used a clamping mechanism to store energy in the incident bar. A clamp was placed on the bar at some distance from the end opposite the specimen. A static tensile load was applied to the end, and as the clamp was released, the tensile stress wave propagated towards the specimen. By using a fracture pin, the clamp could be released almost instantaneously. In the setups prior to this one, the length of time of the loading pulse was dependant on the length of the striker bar (Fig. 1.7). This setup had an added advantage that the length of the loading pulse is related to the length of the bar where the energy is initially stored. Thus, by placing the clamp farther away from the load application point, the time duration of the pulse could be varied. For the setup used by Staab and Gilat, loading pulses could be produced in excess

of 500 microseconds. Previous setups had only produced loading pulses in the range of 100-200 microseconds.
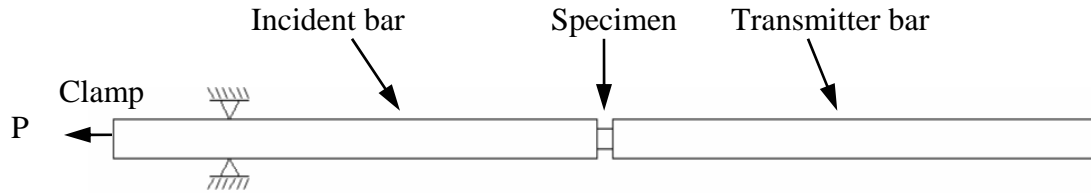
Figure 1.11: Schematic of setup used by Staab and Gilat [19]

Researchers have also used hollow bullets to produce a tensile stress wave. Ogawa [20] used one such setup to study the impact-tension-compression behavior of pure irons. In these setups, the incident bar had some type of an anvil on the impacting end. A cylinder traveled along the incident bar and contacted the anvil as shown in the Fig. 1.12. The impact resulted in a tensile pressure pulse in the incident bar loading the specimen to failure.
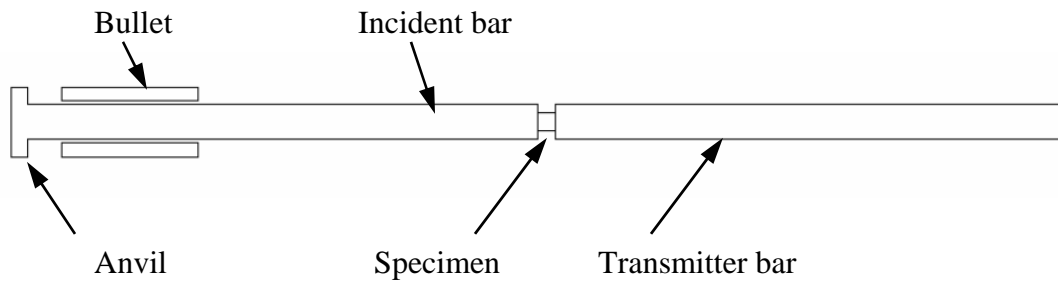
Figure 1.12: Schematic of hollow bullet configuration

The previously mentioned setups are just a sampling of the basic types of setups typically used in SHTB testing. Many variations of these configurations have been derived and used in the last few decades. The advent of high speed data acquisition techniques as well as the introduction of resistance strain gages, quartz and piezoelectric transducers, as well as other high frequency response measurement systems has opened up many doors for testing of dynamic stress-strain response.

1.4.3   Research related to polymers and polymer-matrix particulate composites

The materials of interest in this work are either solid polymers or polymer-matrix composites. In this area, much research has been done in terms of material behavior. This section seeks to outline some of the research that has been done in terms of dynamic tension and compression behavior.

The dynamic compressive behavior of specific syntactic foams was studied using the split Hopkinson pressure bar [21,22]. In these two works, both the lateral confinement effects and the temperature effects were studied for epoxy syntactic foam. They observed that under confinement, the behavior was elastic-plastic-like with a higher modulus of elasticity and yield strength. But under uniaxial stress loading, the behavior was elastic-brittle. The energy absorption capability under lateral confinement was much higher due to the elastic-plastic nature of the response. They also studied both adiabatic temperature rise as well as environmental temperature effects. While the adiabatic temperature rise was negligible, the environmental temperature effects produced a very complex effect on the foam.

Chen *et al.* [3] compared two polymers under tensile and compressive dynamic loading. They observed that under quasi-static loading, the materials exhibited similar material properties in tension and compression. However, there were significant differences between tension and compression in the material responses under dynamic conditions. For the dynamic tests, the specimens generally reached higher peak stresses than they did in the static case. In the static tensile case, the specimens failed in a ductile manner, but in dynamic tension, they failed in a brittle manner. Their work demonstrated that the dynamic compressive behavior is not indicative of the dynamic tensile behavior.

Buckley [23] also studied thermosetting polymers under compression and tension. This work commented on the difficulties associated with dynamic tensile testing and noted on the variability of the results. While the compression tests were very repeatable, the results of the dynamic tension tests proved to have a lot of scatter.

Others [24] used thermosetting polymers to demonstrate that there is an upper limit in constant strain rate testing. They used an analytical approach to estimate the upper limit for constant strain rate testing for different materials. Depending on the elastic modulus, density, and specimen geometry, some time is required for equilibration. If the specimen reaches a failure strain before it has time to equilibrate, the test will not be valid. Also, if the loading pulse has not reached steady state by the time the failure strain is reached, the test will not be under constant strain rate. Their experiments showed that for PMMA, the upper limit was about 1910 s^{-1} and for the S-2 Glass/SC15 composite that they tested, the upper limit was about 1600-1700 s^{-1}.

A device was also developed by Shim *et al.* [25] to study polymeric materials whose failure strains were too large to be reached with a conventional split Hopkinson

bar. The device basically applied two tensile loads, one after the other, to create enough strain to fail the specimen. The device was used to test the polycarbonate material Lexan®. They were able to show that the polycarbonate exhibited properties that were almost identical for both static and dynamic loading conditions.

1.5   Organization of the thesis

Including the present, this thesis contains six chapters. The first chapter introduces the problem, identifies materials of interest, and reviews previous works done by other researchers. The second chapter presents the development details of the actual apparatus. The design of the projectile launching mechanism is discussed. Several iterations of the impact mechanism are detailed. Then, issues associated with the specimen bar interfaces are addressed. The third chapter outlines the data collection and reduction process. First, the equations necessary for data reduction are derived. Secondly, the details of data acquisition are discussed. Finally, the full details of how the raw data are converted into stress-strain responses are shown. The fourth chapter outlines some preliminary results and demonstrates the validity and repeatability of the setup. The fifth chapter discusses results obtained from the apparatus. The results are shown of a brief study to investigate the effect of glass particle reinforcement in the matrix, including the effect of filler volume fraction as well as the effect of mean filler particle diameter. The sixth chapter concludes by summarizing the results and making suggestions for future directions of the research. Finally, three appendices are included. The first shows the MATLAB® and LabVIEW® codes used for data acquisition and post

processing. The second lists the procedure for conducting an experiment. The third outlines the preliminary development of another dynamic test method which motivated the current research.

CHAPTER 2

DESIGN OF THE APPARATUS

2.1   Introduction

Out of the several different methods previously used in SHTB testing, the hollow striker approach was chosen for this work. For the present work, a previously existing gas gun was available in the lab that could be adapted.   The details involved in developing the SHTB are discussed in this chapter.

2.1.1   Overview of the final setup

For reference purposes, a brief overview of the final design is given. The final setup consists of 12.7 mm diameter incident and transmitter bars machined from 7075-T6 aluminum. Both bars are 2.4 m in length. A dovetail is machined into one end of each bar for interfacing with the test specimen. An aluminum anvil, 25.4 mm in diameter and 6.4 mm thick, is mounted to the striker end of the incident bar. The incident bar end is threaded with ¼-20 UNC female threads. A 25.4 mm long socket head cap screw passes through the anvil and constrains it to the end of the incident bar. The 0.25 m long hollow striker that slides along the incident bar has a 25.4 mm outside diameter and 12.7 mm

inside diameter. This is capable of producing loading pulses of approximately 100 microseconds duration. This setup is shown schematically in Fig. 2.1.
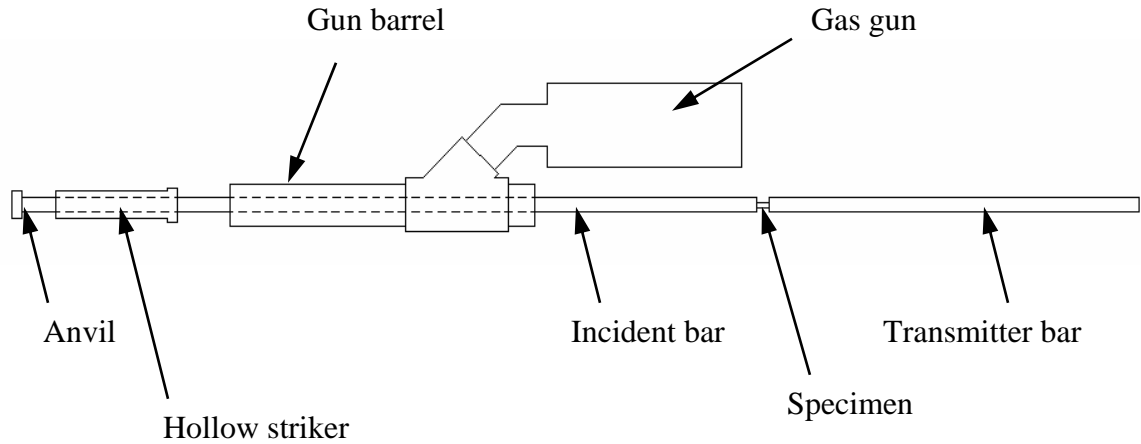
Figure 2.1: Finalized setup

2.2   Design of the launching apparatus

In order to use a hollow striker, a launching mechanism capable of accelerating the striker to a desired velocity must be in place. Due to the axial nature of the SHTB setup, the launching mechanism cannot obstruct the path of the incident bar. Accordingly, a gas gun was modified to meet the requirement. In a normal gas gun, a barrel is separated from a pressure chamber with a valve. When the valve is opened, the pressurized gas from the chamber is allowed to escape into the barrel. Since this apparatus requires the striker to be hollow and travel along a rod coaxially, the valve cannot be inline with the barrel, because the rod must pass through the setup. Hence, a normal gas gun was modified such that the chamber and valve are off axis from the

barrel. The air enters the barrel at a 45° angle. A schematic of the modified setup is
shown in Fig. 2.2.
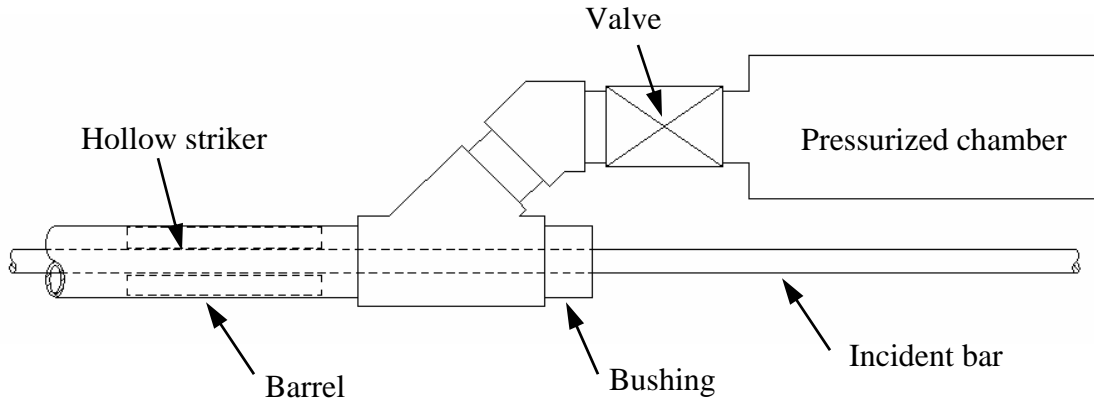
Figure 2.2: Schematic of launching apparatus

When the valve is opened, the gas can flow through the elbow and wye fittings
and into the barrel, thus propelling the striker forward. The aft end of the barrel has a
bronze bushing surrounding the location where the incident bar passes through to prevent
air from leaking out.

The gun barrel is constructed from seamless steel tubing with 50.8 mm outside
diameter and 38.1 mm inside diameter. Several 12.7 mm diameter exhaust holes are
drilled into the fore end of the barrel. Schedule 80 cast iron pipe fittings with diameter of
38.1 mm are used to assemble the barrel to the valve and also to connect the valve to the
aluminum bulkhead. The gas chamber is constructed from a 152 mm diameter cast iron
pipe. It is sealed to the aluminum bulkheads with a room temperature vulcanized rubber
sealant. Four, 25.4 mm diameter threaded rods are used to maintain a compressive load
on the chamber. A pressure gage and quick release fitting is attached through the aft

bulkhead to allow the chamber to be filled with gas. A photograph of the gas gun as constructed is shown in Fig. 2.3.
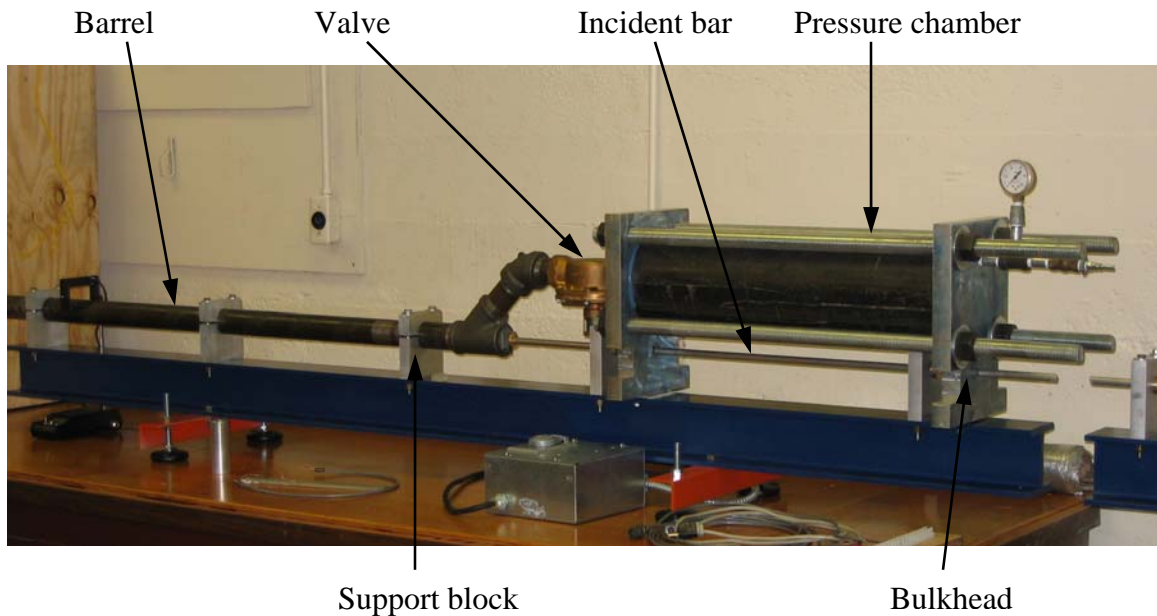
Figure 2.3: Assembled gas gun

Once assembled, the modified configuration was test fired several times to find the relationship between striker velocity and gas chamber static pressure. For all experiments, air was used as the working fluid. At chamber pressures below approximately 27.5 kPa (gage), it was difficult to obtain repeatable velocities. These tests also served to find the working limits of the gun. However, since most of the SHTB tests would be conducted with a striker velocity of less than 10 m/s, it was unnecessary to look at chamber pressures higher than about 172 kPa (gage). The results from the firing tests are shown in Fig. 2.4.
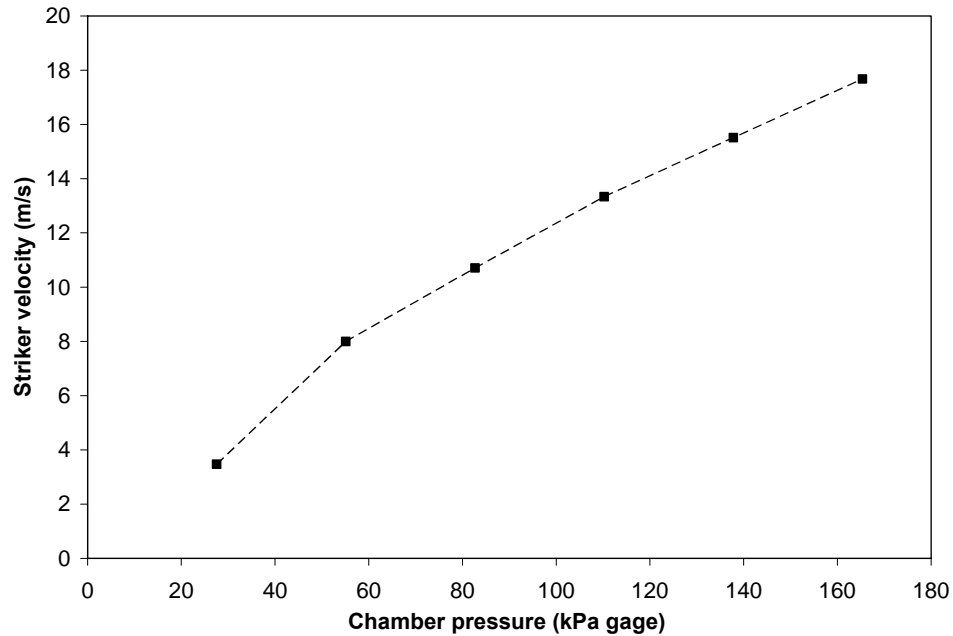
Figure 2.4: Striker velocity vs. chamber pressure for gas gun

2.3   Selection of materials

The major components of this setup were constructed from 7075-T6 aluminum. Polymers, which are of specific interest in the present work, often fail at relatively low stresses. Considering that these stresses are determined by making a measurement on the transmitter bar, the transmitter bar needs to undergo an amount of strain that is measurable with a high signal to noise ratio. Materials like steel, which is commonly used in SHTB testing, are not practical for these measurements. Steel is relatively stiff compared to the soft polymers being tested. Due to this, the transmitted stress will result in a very small strain value in the transmitter bar. Thus the signal will be very feeble. Aluminum is the choice material because it has a lower elastic modulus, but like steel, it has a linear elastic behavior prior to yielding. Aluminum alloy 7075-T6 was the specific

22

alloy chosen because its elastic limits are sufficient to endure repeated loading without failure.

The 12.7 mm bar diameter was selected for several reasons. The bar diameter cannot be too large, because as the diameter increases, it becomes more difficult to ensure that the elastic waves are propagating one-dimensionally. Also, as the bar cross-section increases with bar diameter, the compliance decreases, and less strain is produced for a given amount of force. Thus as the diameter increases, the magnitude of the transmitted signal will decrease for a fixed specimen size. On the other hand, the bar diameter cannot be too small or it will be difficult to successfully grip the specimen. Most SHTB setups utilize bars with diameters in the range of 12.7 mm to 25.4 mm.

2.4   Design of the anvil

Once the gun was constructed and proved to be in working condition, attention was given to the impact end of the incident bar. The main goal of the anvil design is to produce a square pulse that can eventually be altered in amplitude by adjusting the impact velocity and can be altered in shape by using pulse shaping techniques. An idealized loading pulse is shown in Fig. 2.5.
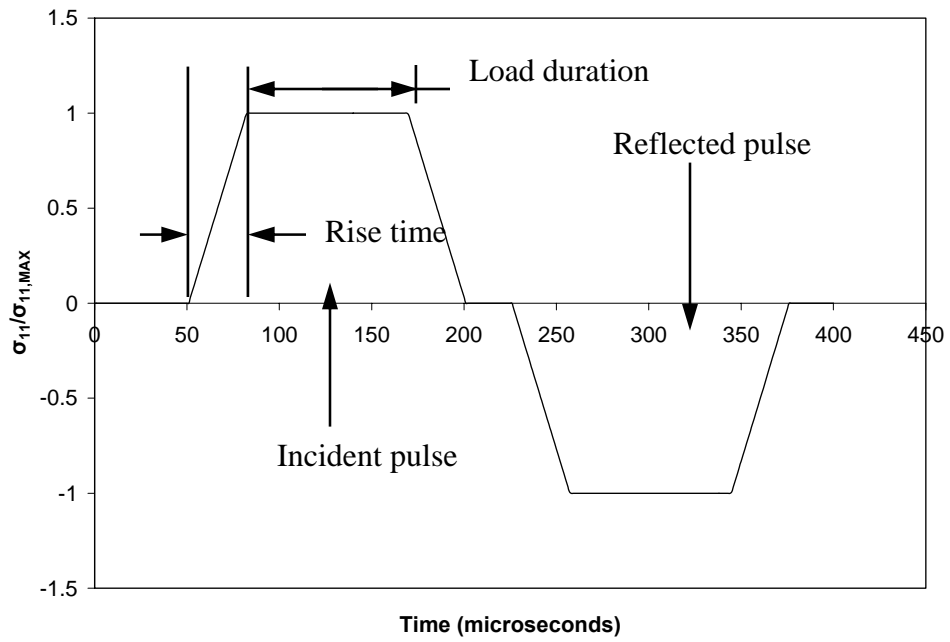
Figure 2.5: Idealized loading pulse
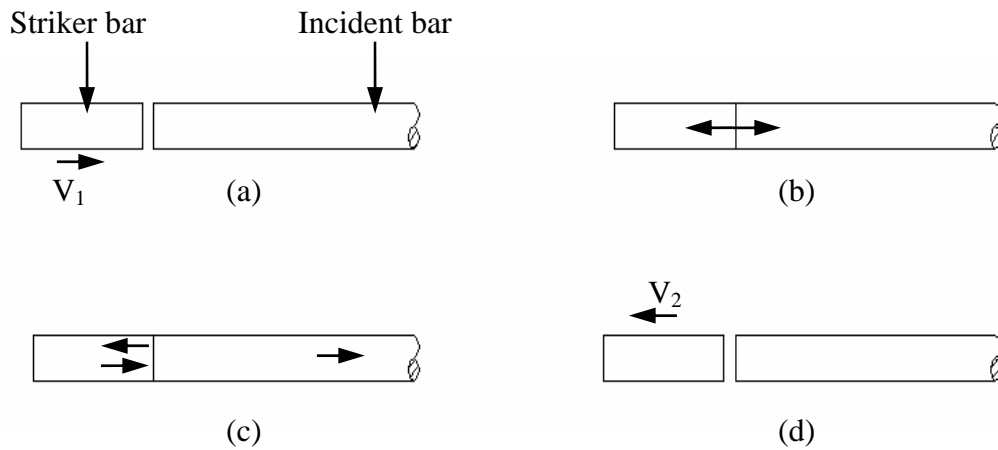
Figure 2.6: Impact condition at (a) just prior to impact, (b) at impact, t = 0, (c) during impact, $t = \dfrac{L}{C_0}$, (d) just after separation, $t = \dfrac{2L}{C_0}$

The time duration of the loading pulse is related to the length of the striker bar. From Fig. 2.6, at impact, (b), a compressive wave initiates at the impact surface of the striker bar. At (c), that wave reflects off of the free end of the striker as a tensile wave. At (d), the tensile wave produces a separation at the original impact surface. Therefore, the wave must propagate one complete round trip in the striker before separation can occur. The load duration is consequently $t = \dfrac{2L}{C_0}$ or the length of time the striker is in contact with the bar.

Five major iterations were completed to arrive at the impact mechanism that would be permanently implemented in the apparatus.

- Large diameter striker tube and anvil

- Large diameter striker tube and anvil with a secondary anvil

- Small diameter striker and anvil

- Small diameter striker and anvil with a secondary anvil

- Small diameter striker and anvil with a rubber damper

2.4.1 Design iteration #1 – large diameter striker and anvil

The first major design consisted of a hollow striker with an outside diameter of 38.1 mm (same as the inside diameter of the barrel) and an inside diameter of 12.7 mm (same as the outside diameter of the incident bar). The length of the striker was chosen to be 0.25 m. This was determined to be of adequate length to produce a long enough loading pulse based on the elastic characteristics of the striker. Since the striker is made

from aluminum, which has an elastic wave speed of approximately 5,100 m/s, it takes approximately 100 microseconds to travel the 0.5 m round trip in the striker. This length was held constant through all of the experiments. For this first configuration, the striker impacted an anvil that was attached to the end of the incident bar with normal threads as shown in Fig. 2.7. The anvil was 25.4 mm in length and the cross-sectional area was the same as that of the striker.

Anvil   Incident bar   Striker   End of gun barrel

Threaded end
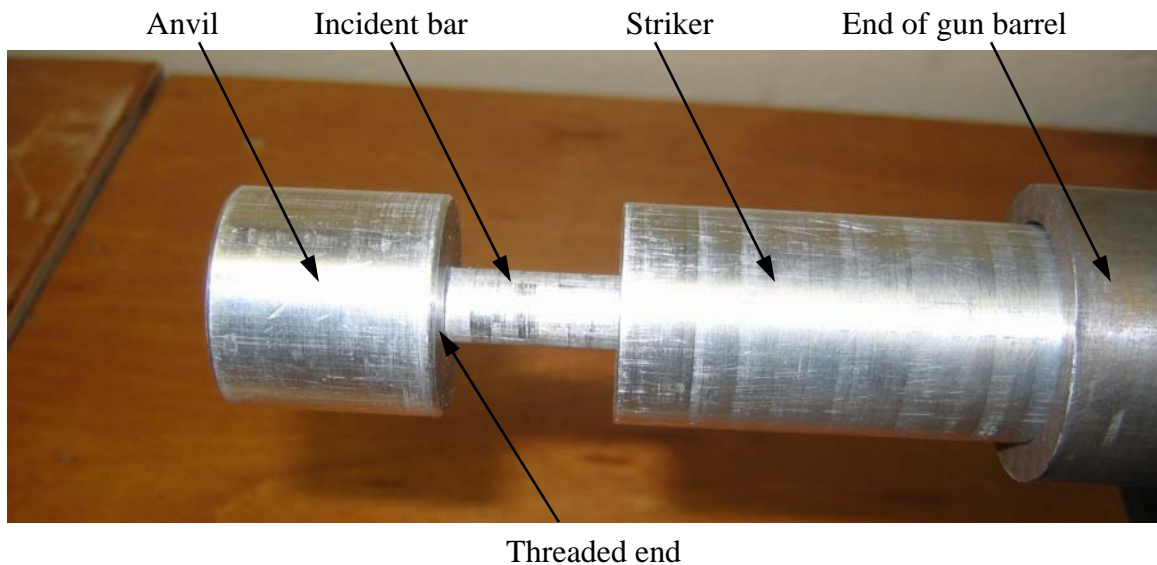
Figure 2.7: Design iteration #1

This configuration was tested by mounting a strain gage approximately 0.75 m from the specimen end of the incident bar. Once assembled, the striker could be fired and the strain history in the incident bar could be recorded to see the shape of the resultant pulse. This setup produced a very poor loading pulse. The rise time of the pulse was sufficiently short; however, the pulse was not square. The subsequent oscillatory

behavior made it difficult to differentiate between the incident wave (pure tension) and the reflected wave (pure compression). These pulses are shown in Fig. 2.8.
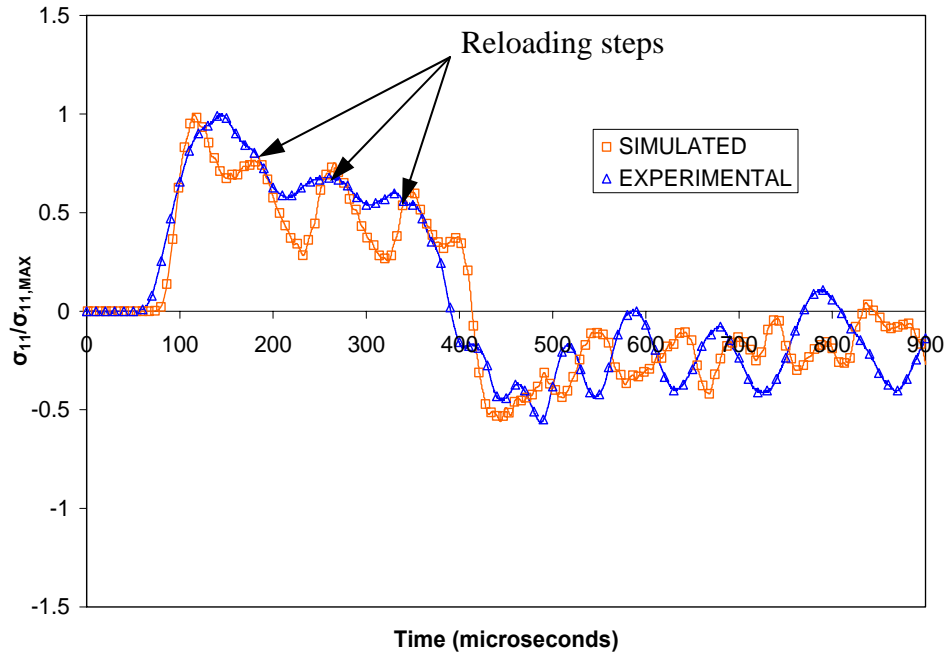
Figure 2.8: Experimental and simulated comparison of iteration #1

This setup was also simulated with a finite element model using ABAQUS®. The model was constructed using a two piece assembly. A 2-dimensional model was created with half symmetry. This allowed the use of axisymmetric, plane strain elements which greatly reduced the necessary computational effort. The elements chosen were CAX4R which are axisymmetric, bilinear elements with reduced integration and hourglass control. The average element size for the model was approximately 1 mm^2.

The model was split up into two analysis steps. In the first step, the striker was given a velocity boundary condition. The step duration was about 1 microsecond, which

27

was short enough not to allow the striker to impact during the step. In the second step, this velocity boundary condition was removed so that the impact took place while the striker was under no imposed boundary conditions. By doing this, the stress fields in the model are only produced by material inertia.

Contact was established along the interface between the striker and the anvil as shown in Fig. 2.9. The surface to surface contact formulation was used. For this, the two desired element-based surfaces were paired up in a master-slave relationship. Generally, there are limitations on which surface is to be used as the master surface and which is to be used as a slave surface. However, these guidelines were unnecessary due to the similarity in compliance between the two surfaces.

Due to the complexity associated with the contact elements, the simulation was run in ABAQUS® explicit with automatic time incrementation. The explicit solver in ABAQUS® is much more numerically efficient, and thus cost effective, for the analysis of discontinuous events such as those associated with contacting bodies. The automatic time estimators built into ABAQUS® proved to be very stable for this model. The time increment size stabilized at approximately 130 nanoseconds.

From Fig. 2.8, it can be seen that the simulation follows the general trend of the experiment very well. The oscillations in the simulated data are much higher than the oscillations in the experimental data. This occurs, to some extent, in the simulations done for all of the iterations, and is attributed to the finite element analysis not accounting for possible damping that occurs in the experiment. The oscillations occur at the same frequency in both cases, but are of different amplitudes and at small phase differences relative to each other.
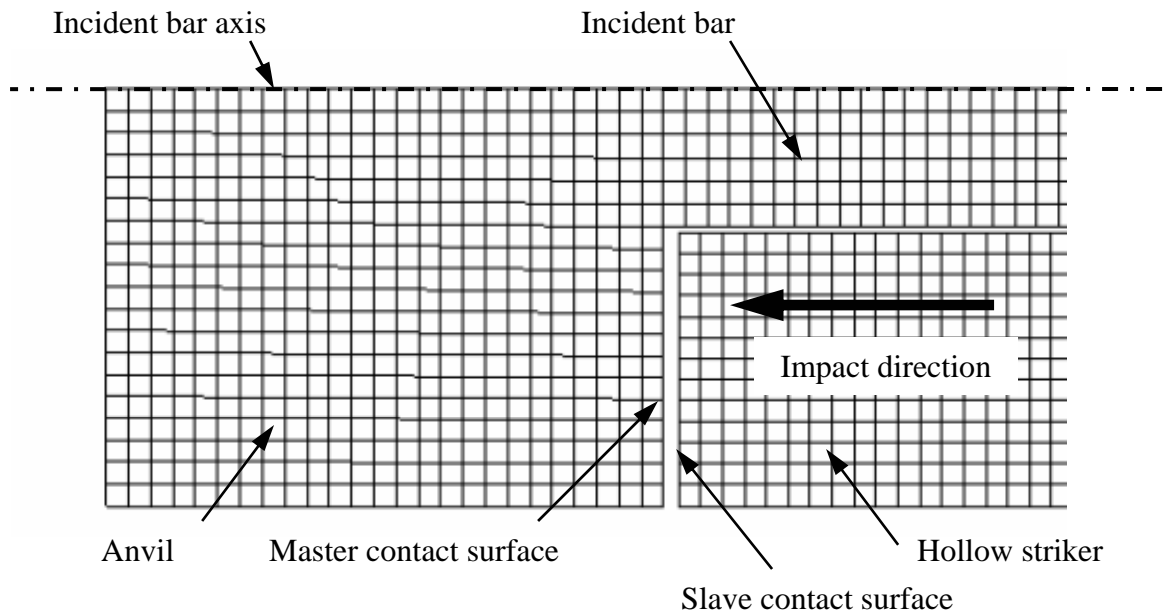
Figure 2.9: FE model used for analyzing design iteration #1

Several minor modifications were made to this layout in an effort to better understand the problems at hand. They include (a) using a jamb nut to pretension the threads on the anvil, (b) trying different striker bar lengths, (c) machining different anvil shapes including tapered anvils and anvils with reduced overall length, (d) greasing the impact surfaces, and (e) drilling extra exhaust holes into the barrel to ensure that the striker was not under acceleration at the impact point. Also, instead of using a single strain gage, two strain gages were placed at diametrically opposite locations on the incident bar to ensure that there were no flexural waves that were affecting the signal. None of these attempts proved to cause an appreciable change in the experimental results.

Despite being unsuccessful, the first major design iteration gave a chance to debug issues associated with the launching apparatus as well as the data acquisition

system. It also helped in realizing the complexity of the problem. The complementary finite element model that was developed served as a tool for providing better insight into future iterations of the design.

2.4.2   Design iteration #2 – addition of a secondary anvil to iteration #1

The second configuration involved using the same anvil and striker as the first, but another tube was registered against the anvil on the surface opposite the impact surface as shown in Fig. 2.10.
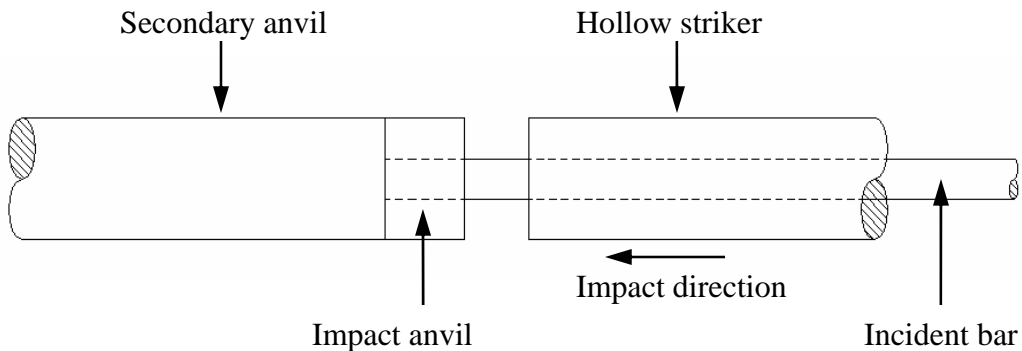
Figure 2.10: Schematic of iteration #2

The secondary anvil serves to mitigate extra energy from the striker. In an ideal case, at impact, a tensile wave is generated in the incident bar and a compressive wave is generated in the striker tube. The wave propagates the length of the striker and reflects off the free end of the striker as a tensile wave. When it returns to the impact surface, the tensile wave causes the striker to separate from the anvil. Thus, as stated earlier, the time

30

duration of the loading pulse is the same as the amount of time it takes an elastic wave to propagate twice the length of the striker tube. Since the cross-sectional area of the striker is so much greater than that of the incident bar, the striker is much less compliant than the bar and anvil. The tensile reflection in the striker is insufficient to cause separation at the impact surface.   Thus, the initial step of the loading pulse is the appropriate time duration; however, the extra energy causes additional "loading steps" of lower amplitude as seen in Fig. 2.8. In preliminary experiments, it was noted that the secondary anvil helped to reduce the amplitude of these steps.

Again, an FE model was constructed to simulate this condition. Once the model was constructed, different scenarios could be examined to see the effect of parameters such as striker tube length, anvil length, and striker tube cross-sectional dimensions. The model was created in the same manner as the model for iteration #1. Axisymmetric, plane strain elements were used on a half-symmetric, 2-dimensional model.   The assembly consisted of three different parts: the striker tube, the incident bar and anvil, and the secondary anvil.
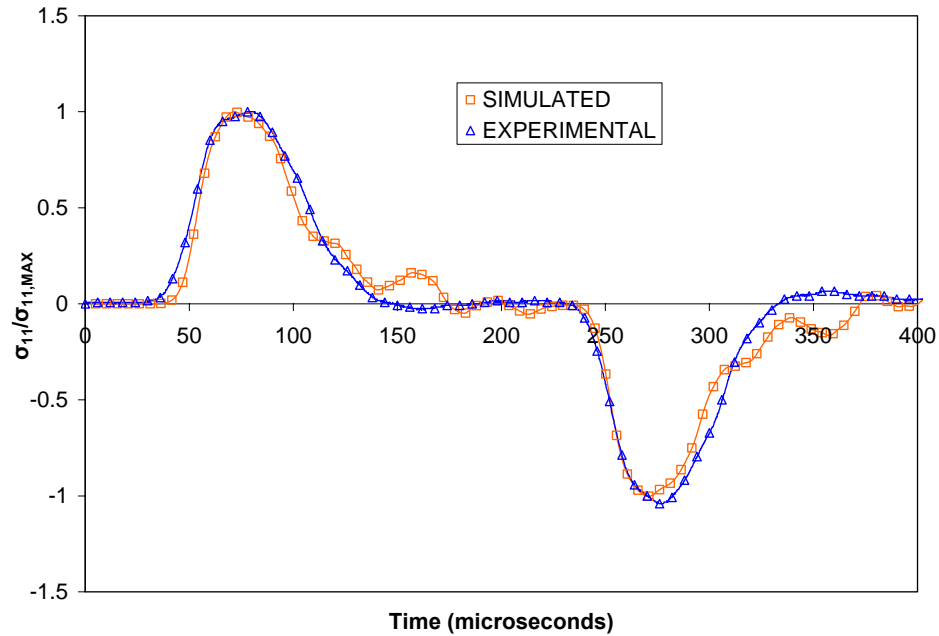
Figure 2.11: Experimental and simulated comparison of iteration #2

As evidenced in the Fig. 2.11, two distinct (incident and reflected) signals are identifiable. This is an important point because the strain rate, and thus the strain, is derived from the reflected pulse. In the previous iteration, the pulses were superimposed on one another. This does not allow for calculations based on the reflected signal. The separation of the signals was a notable accomplishment of design iteration #2.

2.4.3   Design iteration #3 – smaller diameter striker and anvil

Once the effect of the secondary anvil was more fully understood, the effect of the cross-sectional area of the striker could be explored. The third iteration of the design involved using the same configuration as the first design iteration, only with a striker tube

and impact anvil of smaller outside diameters. In this configuration, the anvil has a
through hole in it and is bolted to the incident bar end which has female threads.
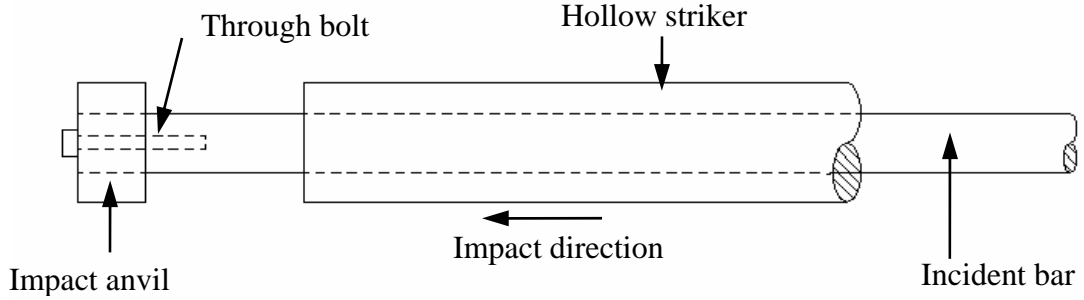
Figure 2.12: Schematic of iteration #3
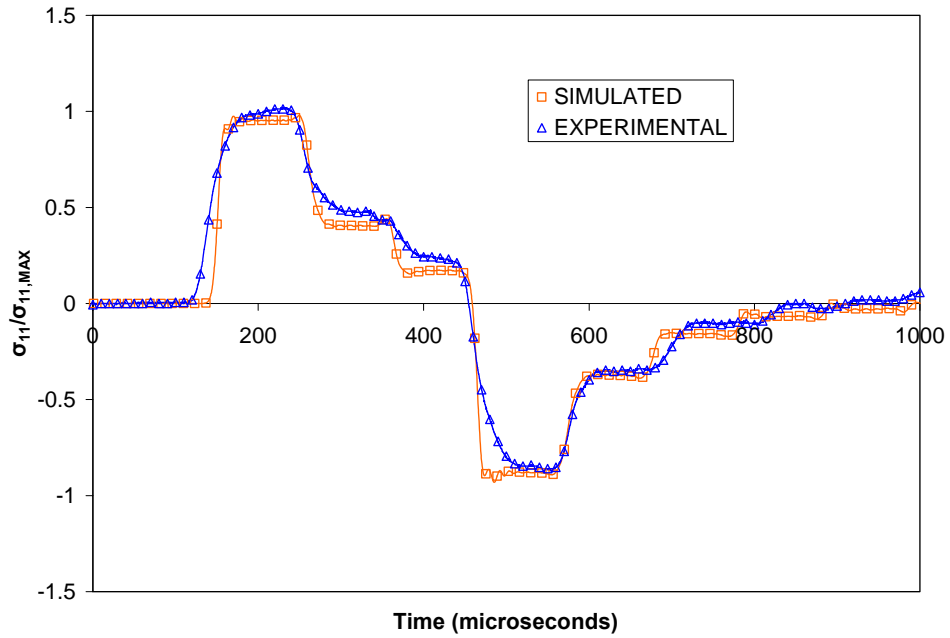
Figure 2.13: Experimental and simulated comparison of iteration #3

This configuration improved the shape of the pulses tremendously as seen in Fig. 2.13. The waveform clearly has a sharper profile. Also, with this setup, the incident and reflected pulses can be identified individually. From this set of experiments, it was evident that some combination of the second and third design iterations would probably be capable of producing the correct pulse shape. Also, through the first three design iterations, excellent agreement was observed in the data trends between the experimental and simulated sets. The main difference is that the simulated results from the impact tend to have sharper edges compared to the experimental ones. As mentioned earlier, this can be attributed to the simulation not accounting for damping that exists in the experiments. Also, the simulation does not account for dispersion of the stress waves over the propagation length. In the simulation, the highest frequency waves are allowed to propagate at the same wave speed as the lower frequency waves. In reality, higher frequency waves travel at a much lower wave speed. This is the essential reason for the simulated pulses to be so sharp, and the experimental pulse to be slightly rounded off and spread out. The details of this phenomenon are covered in another section of this thesis.

2.4.4   Design iteration #4 – addition of a secondary anvil to iteration #3

It was concluded that design iteration #4 should comprise some combination of the previous three configurations. A small diameter striker with a secondary anvil or other damping mechanism would probably be ideal. An aluminum secondary anvil was chosen for the first trial of this iteration. The secondary anvil was constructed to be the same length as the striker tube.
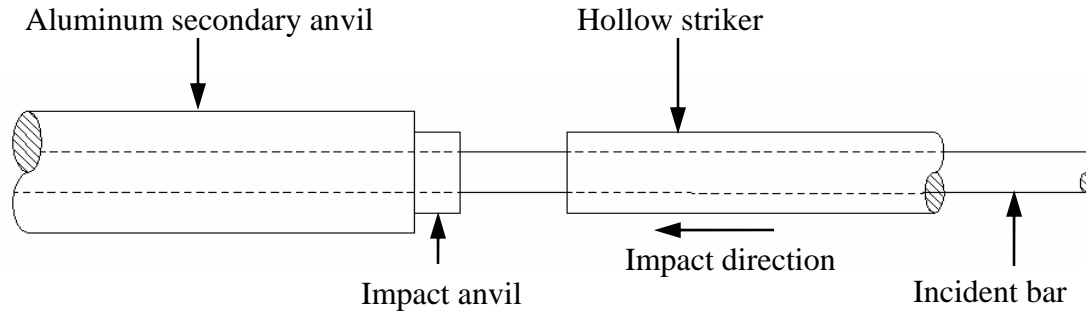
Figure 2.14: Schematic of iteration #4
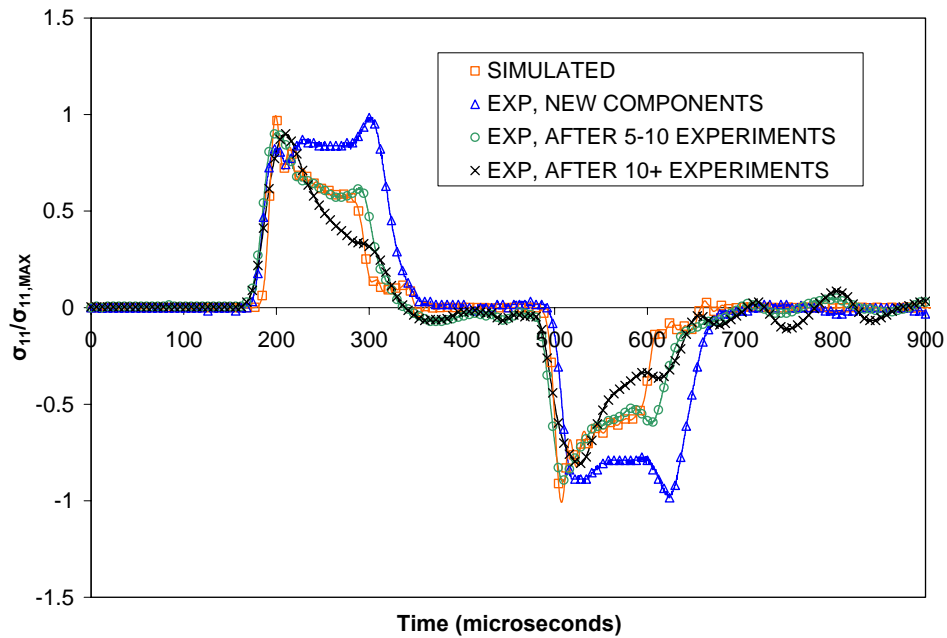
Figure 2.15: Experimental and simulated comparison of iteration #4

It was more difficult to achieve such good agreement between the simulations and the experiments for this particular arrangement. Several experiments were carried out and the results are shown in Fig. 2.15. The first set of data provides a very good square loading pulse; however, it was noted that after several experiments, the signals degraded

35

significantly as seen in the second and third data sets. Several factors contributed to this degradation. The surface of the secondary anvil had a tendency to get damaged because there was no practical way to constrain it. After the main impact, the impact anvil would separate from the surface of the secondary anvil and strike it again. In the ensuing impacts, the striker would not hit the anvil squarely, thus causing disfigurement of both surfaces. Also, if the impact anvil was not registered squarely against the secondary anvil, the signal would be unsatisfactory. A considerable amount of testing was done using this configuration; however, it proved to be too difficult to get consistent loading pulses.

2.4.5   Design iteration #5 – addition of a rubber pad

In the final design iteration, a rubber pad was used as the energy absorbing mechanism instead of the secondary anvil. After a number of experiments, it was determined that a square pulse with a rise time of ~40 microseconds could be generated consistently. This configuration could be used repetitively without causing damage to the components. After performing an experiment in the absence of the specimen, it was noted that the incident and reflected signals are almost identical, meaning that most of the energy is reflected. Signals collected from this configuration are shown in Fig. 2.16. This loading mechanism repetitively exhibited satisfactory performance.
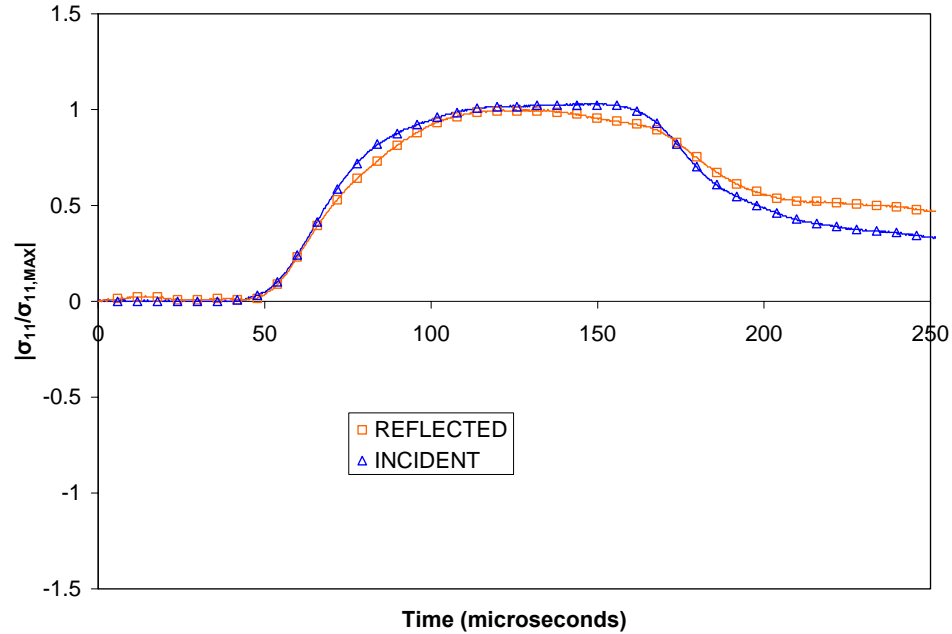
Figure 2.16: Comparison of incident and reflected signals for iteration #5

2.5   Design of the specimen-bar interface

In terms of the gripping mechanism, a dovetail shape was chosen in an effort to reduce the attenuation that can occur in more complex attachment configurations such as specimens with threaded ends, clamps with fasteners, etc. The tensile specimens were made in the shape of a dogbone. Dogbone geometries have known value in the area of quasi-static tensile testing. FE analysis was used to study different geometries and arrive at a specific shape that would allow the bars to be used repeatedly without damage. The details of this process are outlined in the current section.

A generic dovetail shape is shown in Fig. 2.17 along with the complementary dogbone specimen. There are several features that require attention in this particular

37

arrangement. Some of these include (a) the dovetail width, (b) the dovetail length, (c) the angle between the dovetail and the axis of the bar, and (d) the filet radius.
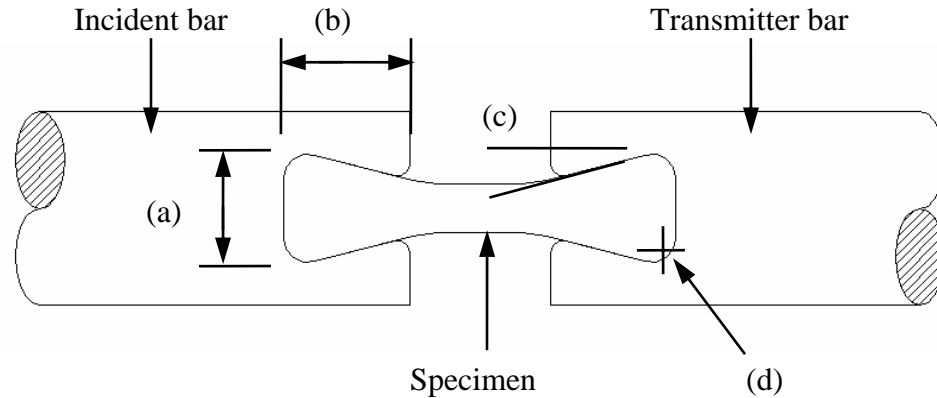
Figure 2.17: Generalized dovetail configuration showing features of interest

The selected initial geometry was machined and tested in the actual setup. For this initial specimen-bar interface geometry the dovetail in the incident bar end failed. A closer look at this geometry with FE analysis revealed that the stresses produced in the aluminum grips during the experiment due to the stress concentration were in excess of the failure stress for the 7075-T6 aluminum being used. Thus, this geometry was used as a benchmark for refining the specimen-bar interface shape such that the tensile testing would not result in failure of the grip region of the incident bar.

The finite element model used for this purpose consisted of two parts, the specimen and the incident bar ends. The geometry was modeled in Solid Edge® graphics tool and converted into an IGES (initial graphics exchange specification) format. This is a neutral file format that could be imported directly into ABAQUS® structural analysis environment. The two parts were then discretized independently and merged together as an assembly. Due to the complex geometry of the bar end, 4-noded linear tetrahedral

elements (C3D4 in ABAQUS®) were used for the mesh. The specimen itself was meshed using 8-noded linear brick elements (C3D8R in ABAQUS®). Quarter symmetry of the configuration was exploited to reduce the size of the model. This allowed the use of a much denser mesh for improving the accuracy of results. About 20,000 elements were used to discretize the incident bar end, and about 1,000 elements were used for the specimen. Figure 2.18 shows the loads and boundary conditions used in the model. The mesh is shown in Fig. 2.19.
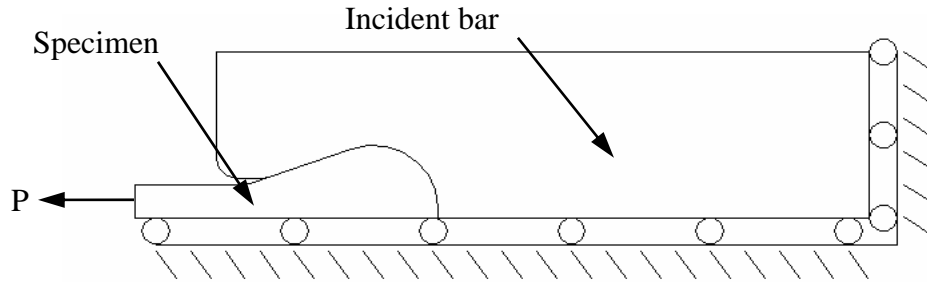
Figure 2.18: Loads and boundary conditions for dovetail model
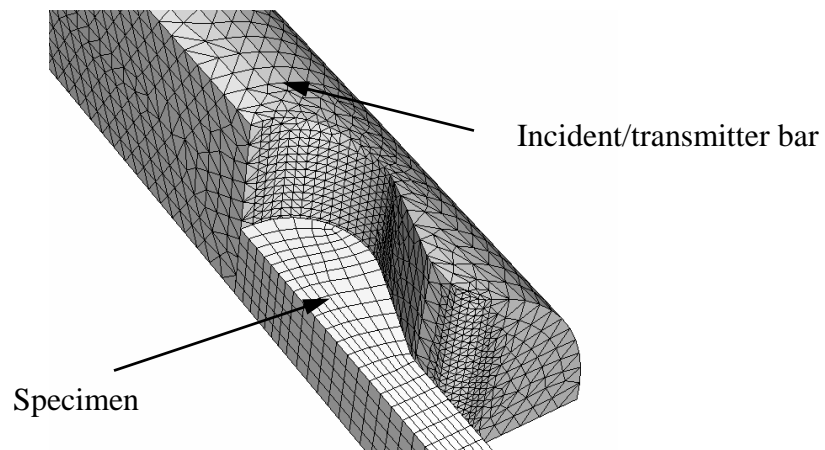
Figure 2.19: FE model of dovetail grip
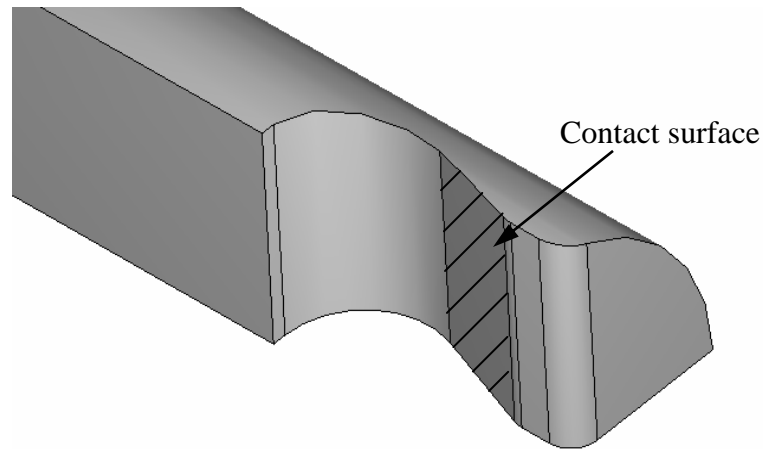
Figure 2.20: Surface of contact enforcement

Contact elements were used along the interface between the bar and specimen on the hatched surface shown in Fig. 2.20. The contact was formulated for both the surface normal and tangential directions. The constitutive law for contact elements included a linear stress-strain behavior in the direction normal to the surface with a stiffness of approximately 10 times the stiffness of the aluminum grip. The aluminum surface was chosen as the master surface. In the direction tangential to the surface, the friction between the aluminum grip (master surface) and specimen end (slave surface) was also accounted for using a rather basic stiffness (penalty) method. In this method, a certain amount of shear stress is carried across the interface between the master and slave surfaces. The shear stress is directly proportional to the normal load between the surfaces. This allowed for the estimation of the friction during the loading event. These parameters for the contact condition were chosen based on guidelines provided in the ABAQUS® user's manual [29]. The end of the bar was constrained from translation in

40

the horizontal direction, and a uniform pressure was applied on the end surface of the specimen (Fig. 2.18).

The stresses through the thickness at the location of the least cross-sectional area of the grip (Fig. 2.21) were the primary output quantity of interest. Designing for a minimal stress ensures that the bar end will endure repetitive loading of the grips. Twelve iterations of the design were explored with the FE model. The particular parameters being studied included the angle of the dovetail, the maximum width of the dovetail, and the length the dovetail extends into the incident bar. The initial (a) and final (d) geometries that were analyzed are shown in Fig. 2.22. Also shown are two of the intermediate geometries (b and c).

Stress monitored through thickness along this line

Grip end of the incident/transmitter bar
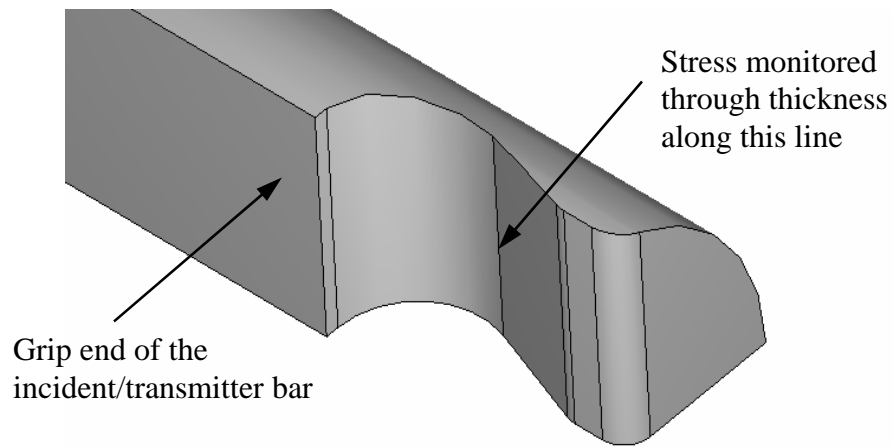
Figure 2.21: Line of interest for stresses
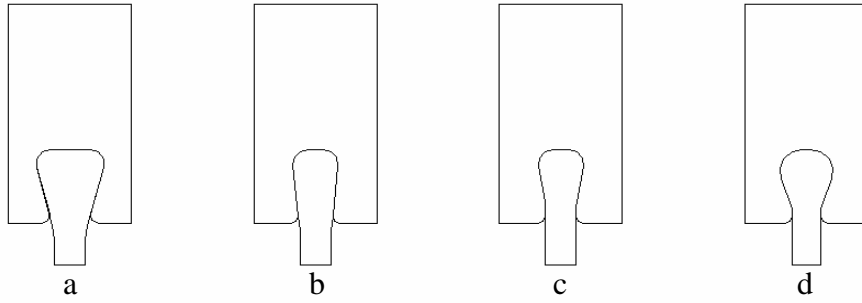
Figure 2.22: Geometries of interest
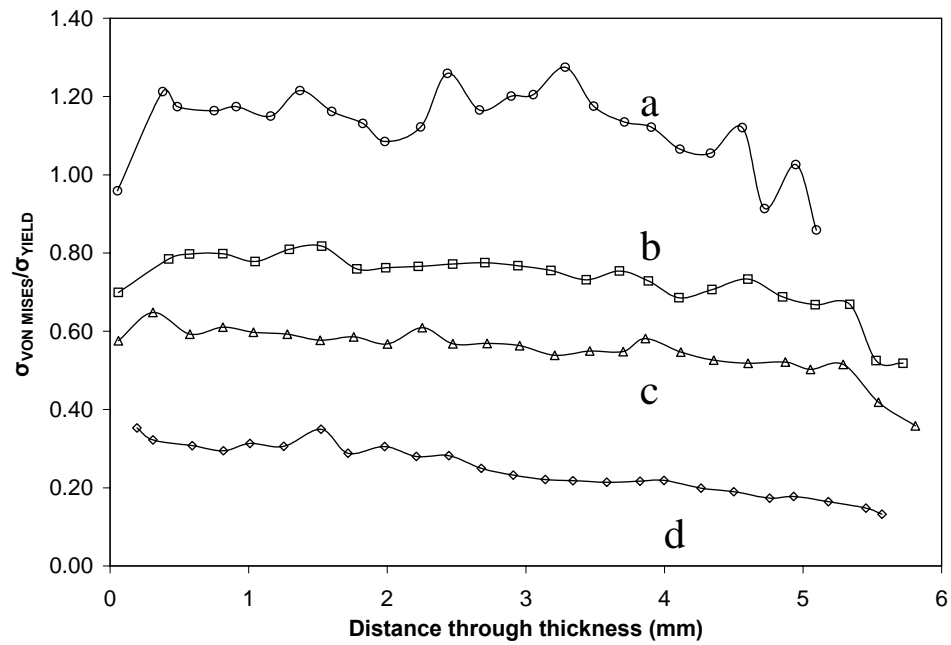
Figure 2.23: Stress through the thickness for different geometries

The plots in Fig. 2.23 correspond to the stresses along the line shown in Fig. 2.21. The origin of the plot corresponds to the mid-plane of the cylindrical rod. As can be seen, iteration (a) exceeded the yield strength of the aluminum by 20% and iteration (d) of the dovetail design had significantly lower stresses.

42

2.6   Specimen stress distribution

For tensile specimens, it is necessary that the gage section has a uniform stress distribution, and that there are no obvious stress concentrations. A plane stress finite element analysis was completed to verify this. The FE model consisted of the desired dogbone geometry registered against an analytically rigid surface. Since the aluminum is essentially rigid in comparison to the polymer specimen, an analytically rigid surface could be used instead of a meshed deformable body, thus simplifying the model. Also, quarter symmetry was invoked. The mesh consisted of 8-noded biquadrilateral plane stress elements (CPS8R in ABAQUS®). The stress distribution contoured for von Mises stresses is shown in Fig. 2.24. The constructed grip is shown in Fig. 2.25.
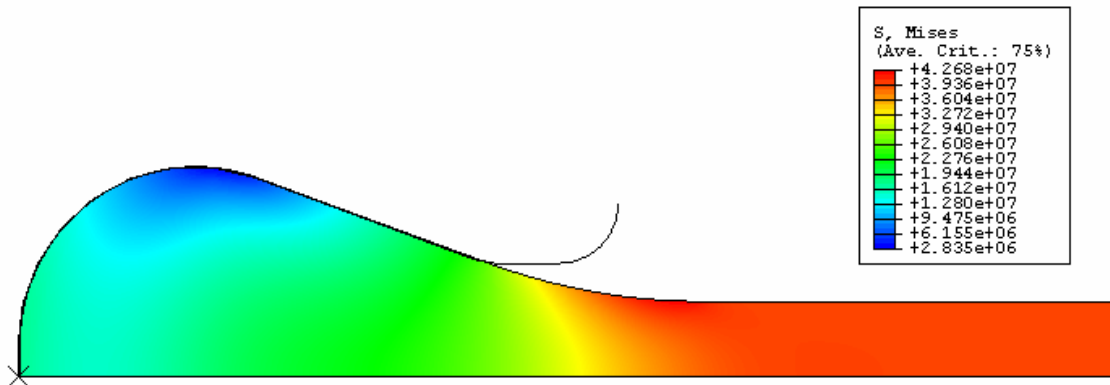
Figure 2.24: Specimen stress distribution for a 40 MPa uniaxial load

Incident grip   Specimen   Transmitter grip
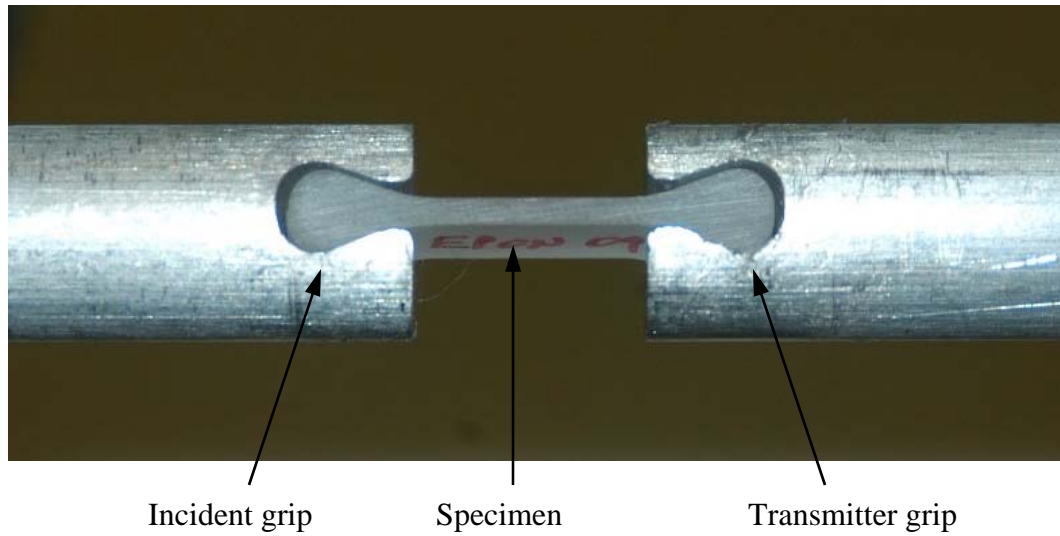
Figure 2.25: Specimen-bar interface as constructed

2.7   Other apparatus design considerations

There were several other minor details that required attention during the SHTB design. The first of these was height adjustability. The system was designed using two independent I-beams as the supports for the two bars. Since they are independent of each other, adjustable feet were mounted to each beam. A self-leveling laser level was used to ensure that the top surfaces of the beams were aligned in the vertical plane. Support blocks were mounted on the top surface of each beam to constrain the two bars. Each bar support was fitted with a bronze bushing machined to the proper tolerance. This allowed the bar to slide freely in the axial direction.
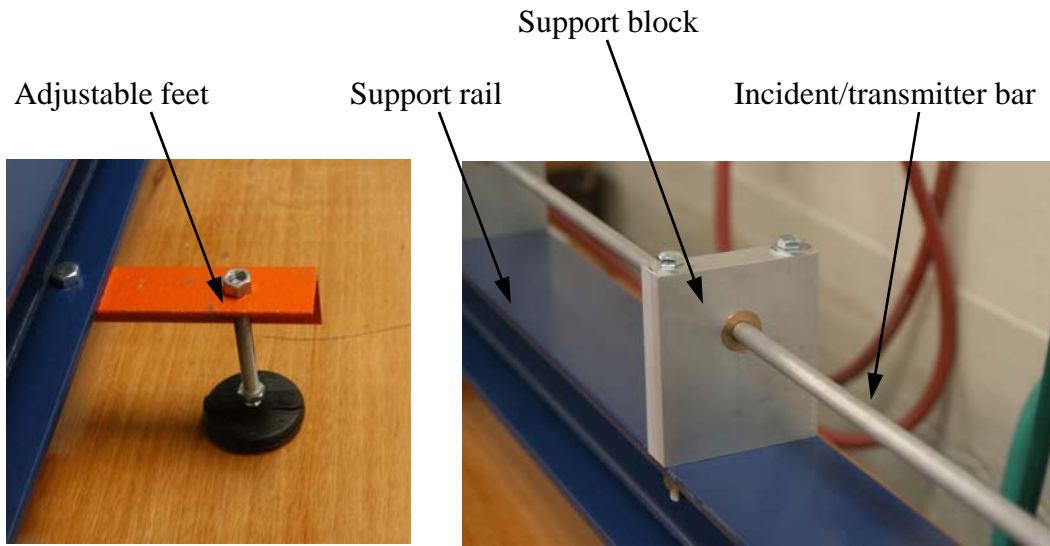
Figure 2.26: Adjustable feet and support blocks

CHAPTER 3

DATA COLLECTION AND REDUCTION

3.1   Introduction

Once the working apparatus was in place, potential data collection and analysis methods were considered prior to conducting experiments. First, the data of interest was identified, and a system implemented for collecting and analyzing that data. This chapter begins by deriving the governing equations for the split Hopkinson bar setup. Next, the characteristics for this configuration are examined using the Lagrangian X-t diagram. A strain gage type and size is selected, and the details of a data acquisition system are described.   Lastly, elaborations are made on the data post processing procedure.

3.2   Derivation of governing equations

3.2.1   Equations for specimen strain rate and strain

In classical split Hopkinson bar analysis, the specimen stress, strain, and strain rate are all determined using the signals measured on the incident and transmitter bars. The following section describes the details of the derivation of the equations used to perform these calculations. This derivation is carried out by finding out how particle

velocity is related to strain, and then using that relationship to determine the relative velocity between each of the bar ends. To begin, the equation of motion for a wave traveling along a bar is given by the one-dimensional wave equation:

$$C_0^2 \frac{\partial^2 u_1}{\partial y^2} = \frac{\partial^2 u_1}{\partial t^2},$$
(3.1)

where C_0 is the bar wave speed, y represents the spatial variable, $\frac{\partial^2 u_1}{\partial t^2}$ is the second time derivative of displacement (particle acceleration), and is the same as $\frac{\partial V}{\partial t}$, with V being the particle velocity. Using these relationships, along with Hooke's law, strain-displacement relations, and the equation of motion, the pressure and velocity can be related across the bar cross section.

First, from Hooke's law, stress and strain are related by $E\varepsilon = \sigma$ where E denotes elastic modulus, ε is the strain, and σ is the stress. This can be rewritten as,

$$E\left(\frac{\partial u_1}{\partial y}\right) = \sigma .$$
(3.2)

Taking the derivative of both sides gives

$$E\frac{\partial}{\partial y}\left(\frac{\partial u_1}{\partial y}\right) = \frac{\partial \sigma}{\partial y}.$$
(3.3)

Knowing that the bar wave speed is related to the mass density and elastic modulus as $C_0 = \sqrt{\frac{E}{\rho}}$ or $E = \rho C_0^2$, the former expression can be rewritten as,

$$\rho C_0^2\left(\frac{\partial^2 u_1}{\partial y^2}\right) = \frac{\partial \sigma}{\partial y}.$$
(3.4)

Finally, substituting in the relationship given by the equation of motion gives the following:

$$\frac{\partial \sigma(y,t)}{\partial y} = \rho \frac{\partial V}{\partial t}. \tag{3.5}$$

The particle velocity, V, is found by solving Eq. 3.5. To do this, the stress distribution must be known in the bar. If the stress wave that is propagating in the bar is harmonic, the distribution will have the form of $\sigma(y,t) = Pe^{i(\omega t - ky)}$. Here, P is the amplitude, ω is the circular frequency, y and t are the spatial and temporal variables, and k is the wave number defined by $k = \frac{\omega}{C_0}$. Taking the spatial derivative of the stress wave distribution gives thus yields

$$\frac{\partial \sigma(y,t)}{\partial y} = -ikPe^{i(\omega t - ky)}. \tag{3.6}$$

Equation 3.6 can be substituted into the pressure-velocity relationship (Eq. 3.5) to get

$$-ikPe^{i(\omega t - ky)} = \rho \frac{\partial V}{\partial t}. \tag{3.7}$$

Rewriting Eq. 3.7 gives an expression for the temporal derivative of velocity,

$$\frac{\partial V}{\partial t} = -i\frac{k}{\rho}Pe^{i(\omega t - ky)}. \tag{3.8}$$

By integrating this expression with respect to time, the expression for particle velocity can be obtained as,

$$V(y,t) = -\frac{k}{\rho\omega}Pe^{i(\omega t - ky)}. \tag{3.9}$$

48

The assumed expression for stress distribution can be interchanged, and the relationship

between wave speed, frequency, and wave number, $\dfrac{1}{C_0} = \dfrac{k}{\omega}$ can be used to simplify the

expression in Eq. 3.9, to get $V(y,t) = \dfrac{1}{\rho C_0}\sigma(y,t)$. If the cross sectional area of the bar

is sized appropriately, the axial stress in the cross section is uniform, and is related to the

strain by $\sigma(y,t) = \varepsilon(y,t)E$. Thus strain is related to particle velocity as,

$$V(y,t) = C_0\varepsilon(y,t). \tag{3.10}$$

Strain rate is defined as the average strain divided by the time over which that

amount of strain occurs. Since strain is related to displacement, strain rate is related to

displacement divided by time, or velocity. If the first bar end displaces by a distance u_1,

and the second bar end displaces by u_2, the strain in the specimen located between the

two bars is $\varepsilon = \dfrac{u_1 - u_2}{L}$ where L is the gage length of the specimen. So, the strain rate is

simply the time derivative of this quantity or, $\dfrac{\partial \varepsilon}{\partial t} = \dfrac{V_1 - V_2}{L}$ where V_1 and V_2 denote

particle velocities at the two ends. Now, using the relationship between the particle

velocity and the strain, the strain rate can be computed. On the first bar, there are two

stress waves that are superposed on one another, one being the incident wave which has a

positive sign (tensile) and the other being the reflected wave which has a negative sign

(compressive). So the expression for velocity, V_1 is

$$V_1(y,t) = C_0\varepsilon_I(y,t) - C_0\varepsilon_R(y,t), \tag{3.11}$$

where subscripts *I* and *R* are used to denote the incident and reflected quantities. In the second bar, there is only one wave, the transmitted wave, which has a positive sign. Thus the expression for velocity, V_2 is

$$V_2(y,t) = C_0 \varepsilon_T(y,t),$$ (3.12)

with subscript *T* denoting the transmitted quantity. Using these expressions, the strain rate can be expressed in terms of the incident, reflected, and transmitted strains as,

$$\frac{\partial \varepsilon}{\partial t} = -\frac{C_0(\varepsilon_T - \varepsilon_I + \varepsilon_R)}{L}.$$ (3.13)

Since $\varepsilon_T = \varepsilon_I + \varepsilon_R$, the expression for specimen strain rate can be finally rewritten as,

$$\frac{\partial \varepsilon}{\partial t} = -\frac{2C_0 \varepsilon_R(t)}{L}.$$ (3.14)

It follows that the specimen strain can be found by simply integrating the above expression,

$$\varepsilon(t) = -\frac{2C_0}{L} \int \varepsilon_R(t)dt.$$ (3.15)

3.2.2   Equation for specimen stress

An appropriate expression for the specimen stress is derived next. A schematic of a tensile dogbone specimen is shown in Fig. 3.1. The time history of the average force in the specimen is given by $F(t) = \dfrac{F_1(t) + F_2(t)}{2}$ where F_1 and F_2 denote forces at the two ends of the specimen as shown.

Typical specimen   Gage section
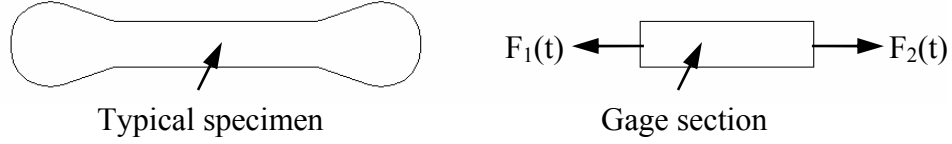
Figure 3.1: Specimen schematic and free body diagram

Thus the average stress in the specimen is $\sigma(t) = \dfrac{F(t)}{A_s}$ where the cross-sectional

area of the specimen is A_S. Given that the specimen is located between the two bars, the

two force terms can be written as,

$$F_1(t) = E\left[\varepsilon_I(t) + \varepsilon_R(t)\right]A_B,$$
(3.16)

$$F_2(t) = E\left[\varepsilon_T(t)\right]A_B,$$
(3.17)

where the cross-sectional area of the incident or transmitter bar is A_B. The average stress

is thus given by

$$\sigma(t) = \frac{EA_B}{2A_S}\left[\varepsilon_I(t) + \varepsilon_R(t) + \varepsilon_T(t)\right].$$
(3.18)

Since $\varepsilon_T(t) = \varepsilon_I(t) + \varepsilon_R(t)$, the average specimen stress can be rewritten finally as,

$$\sigma(t) = \frac{EA_B}{A_S}\varepsilon_T(t).$$
(3.19)

3.3   Strain gage location, type, and size

3.3.1   Selection of gage location

From the derivations shown in the previous section, it is evident that one strain gage is required for measuring the incident and reflected signals and another is required for measuring the transmitted signal. The Lagrangian X-t diagram can be used to identify the proper locations for these gages. This diagram, Fig. 3.2, shows the positions and times for each of the elastic waves that are propagating in the setup.
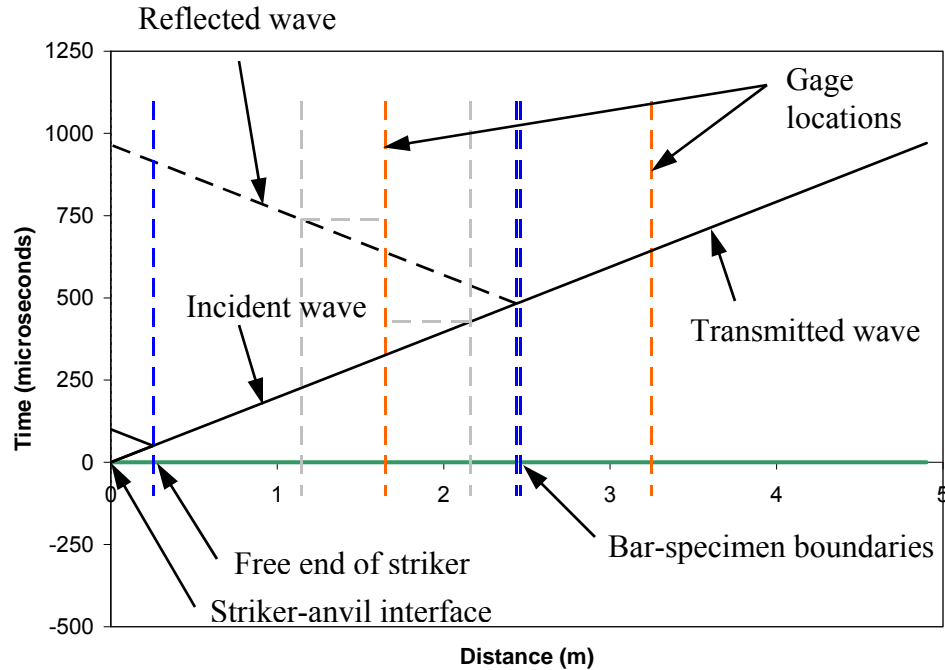
Figure 3.2: Lagrangian X-t diagram

The origin of this plot represents the impact end of the incident bar. The dashed blue vertical lines identify boundaries between the specimen and each bar end. The first is the free end of the striker bar, the second marks the specimen-incident bar interface,

and the third marks the specimen-transmitter bar interface. The dashed orange vertical lines identify the locations of the strain gages. The sloped lines represent the location of the wave propagation front in the X-t space. The dashed lines on either side of the first gage location are offset by a distance that corresponds to the time duration of the loading pulse. It is necessary to locate the gage such that the incident pulse stops loading the gage before the reflected pulse begins to load the gage. If the strain gage is located too close to the specimen-incident bar interface, the signals will overlap. However, if the gage is located too far from the end, there may be significant dispersion effects. There are also physical limitations associated with the setup that may dictate where the gage can be mounted. For the current work, the gages are located 0.75 m from the specimen end of the incident and transmitter bars.

3.3.2   Selection of gage type and size

Once a location for the gages was determined, the size and type of gage must be decided upon. A basic strain gage recording system was already in place and available for this work. The system consisted of an Ectron signal conditioning unit configured for 120Ω gages wired in half-bridge completion.

To select the size gage, several items were considered. With smaller gages, there is less of an averaging effect, so they tend to be able to measure higher frequency signals. However, there are physical difficulties associated with the mounting of smaller gages. It is much more difficult to reliably attach lead wires to small gages. Smaller gages also tend to exhibit degraded performance in terms of maximum allowable strain. On the

other hand, larger gages have more of an averaging effect. As the gage length increases, the frequency response of the gage decreases. This is illustrated schematically in Fig. 3.3.
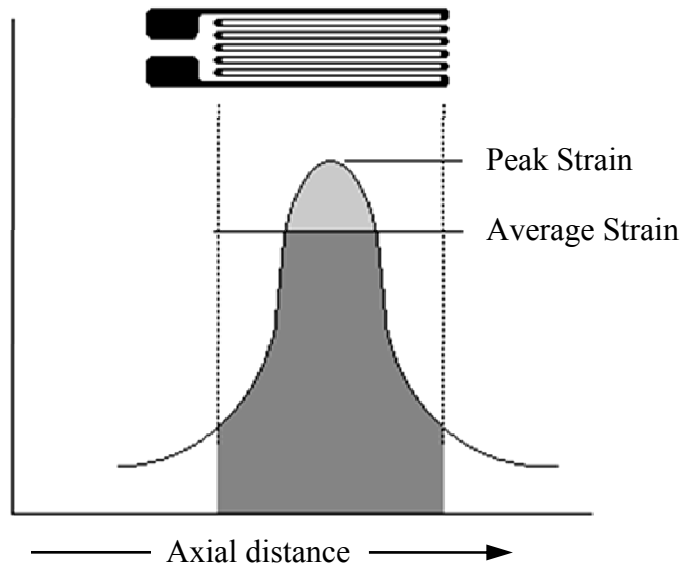
Figure 3.3: Peak vs. average strain (from *Vishay Measurements Group*)

Considering a harmonic wave that is the form of a cosine function, the peak value of the wave is located at the center, and the average can be found by integrating across the period.

$$\varepsilon_{MEASURED} = \frac{C_0}{L} \int_{\frac{-2C_0}{L}}^{\frac{2C_0}{L}} \cos(2\pi ft)dt .$$

(3.20)

Thus, for a cosine function with amplitude of unity, the measured strain will be,

$$\varepsilon_{MEASURED} = \frac{C_0 \sin\left(\dfrac{\pi L f}{C_0}\right)}{\pi L f},\tag{3.21}$$

where L is the gage length, f is the frequency, and C_0 is the wave speed. Figure 3.4 shows the frequency response for a number of different potential gage lengths available for this setup. It was determined that a gage length of 1.5 mm would be a suitable choice for this application.
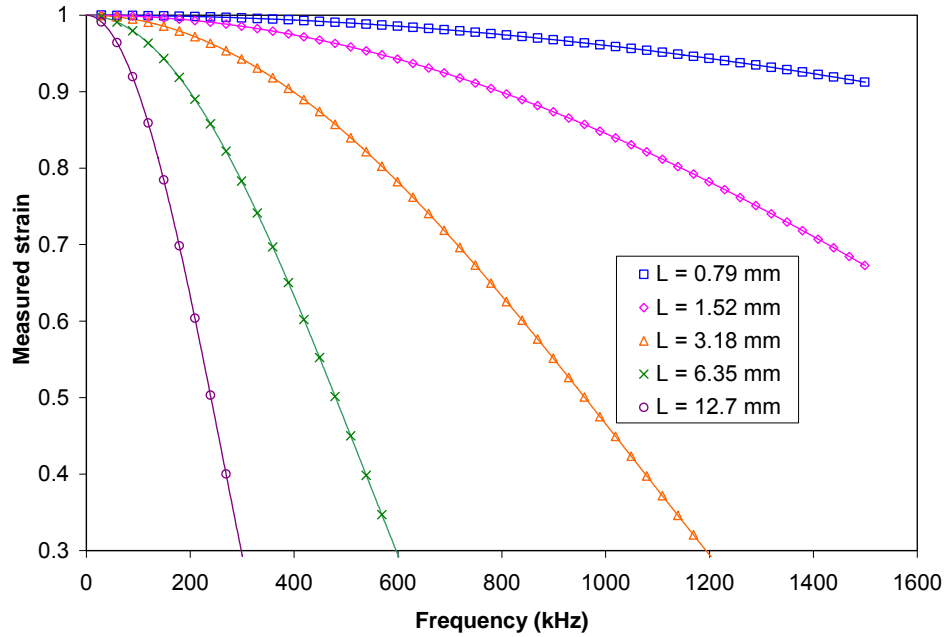
Figure 3.4: Frequency response of strain gages of various lengths

3.4   Data acquisition system details

The strain gages selected were wired in a half-bridge configuration. The working principle of a half-bridge configuration is as follows. Given a Wheatstone bridge circuit as shown in Fig. 3.5, resistors R_1 and R_2 can be replaced by strain gages. The strain gage in the R_1 arm measures the strain, while the strain gage in the R_2 arm (which is mounted on a similar material as the gage in R_1 but remains unloaded) is used to compensate for temperature fluctuations. For the bridge circuit, the change in voltage, V_0 can be computed by $\Delta V_0 = \dfrac{V_S}{4}\left[\dfrac{\Delta R_1}{R_1}+\dfrac{\Delta R_2}{R_2}+\dfrac{\Delta R_3}{R_3}+\dfrac{\Delta R_4}{R_4}\right]$ where V_S is the excitation voltage and each ΔR denotes a change in resistance and thus a change in voltage. For this particular configuration (half-bridge with temperature compensation) R_2, R_3, and R_4 experience no strain from the loading process. Thus, the change in voltage becomes $\Delta V_0 = \dfrac{V_S}{4}\left[\dfrac{\Delta R_1}{R_1}\right]$.
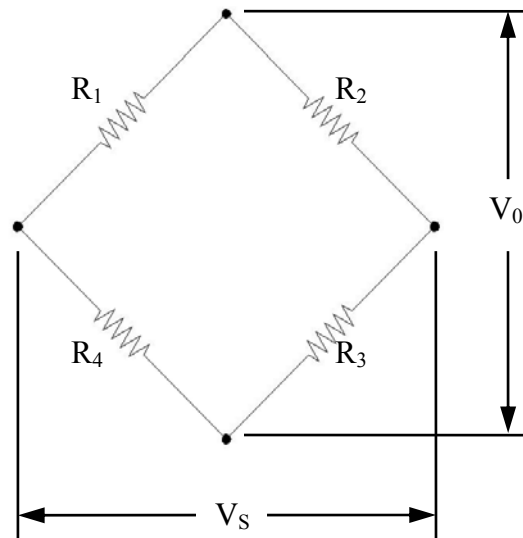
Figure 3.5: Wheatstone bridge circuit

The voltages recorded can be transformed into strains. First, dividing the raw voltage by the channel gain gives the voltage drop across the gage, ΔV_0. Since the gage factor is related to the strain as, $GF = \dfrac{\dfrac{\Delta R}{R}}{\varepsilon}$, the change in resistance is $\dfrac{\Delta R}{R} = \varepsilon GF$. So the original expression from the half-bridge configuration becomes $\Delta V_0 = \dfrac{\varepsilon V_S GF}{4}$. Finally, this can be rearranged for the strain, ε. Thus, for a measured voltage, $V_{MEASURED}$, channel gain of $G_{CHANNEL}$, an excitation voltage of V_S, and a gage factor of GF, the final relationship can be written as,

$$\varepsilon = \frac{4 V_{MEASURED}}{V_S G_{CHANNEL}(GF)}. \tag{3.22}$$

Ectron Model 563H signal conditioning units were used to filter and amplify the signal. These cards operate from DC to 200 kHz bandwidth, gain adjustable from 1 to 1000, and excitation voltage adjustable to a maximum value of 15V. To record the voltages into a computer, a PCI-6110 card from National Instruments was used. This provided 12-bit resolution at 5 MHz sampling frequency. A BNC-2110 card was used to interface the Ectron signal conditioner to the PCI card.
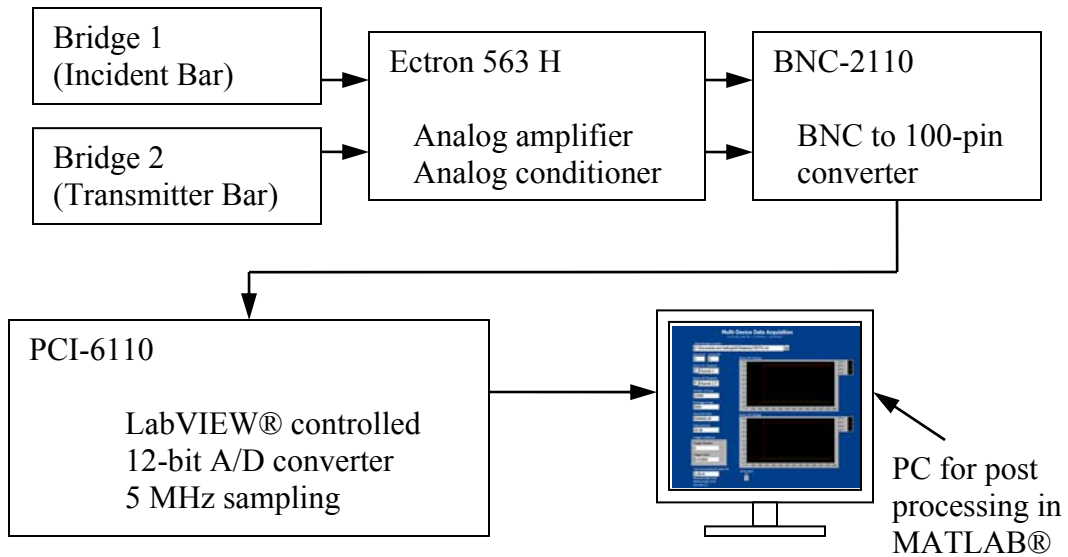
Figure 3.6: Flow chart for data acquisition system

A virtual instrument was created in LabVIEW® to record the voltage signals. The program provides a number of features for the user. It is configurable for up to 8 individual channels on two separate devices. The channels are acquired completely synchronously (i.e., sample n on channel m is acquired at exactly the same time as sample n on channel $m+1$). The user specifies the file name and location for storage, the sampling rate, the total number of scans, the total scans to record prior to the trigger event (pre-trigger scans), the trigger channel, and the trigger level. The data is recorded into an Excel® file where the first column is sample time in seconds, the second column is sample time in either seconds, microseconds, or milliseconds, columns 3 through 6 are the voltages for channels 1 through 4 on device 1, and columns 7 through 10 are the voltages for channels 1 through 4 on device 2 respectively. A screenshot of the final application is shown in Fig. 3.7. The block diagram for this program is shown in App. A.
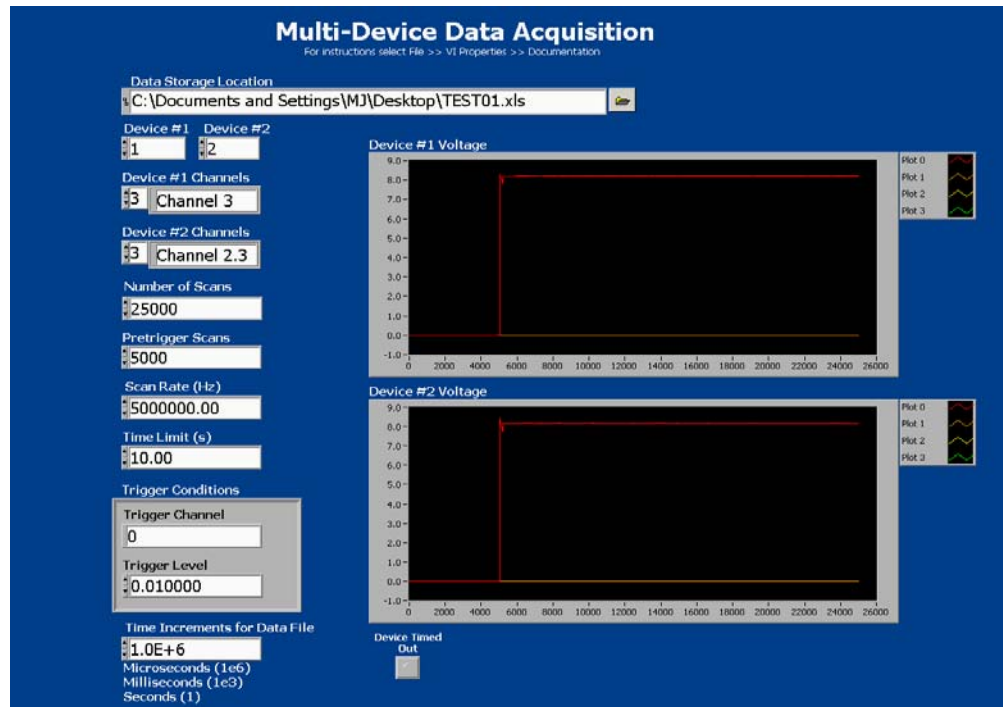
Figure 3.7: Data acquisition virtual instrument

3.5   Post processing

3.5.1   Notes on wave propagation

There are problems associated with wave dispersion that can often require compensation. Dispersion occurs as the wave propagates through the elastic media. Due to the short rise time and the general step nature of the impact event associated with split Hopkinson bar testing, the elastic wave will have some very high frequency content. It has been shown that the phase velocity of a wave varies with its wavelength and thus with its frequency, especially for the case of a long cylindrical bar. Bancroft [14], among others, demonstrated this numerically for cylindrical bars much the same as is used in split Hopkinson bar testing. In an elastic medium like that of the pressure bar setup, the

59

higher frequencies travel at slower velocities. The lower frequency waves maintain a velocity approaching the one dimensional elastic wave velocity. Since the lower frequencies travel at one velocity and the higher frequencies travel at a lower velocity, the wave tends to spread out or disperse. Hence, a strain gage must be placed at a distance close enough to the end of the bar such that dispersion is not a significant issue, yet far enough away from the end of the bar such that the distinct incident and reflected signals can still be discerned. This is particularly important in bars made of viscoelastic materials (polymeric bars). In a setup consisting of aluminum bars, it does not have as much of an effect.

The dispersion correction can be implemented in the frequency domain. First, a strain signal is measured at a known distance from the specimen-bar interface. The Fourier transform must be performed on the signal. Since the dispersion occurs due to changes in the phase velocity, this correction can be made simply by shifting the phase content of the wave by some calculated amount. Several researchers have demonstrated this including Follansbee and Frantz [26], as well as Lifshitz and Leber [27]. The shift values are computed as a function of frequency. The Fourier transform of a function, $f(t)$, is given by,

$$f(t) = \frac{A_0}{2} + \sum_{n=1}^{\infty} D_n \cos(n\omega_0 t - \delta),$$ (3.23)

where A_0 and D_n are Fourier coefficients, δ is the phase shift, and ω_0 is the fundamental frequency. The new time of interest, t', can be computed by shifting the time,

$$t' = t + \frac{z}{C_0}.$$ (3.24)

In Eq. 3.24, z is the propagation distance and C_0 is the bar wave speed of the propagation media. Substituting this expression for t in the Fourier transform equation, we can arrive at the following for the phase shift,

$$\delta = \frac{n\omega_0 z}{C_0}\left(\frac{C_0}{C_n} - 1\right).$$

(3.25)

In Eq. 3.25, C_n is the wave velocity for a particular frequency. Pochhammer [11] and Chree [12] independently studied the equation of motion for a sinusoidal wave propagating in an infinitely long cylinder. Their solution is in the following equation,

$$\frac{4\pi^2}{\Lambda^2}\left(\frac{\rho C_p^2}{\mu} - 2\right)J_1(gR)\left[2\mu\frac{\partial^2 J_0(gR)}{\partial R^2} - \frac{\lambda\rho C_p^2 4\pi^2}{\Lambda^2(\lambda + 2\mu)}J_0(gR)\right]$$
$$+ \frac{16\pi^2\mu}{\Lambda^2}\frac{\partial J_0(gR)}{\partial R}\frac{\partial J_1(hR)}{\partial R} = 0$$

(3.26)

where,

$$g = \frac{\Lambda}{2\pi}\sqrt{\frac{\rho C_p^2}{\lambda + 2\mu} - 1},$$

(3.27)

$$h = \frac{\Lambda}{2\pi}\sqrt{\frac{\rho C_p^2}{\mu} - 1}.$$

(3.28)

In Eq. 3.26, J_0 and J_1 are Bessel functions of the first kind of zero order and first order, respectively, R is the bar diameter, μ and λ are Lame's constants, C_p is the velocity of propagation, ρ is the material density, and Λ is the wavenumber. The solutions to these equations have been studied by multiple investigators for several modes of vibration. Davies [9] established that only solutions for the fundamental mode of vibration are necessary for analysis of propagation in the split Hopkinson bar setup. The relationship between wave velocity and frequency for the first mode of vibration is shown in Fig. 3.8

for different Poisson's ratios. Frequencies between 1 MHz and 2 MHz drop off substantially in velocity.
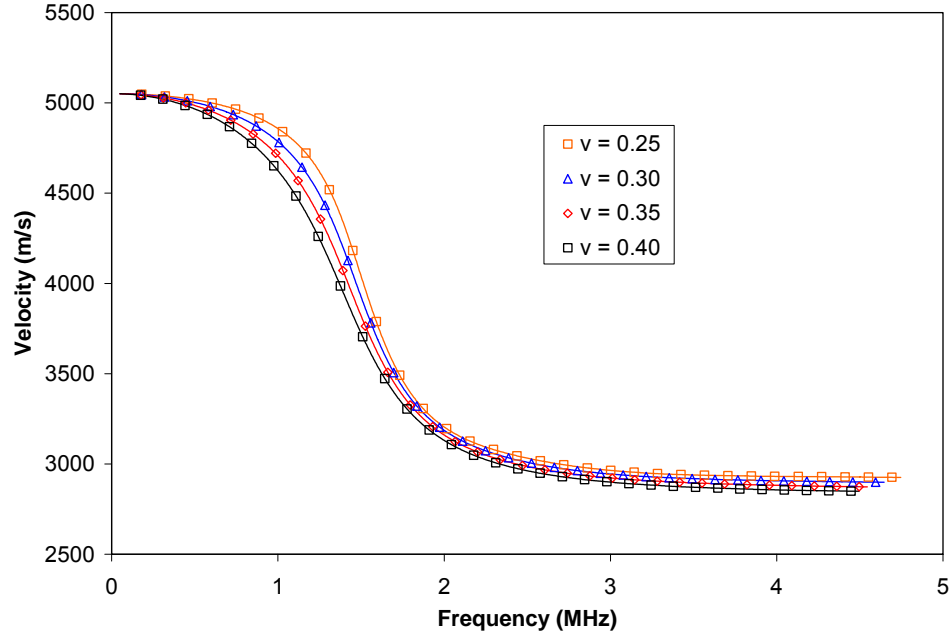
Figure 3.8: Wave speed as a function of frequency

Once the shift values, S(ω), are determined, the phase shift can be implemented in the following fashion:

$$F_S[n] = F[n]\{\cos(S[n]) - i\sin(S[n])\}.$$ (3.29)

In Eq. 3.29, $F[n]$ is the nth shifted frequency component, $F[n]$ is the original n^{th} frequency component and $S[n]$ is the phase angle in radians by which to shift that particular frequency component. Once the shifting has been accomplished, the inverse Fourier transform can be computed, producing the propagated signal.

Since the dispersion correction is implemented in the frequency domain, some information may be lost by performing the transforms and inverse transforms. Thus, it is necessary to examine the frequency content of a typical signal from the configuration used in the present work to determine whether or not it is necessary to implement the propagation. The frequency spectrum is shown (Fig. 3.9) for a signal recorded from one of the experiments done.
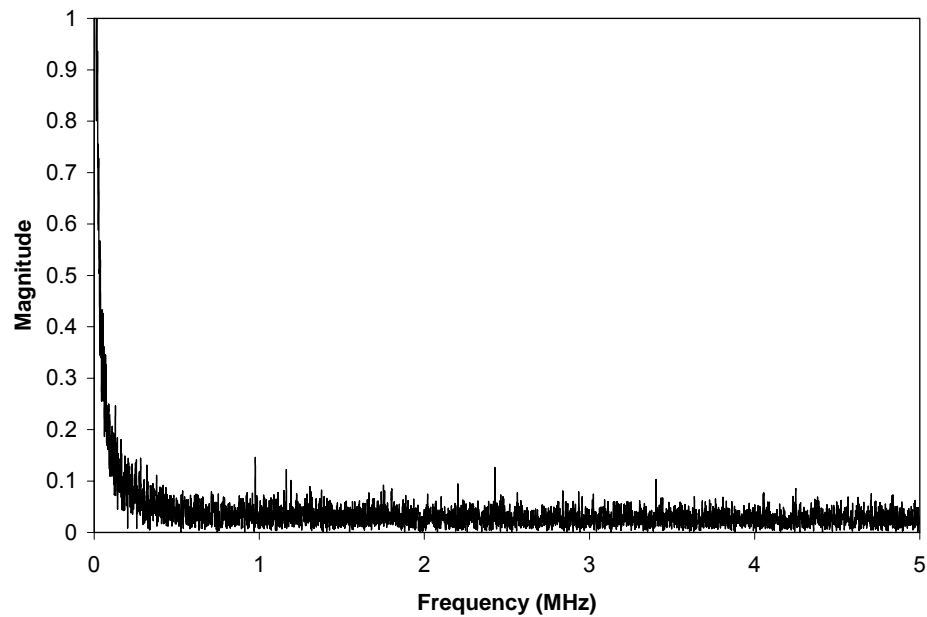
Figure 3.9: Typical signal frequency content

Note that the magnitude is asymptotic below about 0.5 MHz. Since the velocity does not start dropping off until about 1 MHz, it is not necessary to phase shift the signals in the current work. Phase shifting becomes necessary in setups where the signal is measured at a very large distance from the end, and also in setups where the signal has a

much lower rise time. Setups with viscoelastic bars (polymeric) also often require accounting for dispersion.

3.5.2 Data reduction

Since it is unnecessary to phase shift the signals, a simple MATLAB® code can be used to take the raw data, perform the necessary computations, and display the final stress-strain response for the experiment.

```
┌─────────────────────────────────────────┐
│          Read in raw data                │
└─────────────────────────────────────────┘
                    │
                    ▼
┌─────────────────────────────────────────┐
│       Prompt user to identify pulses     │
└─────────────────────────────────────────┘
                    │
                    ▼
┌─────────────────────────────────────────┐
│        Convert voltages to strains       │
└─────────────────────────────────────────┘
                    │
                    ▼
┌─────────────────────────────────────────┐
│    Compute strain rate, strain, and stress │
└─────────────────────────────────────────┘
                    │
                    ▼
┌─────────────────────────────────────────┐
│  Plot and tabulate stress-strain relationship │
└─────────────────────────────────────────┘
```
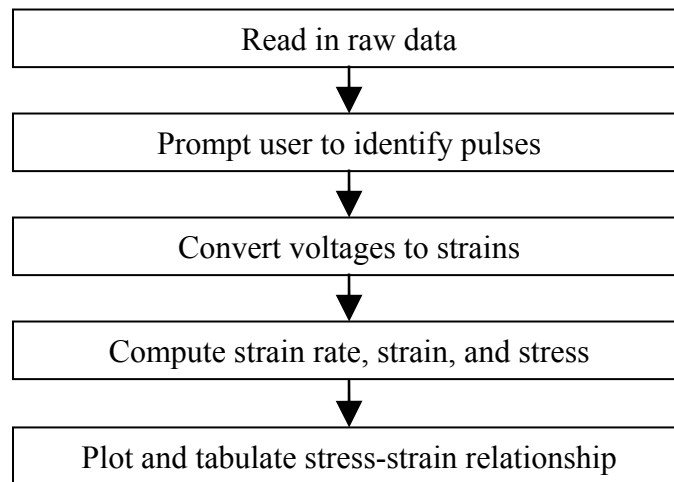
The spreadsheet file produced by the LabVIEW® program is converted into a text, tab delimited file. Once the data is read into the MATLAB® workspace, each channel is plotted and the user is prompted to identify the beginning of each individual pulse (incident, reflected, and transmitted). Once converted to strains, the computations can be made using the equations listed in the beginning of this chapter. The MATLAB® code used to accomplish this is shown in App A.

CHAPTER 4

NOTES ON VALIDITY OF EXPERIMENTAL RESULTS

4.1   Introduction

Using the split Hopkinson tension bar, tests were completed to ensure the validity of the results. First, a benchmarking experiment was completed by comparing results for a popular epoxy system with those found in the open literature. Secondly, experiments were completed to determine the repeatability of the process. Third, the equilibrium conditions for the specimen were checked.

4.2   Benchmarking experiment

For the benchmarking experiments, a neat epoxy was used. EPON 828, manufactured by HEXION™ Specialty Chemicals, was cast and cured using T403 hardener (EPIKURE™ 3233). EPON™ 828 is a popular epoxy system based on a bisphenol-A derived resin. Applications of this specific epoxy range from fiber reinforced composites to aerospace adhesives. The hardening agent, EPIKURE™ 3233, is a T403-type polyoxypropylenetriamine primary amine curing agent. It was chosen for

its compatibility with the EPON™ 828 as well as the availability of mechanical property data in the open literature.

As stated in the first chapter of this thesis, Chen *et al.* [3] reported values of the tensile properties of EPON™ 828 epoxy cured with a T403 hardening agent. The samples were prepared in the manner that will be outlined in Chapter 5. A typical specimen stress history that is representative of many of the polymeric specimens tested in the present work is shown in Fig. 4.1. Figure 4.2 compares the stress-strain response for the quasi-static case as well as the dynamic case. For the experiment performed using the split Hopkinson tension bar, the strain rate was approximately 1300 s^{-1}.
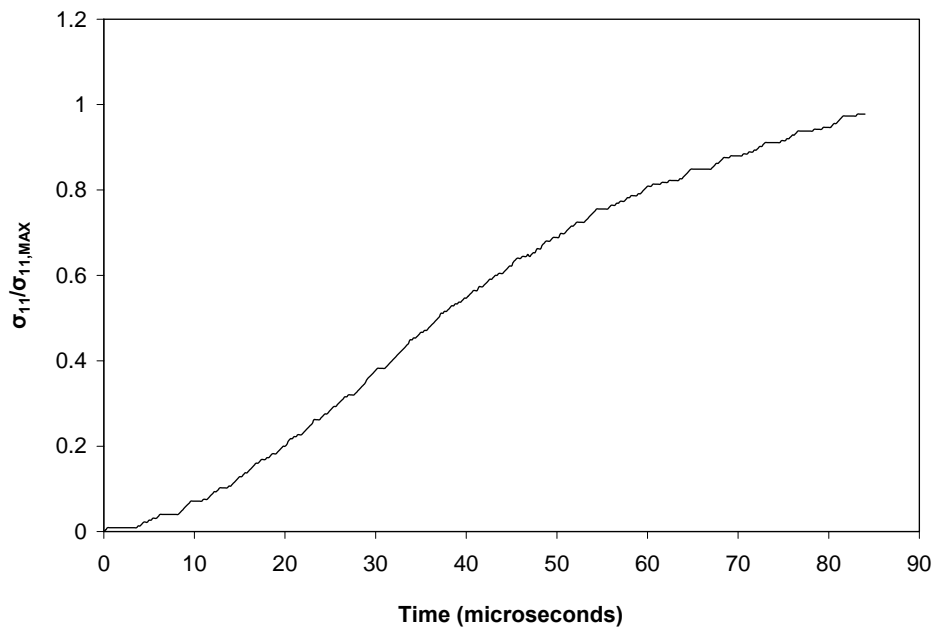
Figure 4.1: Typical specimen stress history
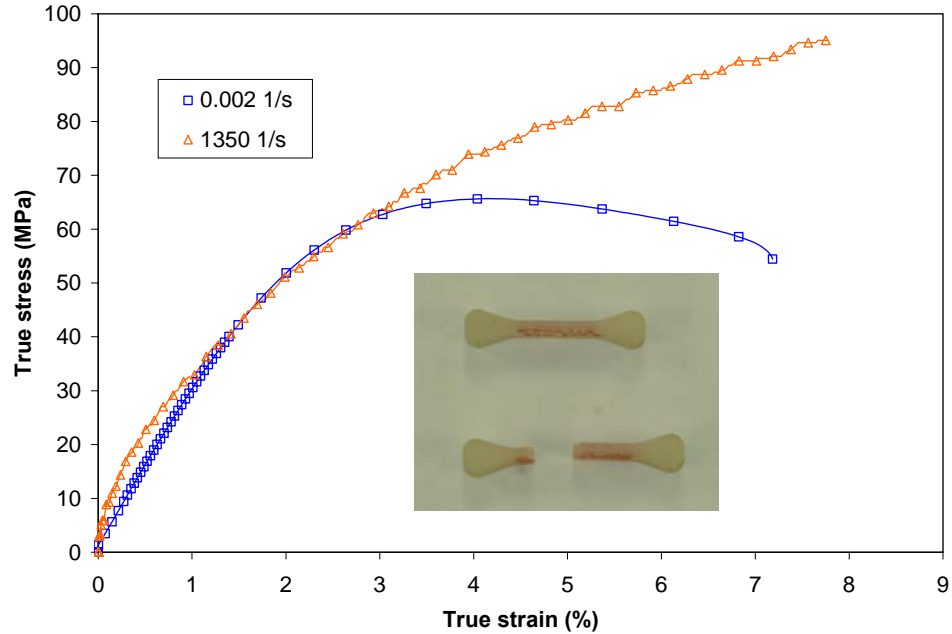
Figure 4.2: Quasi-static and dynamic stress-strain response for EPON 828™ epoxy

For the sake of comparison with the results reported by Chen *et al.*, the values were converted to true stress and strain using the constant volume assumption. Chen *et al.* reported values of approximately 8.5% true strain at failure for the quasi-static case (for a strain rate of 0.00246 s^{-1}) and approximately 8% true strain at failure for the dynamic case (strain rate of 1200 s^{-1}). The ultimate stresses as seen by the specimens were 70 MPa and 90 MPa for the quasi-static and dynamic cases, respectively. They commented that the test specimens failed in the fillet, and that this may have shadowed the strain rate effects. Also, due to the transient nature in the early stages of the experiment (increasing strain rate), split Hopkinson bar tests do not give reliable data for elastic modulus, thus those values are not compared.
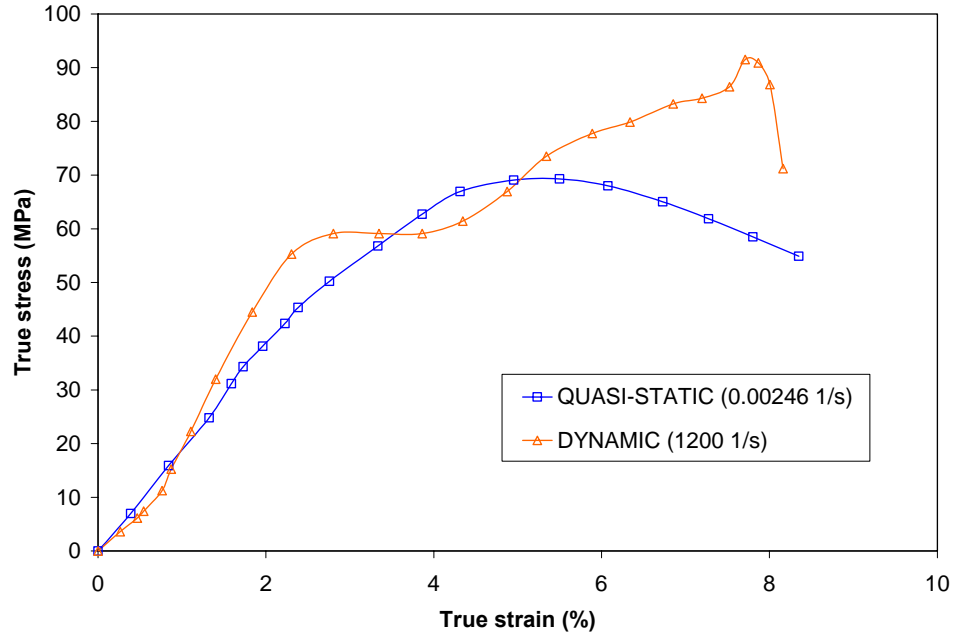
Figure 4.3: Stress-strain responses for EPON™ 828 epoxy as reported by Chen *et al.* [3]

For this work, the failure strains were slightly lower than those reported by Chen *et al.*, shown in Fig. 4.3; however, as in Chen's work, both quasi-static and dynamic experiments failed at similar strains. Also, the failure stresses were in the range of 70-90 MPa. The cure cycle could have played a major role in causing the lower failure strains observed in the present work. The specimens tested by Chen *et al.* were cured at room temperature for 7 days, while the specimens in this work were cured at room temperature for 24 hours followed by a heated cure cycle of 80ºC for 2 hours.

Overall, the data produced by the tensile SHB apparatus in this work is comparable to that found in the literature.

4.3 Experimental repeatability

To demonstrate the repeatability of the setup, several identical neat epoxy test specimens were tested under the exact same conditions. Impact velocity and specimen dimensions were all held constant. It is often difficult to obtain repeatable results in this type of test. Slight variations in the polymer can cause different failure strains and stresses to occur. Also, it is often difficult to control the exact impact velocity for the striker tube. This can change the amplitude of the loading pulse, thus causing minor fluctuations in the strain rate for the experiment. Despite these challenges, the results from this set of experiments exhibit that the apparatus is capable of producing consistent stress-strain responses. These are shown in Fig. 4.4 for three different specimens in which no specimen failure occurred in the grips.
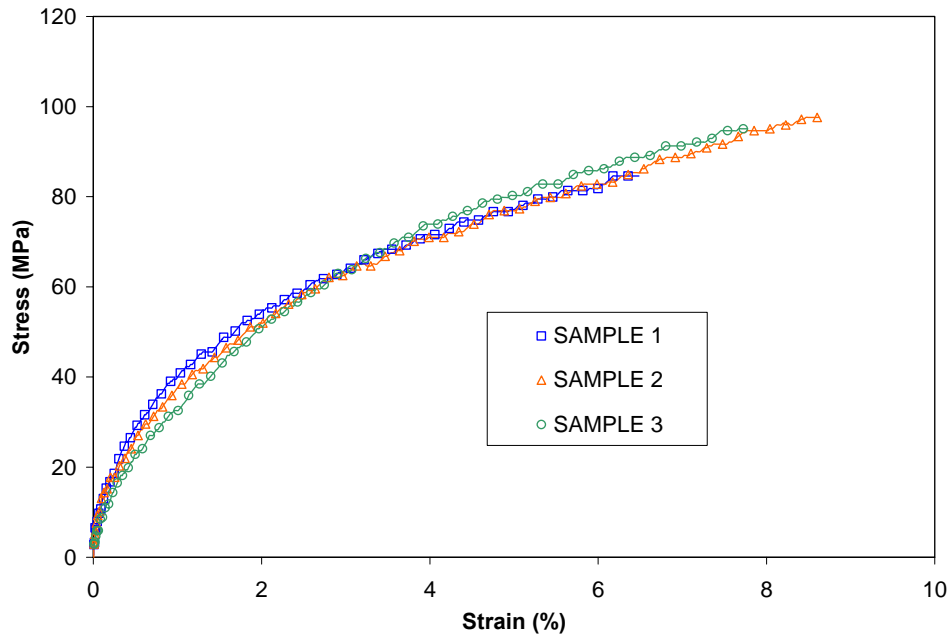
Figure 4.4: Experimental repeatability of identical EPON™ 828 epoxy test specimens

69

4.4   Equilibrium

For high strain rate testing, care has to be taken to ensure that the testing conditions are valid. One of the major criteria for this is that the specimen is in a state of dynamic equilibrium during the test. The equilibrium state is determined by comparing the stresses at each end of the gage section of the specimen. This work uses three different checks to determine the degree of equilibrium for a particular test.

The common way to check this for a split Hopkinson bar test is by comparing the stresses on the incident and transmitter ends of the specimen. This is done by calculating the specimen stress directly using the measured transmitted wave, and comparing this with the stresses found using the computed transmitted wave, $\varepsilon_T = \varepsilon_I - \varepsilon_R$.

A second way for determining the time necessary for the specimen to reach the equilibrium state is through an elastodynamic FE model. Since the density and approximate elastic modulus for the specimen are known, the stresses at two elements on opposite ends of the gage section can be compared. The difference in stresses at each end of the gage section is shown for both the FE model and experiment in Fig. 4.5. According to the three different tests, the specimens will reach equilibrium after 30-40 μs of loading.
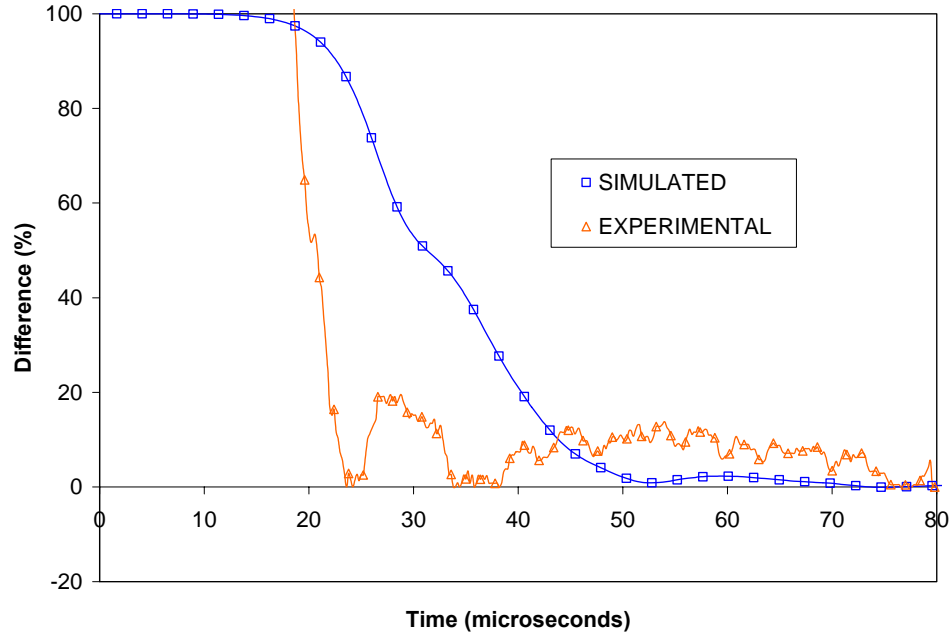
Figure 4.5: Percentage difference in stresses at incident and transmitter faces of specimen

One final way is through calculating the time it takes to reach equilibrium based on the specimen properties. It has been noted in the literature that it typically takes approximately three reverberations of an elastic wave in the specimen for the specimen to reach equilibrium. Since the gage length of the specimen is known and the approximate elastic wave speed is known, a good approximation can be made as to whether the specimen reached equilibrium prior to failure. The specimens used in this work had a gage length of 11 mm. Given an average elastic wave speed for the specimens was about 2500 m/s, it requires approximately 25 μs for the specimen to reach equilibrium in the gage section. This value is consistent with those values from the experiment and the FE model.

4.5   Upper limit on constant strain rate

Another issue, as demonstrated by Chen *et al.* [24], is that there is an upper limit on constant strain rate in split Hopkinson bar testing. The reason for this is that for a given loading pulse and strain rate history, there is an associated rise time. During the rise of the pulse, a certain amount of strain is accumulated. It is possible that this strain can reach the failure strain of the specimen prior to reaching a constant strain rate. This can be visualized by looking at an idealized trapezoidal strain rate history with a certain rise time. For this idealized pulse, the time to failure can be computed for various strain rates and failure strains. From this information, a testing envelope can be constructed for which the specimens fail at a constant strain rate. For example, given a rise time of 50 μs, strain rates ranging from 500 s^{-1} to 2000 s^{-1}, and failure strains ranging from 1% to 10%, the following contour can be computed. Negative values in the contour represent failure prior to reaching constant strain rate conditions. For this reason, it is very difficult to test specimens that have low failure strains. Firstly, it is difficult to achieve very low rise times in split Hopkinson tension bar testing. Secondly, it is difficult to attain low strain rates consistently.
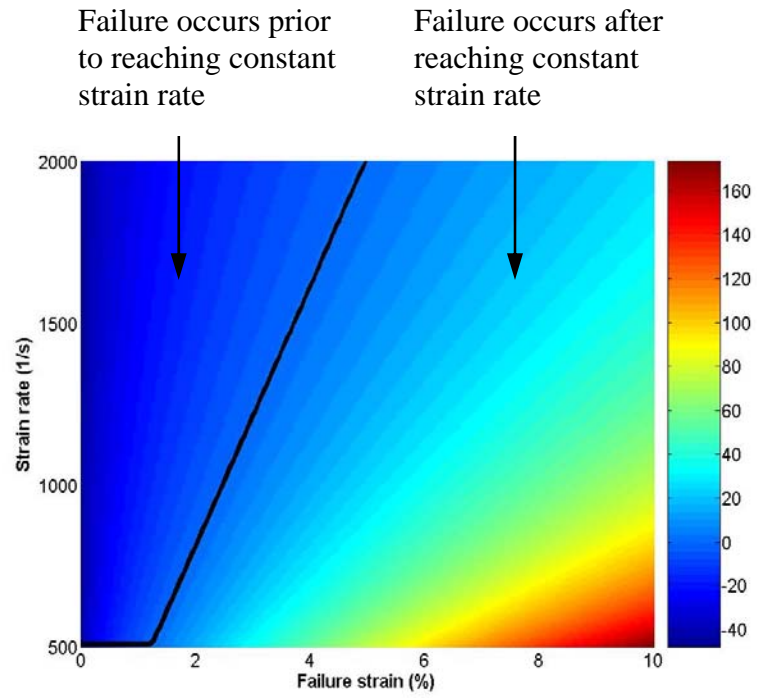
Figure 4.6: Validity envelope for constant strain rate testing

CHAPTER 5

MECHANICAL RESPONSE OF PARTICULATE COMPOSITES

5.1   Introduction

Using the split Hopkinson tension bar apparatus, an investigation of the effect of filler volume fraction and particle size on the stress-strain response of a glass-filled polymer-matrix composite was undertaken.   Secondly, the dynamic behavior of a common acrylic biocement was also investigated.   This chapter presents the results from these experiments.   Unless otherwise noted, all stresses and strains are values of engineering stress and engineering strain.

5.2   Experiments with glass-filled polymer composites

5.2.1   Specimen preparation

The specimens used in this work were made of castable two-part thermosetting polymers.   Given the geometry, the specimen could be cast into a near net shape with only a small amount of necessary finish machining, drastically reducing the processing time required for individual experiments.   In order to do this, a master specimen was machined from solid steel, next a mold cavity was produced by pouring silicone rubber

around the master specimen to create a negative of the specimen, and finally multiple castable specimens were created from the mold.

Electrical discharge machining, commonly referred to as EDM, was selected to cut the intricate shapes for the steel master specimens. Once several master specimens were machined, a rubber mold was formed around the masters. Silicone rubber was chosen as a mold material due to its ability to reproduce the fine details of the masters and for its dimensional stability after curing.

(a) (b)

(c) (d)
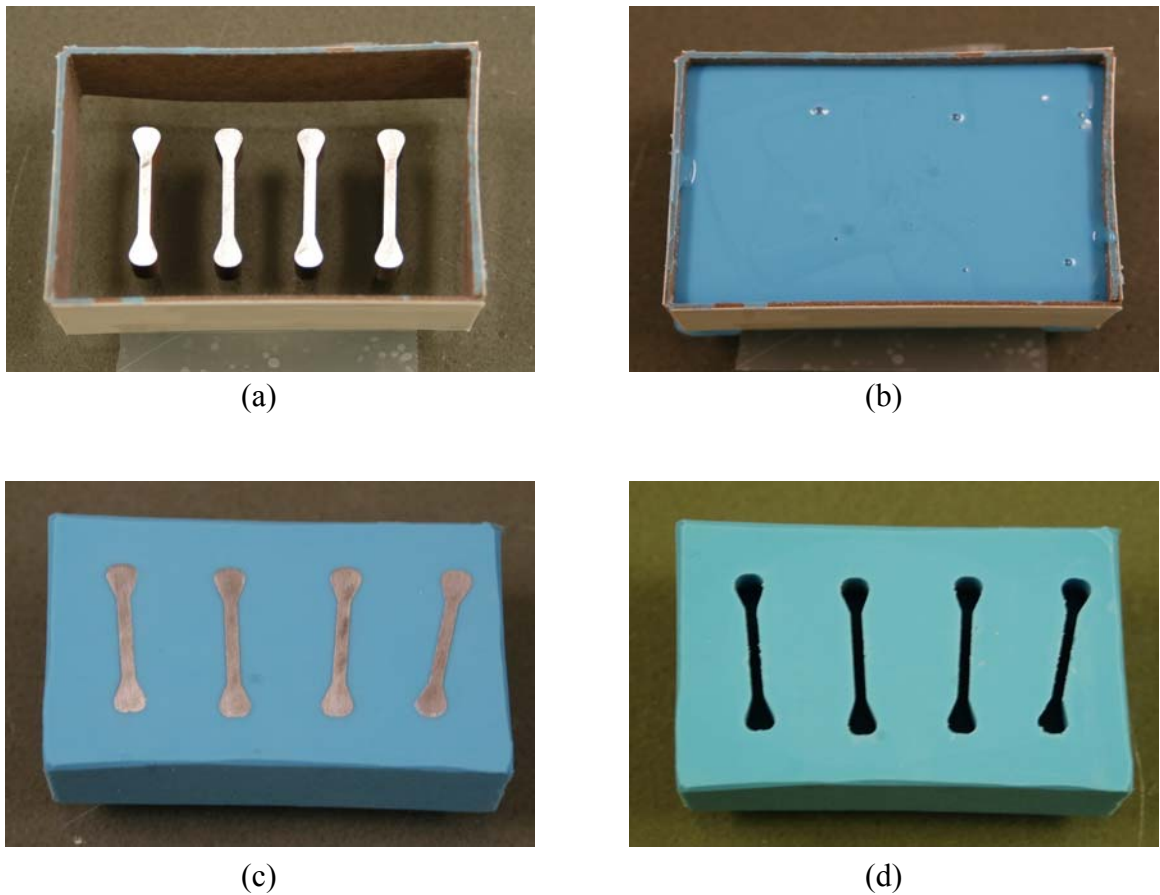
Figure 5.1: Mold fabrication process: (a) steel master specimens with cardboard barrier on glass substrate, (b) silicone rubber casting, (c) cured casting prior to removal of steel masters, (d) resultant mold cavity

The specific product used was PlatSil® 73 Series from PolyTek Development Corporation. This is a very flexible rubber mold material that has high tear strength and can be vulcanized at room temperature. It also has low shrinkage, resulting in very good dimensional stability. To create the mold, a cardboard barrier was constructed on a glass substrate. The master specimens were placed within the cardboard barrier and the silicone rubber mixture was poured and allowed to cure for 30 hours. After curing, the cardboard barrier and the master specimens were removed resulting in a precise cavity for future specimen castings.

After characterization of the neat epoxy (see chapter 4), glass particles were introduced into the polymer matrix. For a given test specimen, the general preparation sequence was as follows. First, the desired quantities of resin and glass particles were measured out and placed into an oven at 50ºC for 1 hour in order to lower the viscosity of the resin. This also allowed the particles to release any moisture. Next, the particles were mixed into the resin and placed back into the oven at 50ºC for another 2 hours. This allowed the mixture to degas while the resin remained at a relatively low viscosity. While continuing to maintain the temperature of the mixture at 50ºC, the curing agent was slowly stirred into the mixture. At this point, a portion of the mixture was poured into the dynamic specimen mold (Fig. 5.1(d)) while the remainder of the mixture was left in the mixing container. Both the mixing container and the dynamic specimen molds were then placed into a vacuum chamber. A pump was used to bring the chamber down to a pressure of -85 kPa (gage). Once at this pressure, the vacuum was released and the chamber allowed to return to atmospheric pressure. This process of vacuuming and releasing was repeated until no air bubbles were observed (typically 15 to 20 times). This

ensured full degassing of each mixture. Periodically, air bubbles were skimmed from the tops of the molds and the mixing container. After degassing, the dynamic specimen molds were set aside and the remaining mixture was poured into the quasi-static specimen molds made of plexiglass (Fig. 5.2(a)).

(a)   (b)
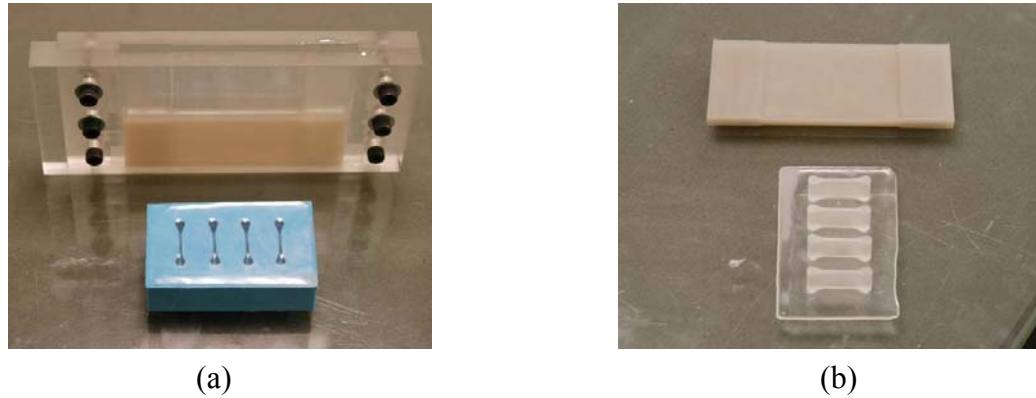
Figure 5.2: (a) Quasi-static and dynamic specimen molds and (b) demolded quasi-static and dynamic specimens
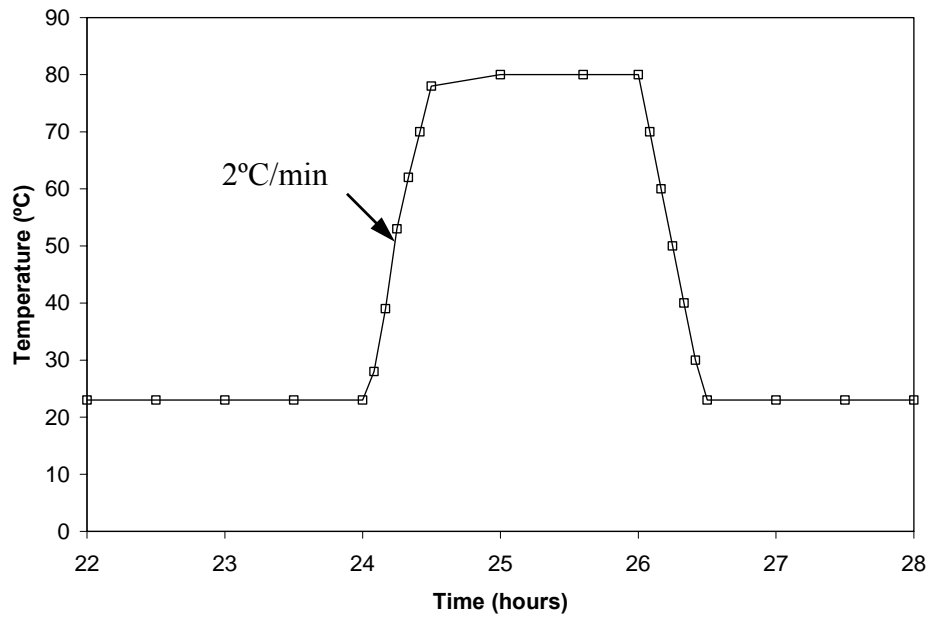
Figure 5.3: Cure cycle for test specimens

All castings for this work (quasi-static and dynamic) were allowed to cure at room temperature for 24 hours prior to being placed in an oven for the heated cure cycle shown in Fig. 5.3. Upon completion of the curing cycle, the specimens were finish machined using a bench router. Testing occurred approximately 10 days after the initial casting.

5.2.2 Filler volume fraction effect on stress-strain behavior

The first set of experiments involved varying the filler particle volume fraction. SPHERIGLASS® solid glass spheres were obtained from Potter's Industries, Inc. The mean diameter of the glass particles for this study was 25 μm. The quasi-static and dynamic tests were conducted for specimens with 0%, 10%, 20%, and 30% fill by volume. For each specimen type, at least three quasi-static tensile tests were conducted and at least four dynamic tensile tests were conducted. The longitudinal and shear wave speeds were measured using ultrasonic pulse-echo measurements. The wave speeds and specimen densities were then used to find the elastic modulus and Poisson's ratio of each specimen by solving Eqs 5.1 and 5.2 simultaneously. The specimen properties are listed in Table 5.1.

$$C_L = \sqrt{\frac{E(1-v)}{\rho(1+v)(1-2v)}} \tag{5.1}$$

$$C_S = \sqrt{\frac{E}{2\rho(1+v)}} \tag{5.2}$$

Name	Volume fraction (%)	Density (kg/m^3)	Longitudinal wave speed (m/s)	Shear wave speed (m/s)
E0000	0	1168	2458	1106
E2510	10	1301	2497	1141
E2520	20	1434	2597	1222
E2530	30	1567	2764	1356

Table 5.1: Properties for glass-filled epoxy with different filler volume fractions (25 μm diameter particles)

The specimen elastic modulus is shown plotted against volume fraction for both the quasi-static tensile tests as well as the ultrasonic measurements in Fig. 5.4. Since it is difficult to obtain reliable data for the early portion of the split Hopkinson bar experiment, ultrasonic measurements are used for determining elastic modulus.
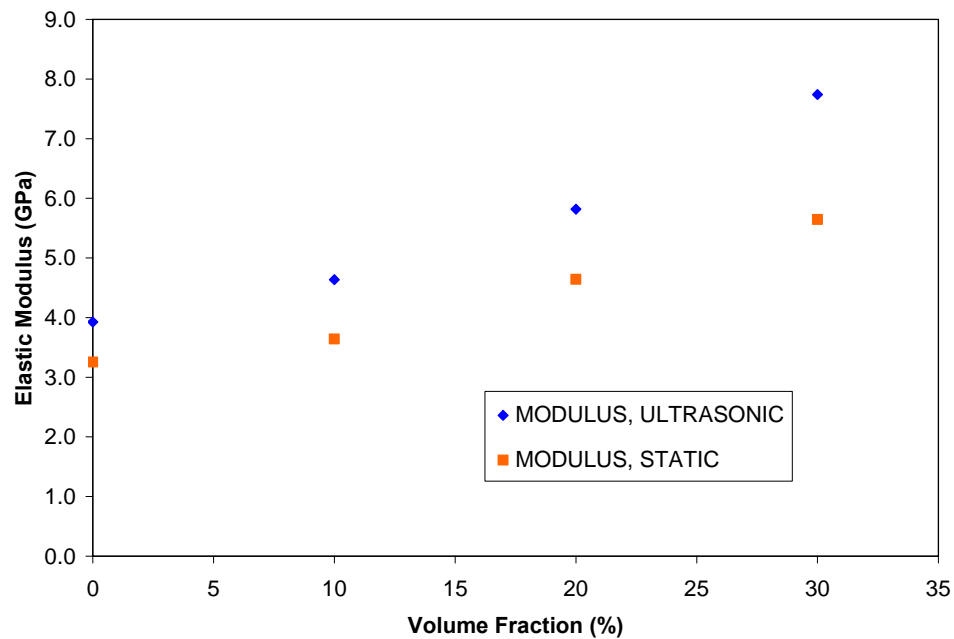
Figure 5.4: Elastic moduli for glass-filled epoxy with different filler volume fractions

79

This stiffening effect due to increasing volume fraction of glass particles in the composite has been investigated and is well supported in the literature. Ishai and Cohen [30,31] and Smith [32] were some of the earlier investigators to look at stress-strain response of glass-filled epoxy composites. The results from quasi-static experiments from the present work are shown in Fig. 5.5.
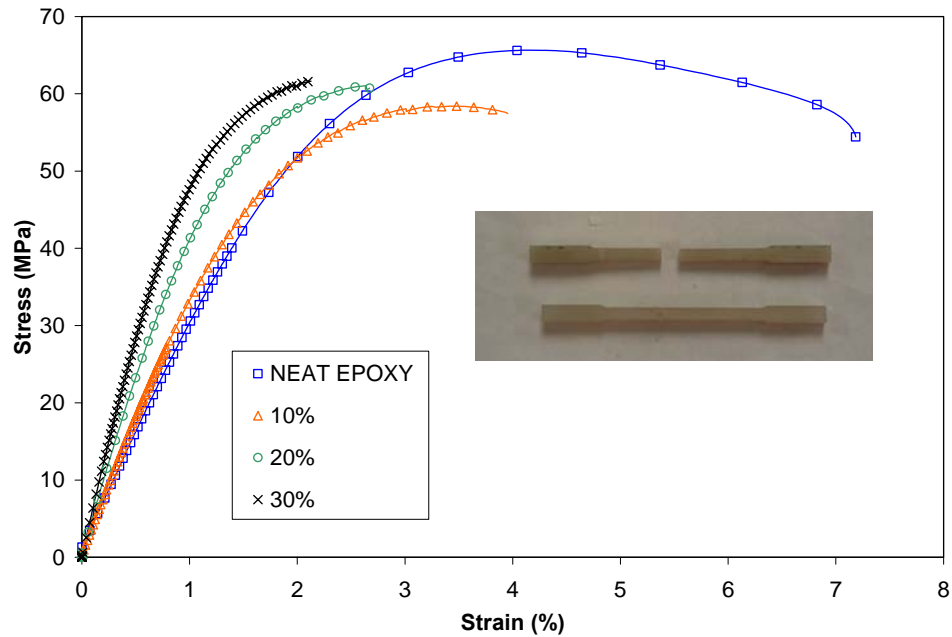
Figure 5.5: Quasi-static stress-strain response for 25 μm glass-filled epoxy with different filler volume fractions (strain rate ≈ 0.002 s^{-1})

To the knowledge of the author, the present work is the first to address the effect of strain rate on the stiffening effect of glass particles at various volume fractions. Despite being able to make a direct measurement of the elastic modulus in the dynamic case, the effect of volume fraction on the dynamic stiffness can be seen qualitatively by observing the overall stress-strain response as shown in Fig. 5.6.
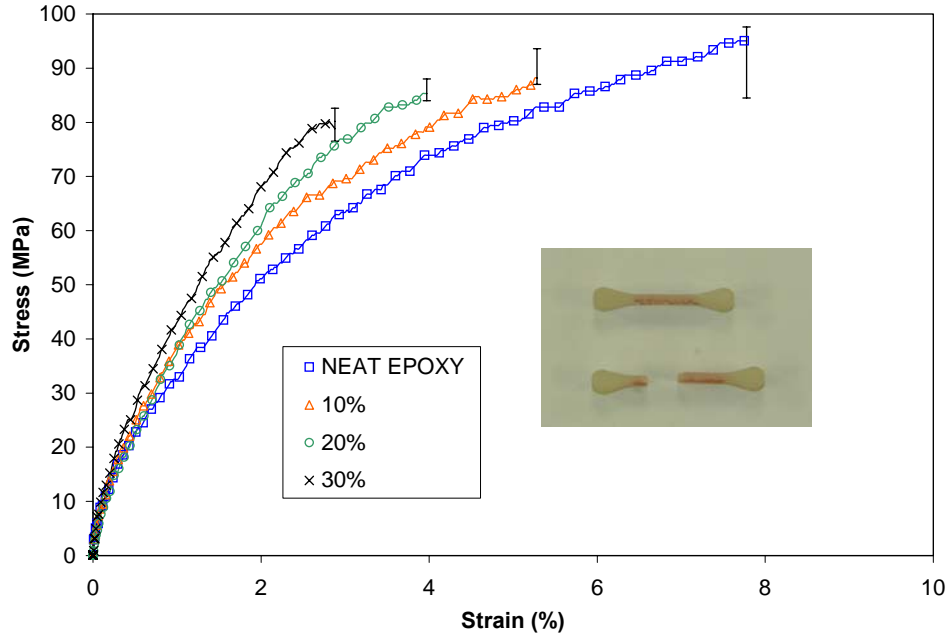
Figure 5.6: Dynamic stress-strain response for 25 μm glass-filled epoxy with different filler volume fractions (strain rate ≈ 1300 s^{-1})

In terms of peak or failure stresses, the specimens generally failed at lower stresses with increased filler volume fractions when tested under dynamic conditions. This is shown in Fig. 5.7. It is clear that there is a decrease in the peak stress values between 0% and 30% filler volume fractions. The drop is monotonic in nature. In the quasi-static load cases, the peak stresses remained nearly constant or slightly increased with filler particle volume fraction. Previous research work, particularly that by Ishai and Cohen [30,31], has shown a general increase in peak stress with volume fraction for this type of composite (polymer matrix with glass particle reinforcement) under quasi-static loading conditions as well. Besides decreasing the peak stress, increasing filler volume fraction also led to a decrease in specimen ductility. In terms of strain rate effect, dynamic peak stresses are consistently higher than the quasi-static values.

81
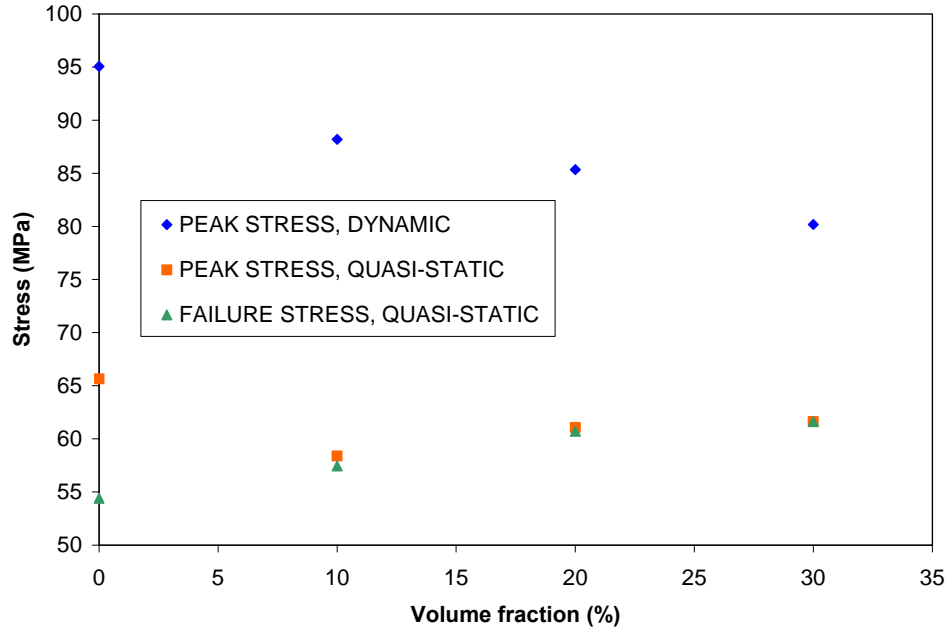
Figure 5.7: Peak and failure stresses for 25 μm glass-filled epoxy with different filler volume fractions

The decrease of peak stress with filler volume fraction under the dynamic conditions is not clearly understood due to the micromechanical complexities involved. However, interfacial debonding between the particles and the matrix due to propagating stress waves could likely result in the evolution of internal defects during a dynamic loading event. At higher volume fractions, the concentration of such defects is greater and hence lower peak stresses can be expected. A second source of the decrease in peak stress could be due to the possibility of gas entrapment. At higher fills, the mixture becomes much more viscous thus increasing the difficulty of degassing. This could introduce microscopic porosity into the material, hence lowering peak stress.

For the dynamic experiments, both volume fraction as well as strain rate play a role in the embrittlement of the specimen. It has been demonstrated [30] that at low

82

strain rates (quasi-static) these two factors are independent of each other, but it is possible that at higher strain rates, the effects become coupled. If the two variables were independent of one another, the change in peak stress with respect to strain rate, should remain constant across the range of volume fractions. However, this quantity changes with different volume fractions (Fig. 5.8). Such a coupling of the two effects could play a role in causing the decreased peak stress with increased volume fraction of the filler.
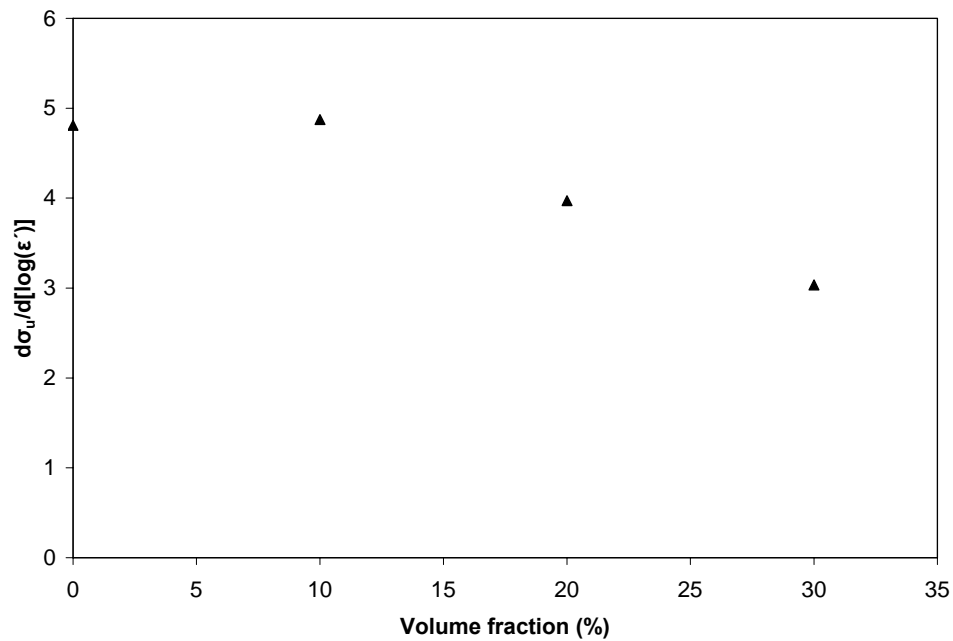
Figure 5.8: Coupling effect of strain rate and filler volume fraction

In general, the specific energy absorbed by each specimen decreased with volume fraction in both the quasi-static and dynamic loading conditions. Energy dissipated by dynamic test specimens was consistently higher than the corresponding quasi-static ones over the range of volume fractions studied. This is shown in Fig. 5.9. As the particle volume fraction increases, there is a reduction in the amount of plastic deformation that

occurs. Since a large portion of energy is absorbed during the plastic deformation regime, when the ability to undergo plastic deformation is removed, the total energy is reduced.
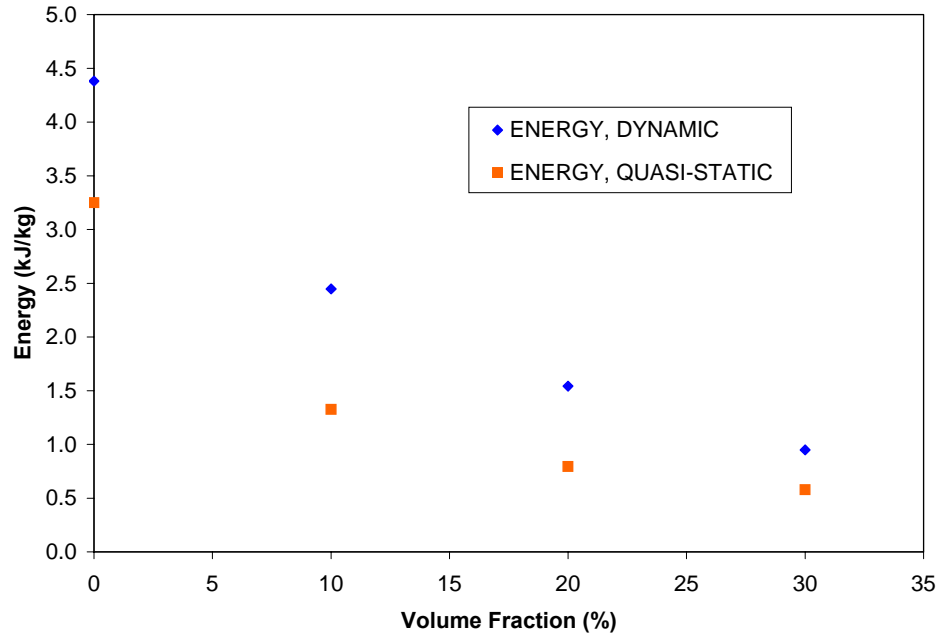
Figure 5.9: Specific energy absorption for 25 μm glass-filled epoxy with different volume fractions

5.2.3   Predictions based on micromechanics

Several models have been developed to predict elastic properties of composites based on the known properties of the matrix and inclusions. In addition, several investigators have made suggestions as to the prediction of failure properties based on empirical methods, as well as finite element models and some probabilistic approaches.

The Mori-Tanaka model is commonly used to describe the relationship between elastic modulus and filler volume fraction. The model, as described by Weng [36], is

shown in Eqs. 5.3 and 5.4 where subscripts m and i denote the 'matrix' and 'inclusion', respectively. Lame's constants are dentoted by κ and μ. Elastic modulus, E, is computed using $E = \dfrac{9\kappa\mu}{3\kappa+\mu}$.

$$\kappa = \kappa_m \left(1 + \frac{V_f}{\frac{3(1-V_f)\kappa_m}{3\kappa_m+4\mu_m} + \frac{\kappa_m}{\kappa_i-\kappa_m}} \right) \tag{5.3}$$

$$\mu = \mu_m \left(1 + \frac{V_f}{\frac{6(1-V_f)(\kappa_m+2\mu_m)}{5(3\kappa_m+4\mu_m)} + \frac{\mu_m}{\mu_i-\mu_m}} \right) \tag{5.4}$$

Another popular model for describing the volume fraction effect on elastic modulus is the Hashin-Shtrikman model. This model predicts upper and lower bounds for the values of elastic modulus. As presented by Ravichandran [37], Eqs. 5.5 and 5.6 are used to compute the Lame's constants of the composite. For the present work, only the lower bounds (superscript l) were computed and plotted. Subsequently, the elastic modulus is computed from Lame's constants.

$$\kappa_c^l = \kappa_m + \frac{V_i}{\frac{1}{(\kappa_i-\kappa_m)} + \frac{3V_m}{(3\kappa_m+4\mu_m)}} \tag{5.5}$$

$$\mu_c^l = \mu_m + \frac{V_i}{\frac{1}{(\mu_i-\mu_m)} + \frac{6(\kappa_m+2\mu_m)V_m}{5\mu_m(3\kappa_m+4\mu_m)}} \tag{5.6}$$

As evidenced in Fig. 5.10, both of these models predict the elastic response to filler volume fraction reasonably well for both the quasi-static values as well as the values from ultrasonic measurements.
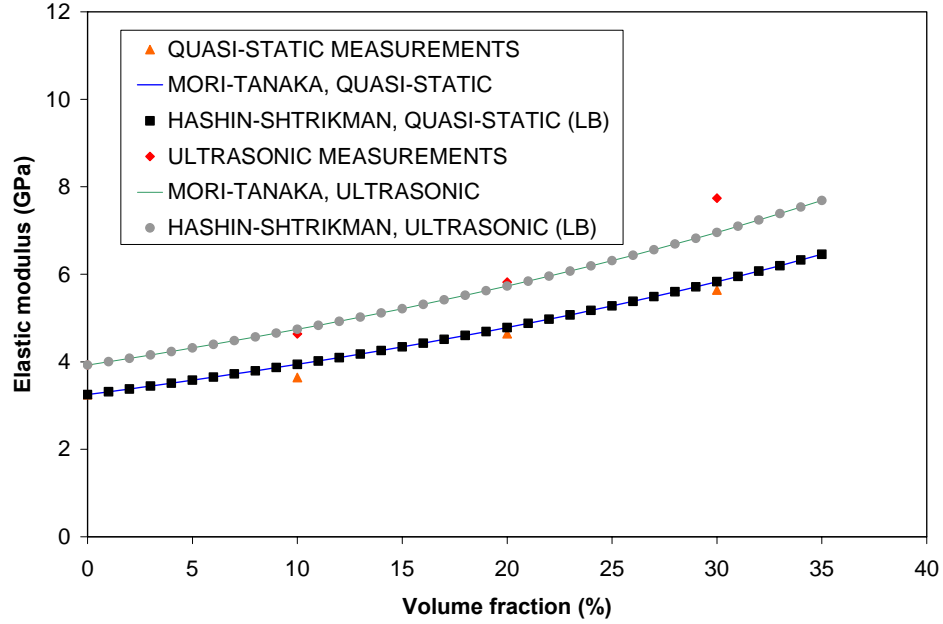
Figure 5.10: Comparison of experimental elastic moduli with analytical predictions

In terms of stress, several models have been proposed to better quantify the effect of filler volume fraction on failure stress. One such model, suggested by Piggott and Leidner [38], assumed that failure stress was dependant on filler volume fraction in a linear sense. They commented that some relationship of the form $\dfrac{\sigma_u}{(\sigma_u)_m} = K - bV_f$ was adequate for describing the behavior. In this case, K was a stress concentration factor and b was a constant dependant upon particle-matrix adhesion strength. The negative value suggests that weakly bonded filler lowers σ_u of the composite of a known V_f. The failure stress of the unfilled matrix is denoted as $(\sigma_u)_m$ and the failure stress of the composite is denoted as σ_u. Another model, proposed by Nicolais and Mashelkar [39], argued that a relationship of the form $\dfrac{\sigma_u}{(\sigma_u)_m} = 1 - bV_f^n$ was more appropriate. They recommended that

positive values of *b* and values of *n < 1* were sufficient to represent the behavior. Specifically, they suggested that *b = 1.21* and *n = 2/3* for glass-filled polymers. Both of these models are predominately empirical in nature. A third model, derived by Schrager [40], took more of a probabilistic approach. In this case, $\frac{\sigma_u}{(\sigma_u)_m} = e^{-rV_f}$ where *r* is computed based on the particle diameter, *R*, as well as the interphase distance, *ΔR*. Schrager considers the interphase distance as the portion of the matrix that is affected by the addition of the fillers due to local stress concentrations. Specifically, $r = (v_i + v_p)/v_p$ where $v_i = 4\pi(R + \Delta R)/3$ and $v_i = 4\pi R/3$. Each of these models is shown in Fig. 5.11.
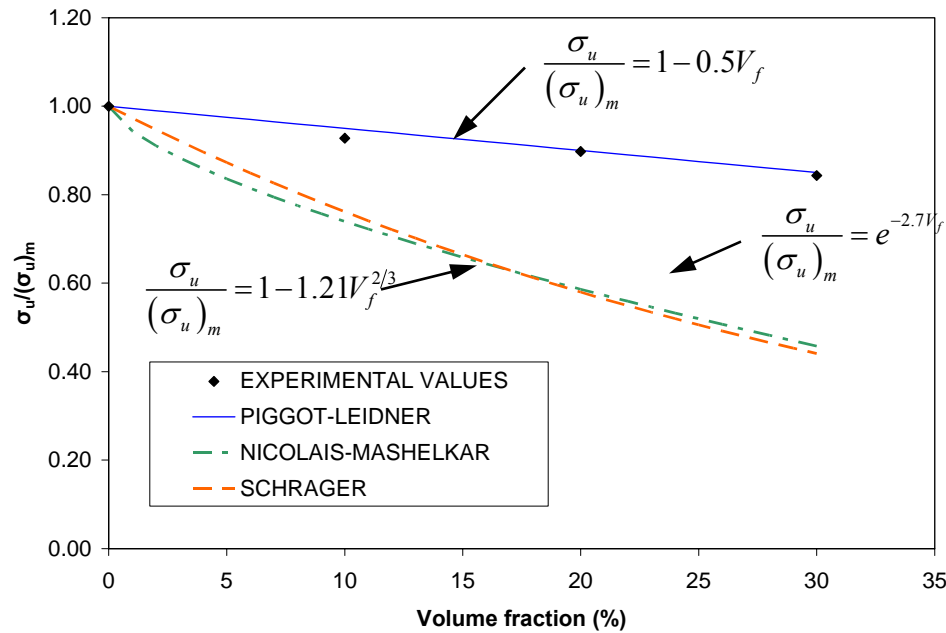
Figure 5.11: Comparison of strength values with previous empirical models

For the current work, none of these models had outstanding agreement with the experimental values, although the model proposed by Piggot and Leidner [38] could capture the experimental trend for a fitted value of $k = 1$ and $b = 1/2$. Hence, an alternative model is explored. From Fig. 5.10, it is evident that the elastic modulus is related to the square of the volume fraction through some constants, or $E \propto V_f^2$. From experimental observations, the failure stress was inversely proportional to the elastic modulus, or $\sigma_u \propto E^{-1/3}$. From these two relationships, it follows that $\sigma_u \propto V_f^{3/2}$. Thus, a relationship of the form $\dfrac{\sigma_u}{(\sigma_u)_m} = c_1 + c_2 V_f^{3/2}$ is necessary to describe the behavior of failure stress with respect to filler volume fraction. This is demonstrated in Fig. 5.12. The necessity of the constant c_1 is related to the decrease in strength of the matrix with the initial introduction of the filler particles.
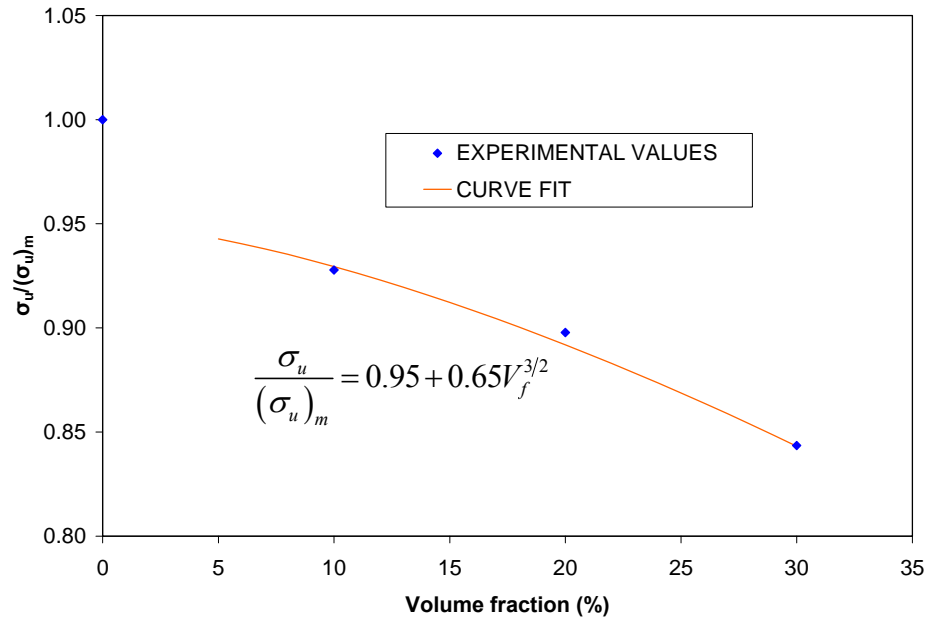
Figure 5.12: Comparison of strength values with the proposed empirical model

88

5.2.4 Particle size effect on stress-strain behavior

In addition to studying the effect of volume fraction, a brief investigation of particle size effect was also undertaken. In this study, the volume fraction was held constant at 10%, while particles with mean diameters of 11 μm, 25 μm, 35 μm, and 42 μm were used in the composite. Once again, ultrasonic measurements were used along with Eqs 5.1 and 5.2 to obtain the elastic modulus and Poisson's ratio of each specimen. The measured specimen properties are listed in Table 5.2. The stiffness remains nearly constant for the various particle sizes since the volume fraction remains constant. This is evidenced in Figs. 5.13 and 5.14. The quasi-static stress-strain response for the glass-filled epoxy specimens with different particle sizes was almost identical. The largest particle size (42 μm) failed at a lower strain than the others; however, despite a number of unsuccessful attempts, failure occurred in the grip for this particle size.

Name	Particle size (μm)	Density (kg/m^3)	Longitudinal wave speed (m/s)	Shear wave speed (m/s)
E0000	0	1168	2458	1106
E1110	11	1301	2497	1141
E2510	25	1301	2509	1157
E3510	35	1301	2484	1145
E4210	42	1301	2502	1145

Table 5.2: Specimen properties for glass-filled epoxy with various filler particle diameters (10% filler volume fraction)
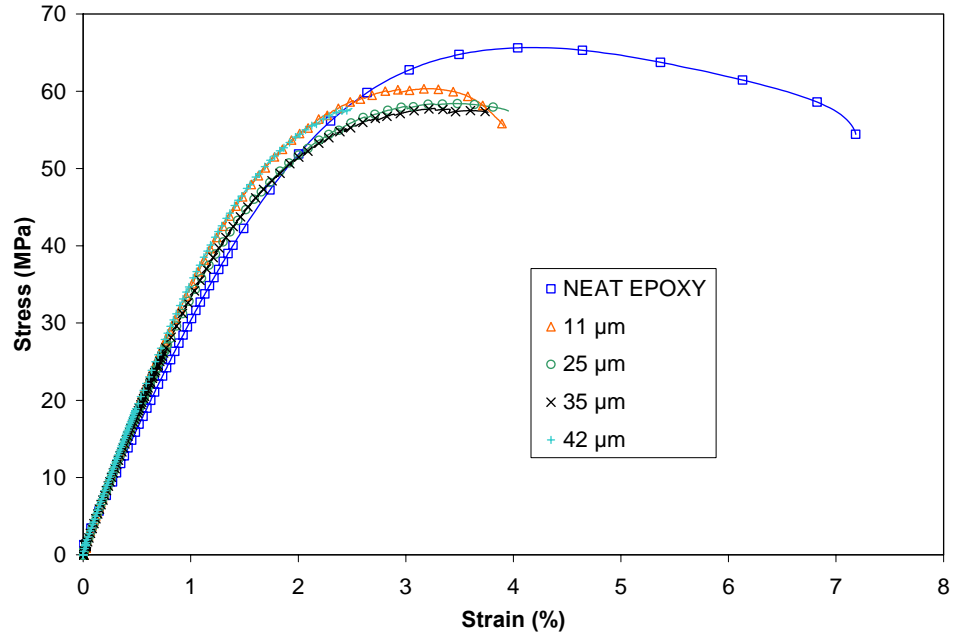
Figure 5.13: Quasi-static stress-strain response of 10% volume fraction glass-filled epoxy with different particle sizes (strain rate $\approx$ 0.002 s^{-1})
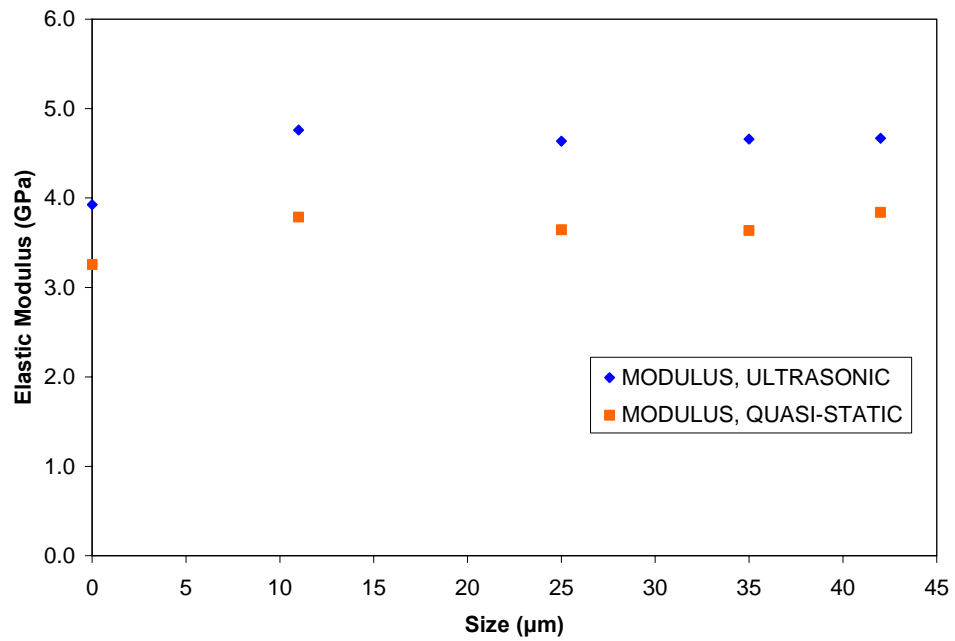
Figure 5.14: Elastic modulus of 10% volume fraction glass-filled epoxy with different particle sizes
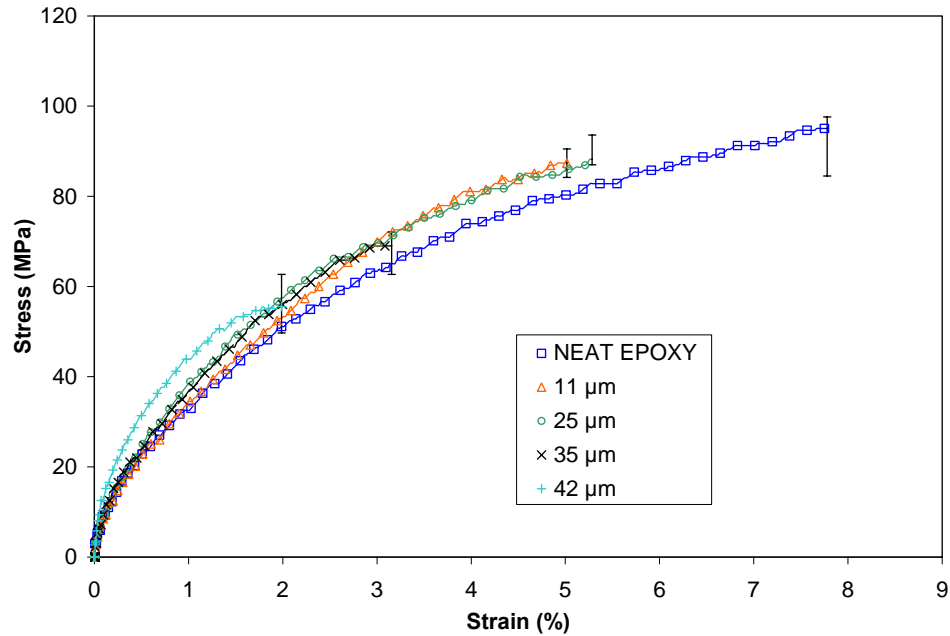
Figure 5.15: Dynamic stress-strain response of 10% volume fraction glass-filled epoxy with different particle sizes (strain rate ≈ 1300 s^{-1})

Qualitatively, the dynamic stress-strain responses for the various particle sizes are very similar in terms of stiffness (Fig. 5.15). Specimens with particle sizes of 11 μm and 25 μm had almost identical stress-strain responses. In terms of peak stresses (values shown in Fig. 5.16), there is a non-monotonic behavior with respect to particle size. Within the experimental error, both 25 μm particle and 11 μm particle specimens have the highest strength. The 35 μm and 42 μm particle specimens had peak stresses that were 22% and 37% respectively lower than the 25 μm particle specimens. It is possible that it truly is a non-monotonic response, such as that observed by Kitey [4], where fracture toughness increased for particle sizes up to 35 μm and decreased thereafter as shown in Fig. 5.16. Since dynamic fracture toughness is a more localized measurement than peak stress, it can be more sensitive to the effect of filler particle size.
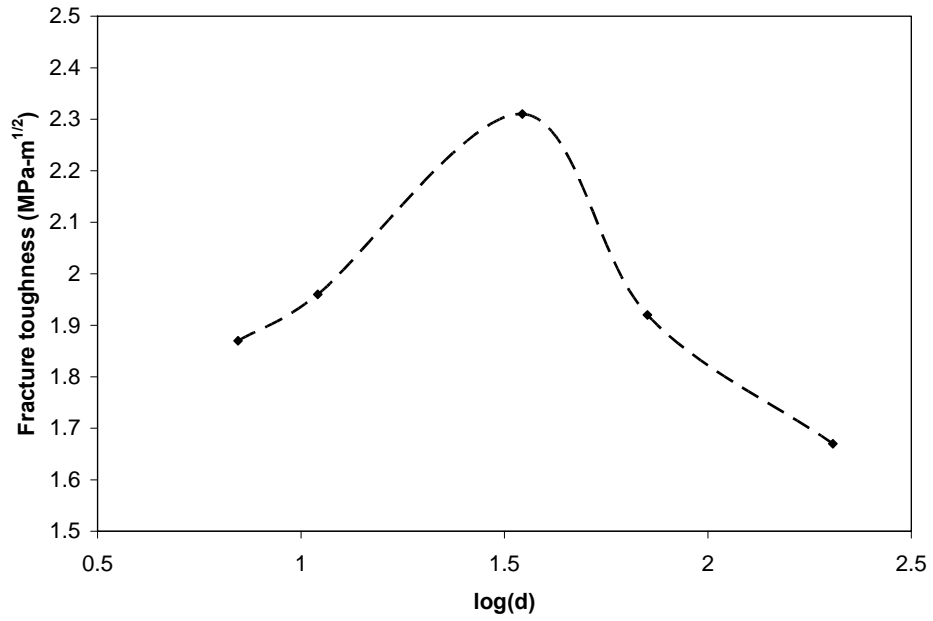
Figure 5.16: Steady state fracture toughness as reported by Kitey [4]
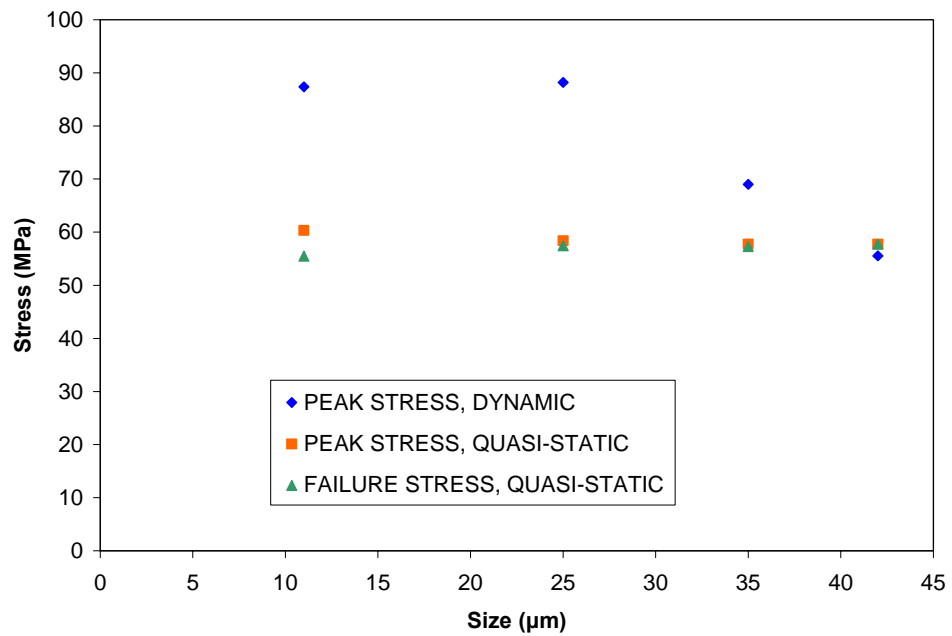
Figure 5.17: Particle size effect on peak and failure stresses (10% filler volume fraction)

However, for this work, the error in the values of peak stresses for the 11 μm and 25 μm specimens overlaps. This could simply be variance in the experiments. Also, the peak stress showed a slight decrease for all particle sizes in the quasi-static case. The only way to be certain is to test a wider range of particle diameters. In the present work, major difficulties were encountered when casting specimens with smaller particles (7 μm) and larger particles (71 μm). In the 7 μm particle case, it was very difficult to prevent particles from coalescing. In the 71 μm particle case, the particles had a tendency to settle due to the lengthy gel time associated with the epoxy system. Addition of modifiers to the epoxy system would certainly make it possible to cast a much broader range of particle sizes; however, this was beyond the scope of the present work.
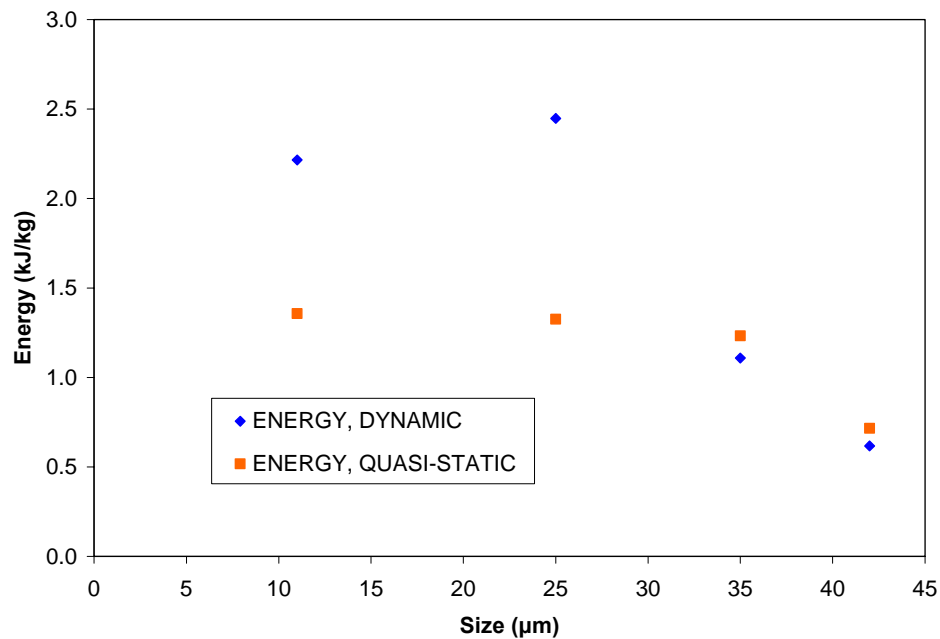
Figure 5.18: Specific energy absorption for different particle sizes (10% filler volume fraction)

Specific energy absorption also decreases with increasing particle size. It is not exactly clear as to why the strength and specific energy have a non-monotonic behavior with particle size. There is some embrittlement associated with the larger particles, even though all of the specimens contained the same volume fraction. There must be additional competing mechanisms causing the unexplained difference.

5.3   Biocements

5.3.1   Introduction and background

A second material of interest in this work is an acrylic-based bone cement. Bone cement is used when a joint in the human body becomes damaged or worn out. In this case, arthroplasty surgery is commonly used to repair, replace, or realign the joint. In recent years, it has become common to surgically replace the joint with a prosthesis. Examples include hip and knee replacements. This is done to relieve pain, to restore range of motion, and to improve walking ability. An acrylic material is often used to anchor the prosthetic components to the existing bone structure as well as remodel portions of the damaged bone. This serves to transfer all stresses between the prosthesis and the living bone. A great deal of research effort has focused on such things as creep, fatigue, and fracture of bone cement. Specifically, the work done in fatigue behavior has been comprehensively reviewed by Krause and Mathis [33] as well as by Lewis [34]. Harper and Bonfield [35] have reported tensile characteristics of different commercially available bone cements. However, little or no work has been done in the area of dynamic tensile behavior. As the understanding of biomechanics and the mechanical performance

of prosthetic components continues to improve, it is more common for patients to return to a highly active lifestyle after surgery. In this case, it is necessary to characterize these biomaterials under the higher strain rates that they will see in service.

5.3.2   Specimen preparation

The biocement studied in the work was Palacos® R which was obtained from Zimmer Orthopaedic Surgical Products and is manufactured by Heraeus Kulzer GmbH. The cement is created by mixing 40 g of a powder containing 33.8 g of poly(methyl acrylate, methyl methacrylate), 5.9 g of zirconium dioxide, and 0.3 g of benzoyl peroxide with 20 mL of a liquid containing 18.4 g of methyl methacrylate. For the first round of experiments, the liquid and powder were mixed at room temperature. In the second set of experiments, the liquid and powder were cooled to 5ºC in an effort to increase cure time and decrease specimen porosity. When the two constituents are mixed, a paste is formed that eventually hardens via an exothermic reaction. For the present work, the dynamic test specimens were cast using the same molds used in the glass-filled epoxy study. The quasi-static specimens were machined from a solid plate of the material.

5.3.3   Results

Harper and Bonfield [35] have reported values for the tensile characteristics of Palacos® R. The results from a batch of 7 tests are listed in Table 5.3. They commented that the cement was mixed in air instead of vacuum, and that this resulted in a varying

amount of porosity. In the present work, it was also observed that mixing the cement in air created a significant amount of porosity. The values of peak stress, failure stress, and failure strain from the quasi-static case were slightly lower than those reported by Harper and Bonfield [35]. No improvement was observed for the pre-chilled specimens.

	Reported by Harper and Bonfield (35)	Present work, quasi-static values
Elastic modulus (GPa)	3.21	2.6
Failure stress (MPa)	51.4	35.3
Failure strain (%)	2.25	2.02

Table 5.3: Quasi-static tensile stress-strain results for Palacos® R bone cement
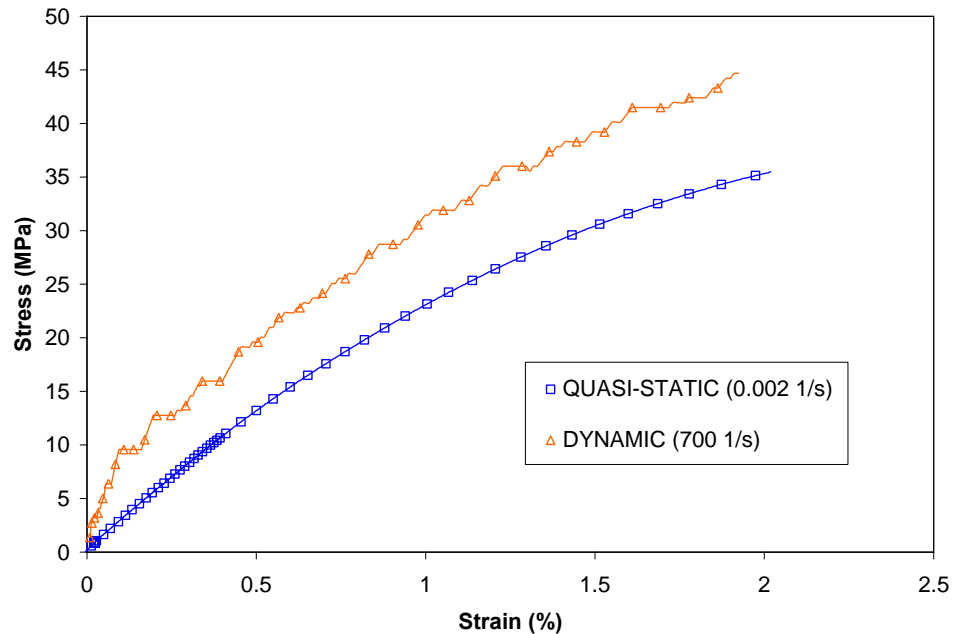
Figure 5.19: Quasi-static and dynamic mechanical response of Palacos® R bone cement

(a)

(b)

Figure 5.20: Broken bone cement specimens (a) quasi-static and (b) dynamic

As is the case with the other thermosetting polymers presented in this work, the higher strain rate loading corresponds to a stiffer response for the bone cement. The dynamic loading also resulted in a higher peak stress, and lower failure strain. Given the low failure strain of the bone cement, there were difficulties in obtaining a specimen that failed under equilibrium and under constant strain rate. The oscillations in the stress-strain response observed in Fig. 5.19 further support this. Material with this behavior is very challenging to test in tension, because as the gage length is reduced (in an effort to decrease equilibration time), the strain rate increases (for a given loading pulse). Thus, the magnitude of the loading pulse must be reduced with the decrease in gage length. For the apparatus used in the present work, this was not feasible.

CHAPTER 6

CONCLUSIONS

6.1   Conclusions

In the present work, a split Hopkinson tension bar was developed to study high strain rate behavior of polymer composites. The apparatus was then used to investigate the effect of filler particle volume fraction on the mechanical response of glass-filled epoxy. Also, an investigation of the effect of particle size on the mechanical response of glass-filled epoxy was undertaken. Lastly, a study of the strain rate effect on the stress-strain response of bone cement was carried out.

The setup was developed through a series of design iterations employing experimental as well as numerical tools to refine the design of the setup. Elastodynamic FE simulations were used in particular to better understand the highly transient nature of the problem. These simulations, coupled with experiments, helped to reach a working setup that could repetitively produce square loading pulses. Once the loading aspects of the setup had been addressed, attention was given to the interaction between the specimen and the apparatus. A dovetail interface was used to attach the specimen to the incident and transmitter bars. This interface allowed for the use of a dogbone style specimen

geometry. This geometry has known value in quasi-static tensile testing. Previous split Hopkinson tension bar setups have not attempted this type of geometry.

Next, a series of experiments were completed using neat epoxy. The neat epoxy system was used to ensure the validity of the experimental results. The results obtained using the apparatus developed in this work were compared with results for the same material found in the open literature. Also, several experiments were conducted under identical conditions to test the setup for repeatability of measurements.

The apparatus was then used to study mechanical response of glass-filled particulate composites. The first part of this study was devoted to the effect of filler particle volume fraction. Tests were carried out with particles of 25 μm mean diameter for filler volume fractions of 0%, 10%, 20%, and 30%. For each volume fraction, specimens were tested at a quasi-static loading rate of approximately 0.002 s^{-1}. Complimentary dynamic specimens were tested at a loading rate of approximately 1300 s^{-1}. The specimens failed in a ductile manner for the quasi-static case, but they failed in a brittle manner in the dynamic case. It was observed that the peak specimen stress increased with filler volume fraction for the static case while it decreased for the dynamic case. At low strain rates, the strain rate and the increase in filler volume fraction independently serve to embrittle the specimen. However, it is possible that at higher strain rates, these two effects become coupled. The results from these experiments were compared with some predictions based on micromechanical modeling. In particular, the elastic modulus values compared reasonably well with values computed using the Mori-Tanaka model. In terms of material strength, several empirical models were applied to the results. One model, suggested by Piggot and Leidner, produced reasonable

99

agreement with the data by selecting the appropriate coefficients. A more sensible curve-fit was then produced for the current data based on the behavior observed.

The second part of this study was devoted to the effect of filler particle size on the mechanical response. The tests were carried out with a volume fraction of 10% for filler particle sizes of 11 μm, 25 μm, 35 μm, and 42 μm mean diameter. All of the specimens were very similar in terms of stiffness; however, there was a non-monotonic behavior in the failure stress. There was a slight increase in failure stress from 11 μm to 25 μm particles and a decrease in failure stress thereafter.

In addition to studying glass-filled epoxies, a brief study was undertaken to observe the effect of strain rate on the stress-strain response of a commercially available bone cement. Palacos® R bone cement was obtained from Zimmer Orthopaedic, Inc. for these tests. The bone cement, which is polymethyl methacrylate (PMMA), has a similar response to the glass-filled epoxies under dynamic loading. The peak stress for the dynamic case is higher than that of the quasi-static case. Also, there is a decrease in the strain value at which the peak stress occurs.

6.2   Future work

This work focused primarily on constructing a framework for dynamic tensile testing. A great deal of effort was required to understand high strain rate testing well enough to produce such a framework. In terms of improvement of the existing apparatus, work could be done to produce a better loading pulse by possibly further examining the effect of striker cross-sectional area on the pulse shape. Also, split Hopkinson bar testing

has constantly been plagued by the inability to accurately identify the beginning of each of the pulses. An algorithm could perhaps be sought out to perform this function.

With the existing apparatus, tests can be done to further understand the effects of glass particles on a polymer matrix. In particular, tests could be conducted at higher filler volume fractions and with a wider range of particle diameters. Also, tests could be conducted on the bone cement to observe the effect of vacuum mixing and quantify its improvement of the mechanical properties. One other possibility is to look at the effect of introducing a filler material into the bone cement.

The apparatus could easily be modified to accept other attachment configurations such as threaded or bonded specimens for materials that are not castable. In general, the framework could be used to test a wide range of low to medium impedance materials.

Also, a compression version of the existing setup can be produced with less effort. Deformation behavior tends to have a wide variation between tension, compression, and shear conditions. The ability to test materials under dynamic compression would be an excellent compliment to the existing framework.

BIBLIOGRAPHY

1. Gray, George T. Classic split Hopkinson bar testing. *ASM Handbook*, 8, Mechanical Testing and Evaluation, 462-476, 2000.

2. Jones, R. M. *Mechanics of Composite Materials*, Second edition. Taylor and Francis, Inc., 1999.

3. Chen, W., Lu, F., and Cheng, M. Tension and compression tests of two polymers under quasistatic and dynamic loading. *Polymer Testing*, 21, 113-121, 2002.

4. Kitey, R. and Tippur, H.V. Dynamic crack growth in particulate bimaterials having discrete and diffuse interfaces: Role of microstructure. *Engineering Fracture Mechanics*, 72, 2721-2743, 2005.

5. Kitey R., *Microstructural effects on fracture behavior of particulate composites: Investigation of toughening mechanism using optical and boundary element methods*, PhD dissertation, Auburn University, 2006.

6. Hopkinson, B. A method of measuring the pressure produced in the detonation of high explosives or by the impact of bullets. *Philosophical Transactions of the Royal Society of London. Series A, Containing Papers of a Mathematical or Physical Character*, 213, 437-456, 1914.

7. Robertson, R. Some properties of explosives. *Journal of the Chemical Society, Transactions*, 119, 1-29, 1921.

8. Landon, J. W. and Quinney, H. Experiments with the Hopkinson pressure bar. *Philosophical Transactions of the Royal Society of London. Series A, Containing Papers of a Mathematical or Physical Character*, 103, 622-643, 1923.

9. Davies, R. M. A critical study of the Hopkinson pressure bar. *Philosophical Transactions of the Royal Society of London. Series A, Mathematical and Physical Sciences*, 240, 375-457, 1948.

10. Kolsky, H. An investigation of the mechanical properties of materials at very high rates of strain. *Proceedings of the Physical Society. Section B*, 62, 676-700, 1949.

11. Pochhammer, L. Uber die Fortpflanzungsgeschwindigkeiten kleiner schwingungen in einem unbegrenzten istropen kreiszylinder. *J. reine angew. Math*, 81, 324-336, 1876.

12. Chree, C. The equations of an isotropic elastic solid in polar and cylindrical coordinates: Their solutions and applications. *Transactions of the Cambridge Philosophical Society*, 14, 250-369, 1889.

13. Love, A. E. H. *Treatise on the Mathematical Theory of Elasticity*. Cambridge, 1927.

14. Bancroft, D. The velocity of longitudinal waves in cylindrical bars. *Physical Review*, 59, 588-593, 1941.

15. Harding, J. and Welsh, L. M. A tensile testing technique for fibre-reinforced composites at impact rates of strain. *Journal of Materials Science*, 18, 1810-1826, 1983.

16. Lindholm, U. S. and Yeakley, L. M. High strain-rate testing: Tension and compression. *Experimental Mechanics*, 8, 1-9, 1968.

17. Nicholas, T. Tensile testing of materials at high rates of strain. *Experimental Mechanics*, 21, 177-185, 1981.

18. Harding, J., Wood, E. O., and Campbell, J. D. Tensile testing of materials at impact rates of strain. *Journal of Mechanical Engineering Science*, 2, 88-96, 1960.

19. Staab, G. H. and Gilat, A. A direct-tension split Hopkinson bar for high strain-rate testing. *Experimental Mechanics*, 31, 232-235, 1991.

20. Ogawa, K. Impact-tension compression test by using a split-Hopkinson bar. *Experimental Mechanics*, 24, 81-85, 1984.

21. Song, B., Chen, W., Yanagita, T., and Frew, D. J. Confinement effects on the dynamic compressive properties of an epoxy syntactic foam. *Composite Structures*, 67, 279-287, 2005.

22. Song, B., Chen, W., Yanagita, T., and Frew, D. J. Temperature effects on dynamic compressive behavior of an epoxy syntactic foam. *Composite Structures*, 67, 289-298, 2005.

23. Buckley, C. P., Harding, J., Hou, J. P., Ruiz, C., and Trojanowski, A. Deformation of thermosetting resins at impact rates of strain. Part I: Experimental study. *Journal of the Mechanics and Physics of Solids*, 49, 1517-1538, 2001.

24. Pan, Y., Chen, W., and Song, B. Upper limit of constant strain rates in a split Hopkinson pressure bar experiment with elastic specimens. *Experimental Mechanics*, 45, 440-446, 2005.

25. Shim, V. P. W., Yuan, J., and Lee, S. H. A technique for rapid two-stage dynamic tensile loading of polymers. *Experimental Mechanics*, 41, 122-127, 2001.

26. Follansbee, P. S. and Frantz, C. Wave propagation in the split Hopkinson pressure bar. *Journal of Engineering Materials and Technology*, 105, 61-66, 1983.

27. Lifshitz, J. M. and Leber, H. Data processing in the split Hopkinson pressure bar tests. *International Journal of Impact Engineering*, 15, 723-733, 1994.

28. Durelli, A. J. *Applied Stress Analysis*. Prentice-Hall, Inc., 1967.

29. ABAQUS™ User's Manual (Version 6.5). ABAQUS Inc., Providence, RI.

30. Ishai, O. and Cohen, L. J. Elastic properties of filled and porous epoxy composites. *International Journal of Mechanical Sciences*, 9, 539-546, 1967.

31. Ishai, O. and Cohen, L. J. Effect of fillers and voids on compressive yield of epoxy composites. *Journal of Composite Materials*, 2, 302-315, 1968.

32. Smith, J. C. The elastic constants of a particulate-filled glassy polymer: Comparison of experimental values with theoretical predictions. *Polymer Engineering and Science*, 16, 394-399, 1976.

33. Krause, W. R. and Mathis, R. S. Fatigue properties of acrylic bone cements: Review of the literature. *Journal of Biomedical Materials Research: Part B, Applied Biomaterials*, 22, 37-53, 1988.

34. Lewis, G. Properties of acrylic bone cement: State of the art review. *Journal of Biomedical Materials Research: Part B, Applied Biomaterials*, 38, 155-182, 1997.

35. Harper, E. J. and Bonfield, W. Tensile characteristics of ten commercial acrylic bone cements. *Journal of Biomedical Materials Research: Part B, Applied Biomaterials*, 53, 605-616, 2000.

36. Weng, G. J. Some elastic properties of reinforced solids, with special reference to isotropic ones containing spherical inclusions. *International Journal of Engineering Sciences*, 22 (7), 845-856, 1984.

37. Ravichandran, K. S. Elastic properties of two-phase composites. *Journal of the American Ceramic Society*, 77 (5), 1178-1184, 1984.

38. Piggott, M. R. and Leidner, J. Misconceptions about filled polymers. *Journal of applied polymer science*, 18, 1619-1623, 1974.

39. Nicolais, L. and Mashalkar, R. The strength of polymeric composites containing spherical fillers. *Journal of applied polymer science*, 20, 561-563, 1976.

40. Schrager, M. The effect of spherical inclusions on the ultimate strength of polymer composites. *Journal of Applied Polymer Science*, 22, 2379-2381, 1978.

APPENDICES

APPENDIX A

MISCELLANEOUS CODE

A.1 Main post processing program (MATLAB®)

```
close all
clear all
clc

%-------------------------------------------------------------------------
%List of experimental parameter
%-------------------------------------------------------------------------
freq = 5e6;                  %Sample rate, Hz
d_al = 0.0127;               %Incident and transmitter bar diameters, m
r_al = d_al/2;               %Bar radius, m
A_al = pi*r_al^2;            %Area of aluminum, m^2
E_al = 71.7e9;               %Young's modulus, Pa
rho_al = 2810;               %Density of aluminum, kg/m^3
C_al = sqrt(E_al/rho_al);    %Wave speed of aluminum, m/s
GF = 2.13;                   %Gage factor
Gch1 = 500;                  %Channel 1 gain
Gch2 = 1000;                 %Channel 2 gain
L_bar = 96*.0254;            %Incident bar length, m
L_b = 10*.0254;              %Bullet length, m
L_bn = (2*L_b/C_al)*freq;    %Loading time in samples
L_g = 31*.0254;              %Gage length from end
pretrig = 5000;              %Pretrigger scans


%-------------------------------------------------------------------------
%Prompt user for various input parameters
%-------------------------------------------------------------------------
s = input('What file do you want to analyze? ','s');
data = load(s);
% w_sp = input('What is the specimen thickness (mm)? ');
w_sp = 1.6;
w_sp = w_sp/1000;
t_sp = input('What is the specimen width (mm)? ');
t_sp = t_sp/1000;
% L_sp = input('What is the gage length of the specimen (mm)? ');
L_sp = 11;
L_sp = L_sp/1000;
A_sp = w_sp*t_sp;
```

107

```
n1 = round(0.8*pretrig);
n2 = n1+round((2*L_bar/C_al)*freq);
n = [n1:n2];
time = [0:(10^6)/freq:(10^6)*(length(n)-1)/freq]';
ch1 = data(n,2);
ch2 = data(n,3);


%------------------------------------------------------------------------
%Identify and separate pulses
%------------------------------------------------------------------------
plot(time,ch1)
t = input('What is the minimum time of the incident signal? ');
t = round(t*(10^-6)*freq);
close all

plot(time,ch1)
u = input('What is the minimum time of the reflected signal? ');
u = round(u*(10^-6)*freq);
close all

plot(time,ch2)
v = input('What is the minimum time of the transmitted signal? ');
v = round(v*(10^-6)*freq);
close all

ch1i = ch1([t:t+3*L_bn]);
ch1r = ch1([u:u+3*L_bn]);
ch1i = ch1i - ch1i(1);
ch2 = ch2([v:v+3*L_bn]);
time = [0:(10^6)/freq:(10^6)*(length(ch1)-1)/freq]';


%------------------------------------------------------------------------
%Calculate strains for all the raw data
%------------------------------------------------------------------------
ch1i_eps = 2.*ch1i./Gch1./GF;
ch1r_eps = 2.*ch1r./Gch1./GF;
ch2_eps = 2.*ch2./Gch2./GF;


%------------------------------------------------------------------------
%Propagate both signals back to the interface
%------------------------------------------------------------------------

%This section of code does not currently do anything, but this is the
%location where the signals could be propagated to the end of the bar
%if it were necessary.

%The subroutine prop.m could be called here

eI = ch1i_eps;
eR = ch1r_eps;
eT = ch2_eps;
eI1 = eI;
eR1 = eR;
eT1 = eT;
```
108

```matlab
eI1 = eI1([1:1+2*L_bn])-eI1(1);
eR1 = eR1([1:1+2*L_bn])-eR1(1);
eT1 = eT1([1:1+2*L_bn])-eT1(1);


time = [0:(10^6)/freq:(10^6)*(length(eR1)-1)/freq]';


%-------------------------------------------------------------------
%Calculate stress, strain, and strainrate for specimen
%-------------------------------------------------------------------
stress_sp = E_al.*A_al.*(eT1)./A_sp;

%Calculate strainrate with 2-wave analysis
strainrate(:,2) = -2.*C_al.*((eT1-eI1))./L_sp;
%Calculate strainrate with 1-wave analysis
strainrate(:,3) = -2.*C_al.*eR1./L_sp;
%Calculate strainrate average of 1- & 2-wave analyses
strainrate(:,1) = -2.*C_al.*(eR1+(eT1-eI1))./L_sp/2;


%Loop to compute strains using basic trapezoidal integration
n = 1;
strain(1,[1:3]) = 0;
while n<length(strainrate)
    n = n+1;
    strain(n,:) = (strainrate(n,:)+strainrate((n-1),:)).*0.5*...
            (1/freq)+strain((n-1),:);
end
strain_all = strain;
strain_all = strain_all.*100;


[pk,loc] = max(stress_sp);
stress = stress_sp*(10^-6);
strain1 = strain_all(:,1);
strain2 = strain_all(:,2);
strain3 = strain_all(:,3);


stress1 = stress([1:1.5*loc]);
strain1 = strain([1:1.5*loc],2);


format long
strain100 = strain1.*100;


%-------------------------------------------------------------------
%Smoothing data (7-point moving average)
%-------------------------------------------------------------------
warning off
avg_strain = zeros(length(strain1),1);
avg_stress = zeros(length(stress1),1);
for r = 4:length(strain1)-3
    ab = strain100([r-3:r+3]);
    cd = stress1([r-3:r+3]);
    avg_strain(r) = mean(ab);
    avg_stress(r) = mean(cd);
end
```

```
%-------------------------------------------------------------------
%Write data to a file
%-------------------------------------------------------------------
dataz = [strain1 strain100 stress1 avg_strain avg_stress avg_strain
avg_stress];
dataz = dataz([1:loc+25],:);
fid = fopen(input('What do you want to name the results file?
','s'),'w');
fprintf(fid,'  Strainrate %6.2f     \n',max(max(strainrate)));
fprintf(fid,'  Strain       Strain(%%)    Stress(MPa)  Strain,Avg
Stress,Avg\n');

for n = 1:length(dataz)
    fprintf(fid,'%12.8f %12.8f %12.8f %12.8f %12.8f %12.8f
%12.8f\n',...

dataz(n,1),dataz(n,2),dataz(n,3),dataz(n,4),dataz(n,5),dataz(n,4),dataz
(n,5));
end
fclose(fid);
```

A.2 Propagation subroutine (MATLAB®)

```
function y = propa(x,f,C_0,r_0,Z_ch)

%---------------------------------------------------------------
%This is a function that given the following variables:
%   x       Signal to be propagated    [Arbitrary Units]
%   f       Sampling frequency         [Hz]
%   C_0     Wavespeed of bar           [m/s]
%   r_0     Radius of bar              [m]
%   Z_ch    Distance to be propagated  [m]
%
%Can be called using the following line of code:
%   y = propa(x,f,C_0,r_0,Z_ch)
%
%This will move the signal along the length of the bar
%by shifting the phase of the particular signal based
%on the velocity-frequency relation given in the files dataz.
%---------------------------------------------------------------

%Read in data from velocity-frequency relationship
%This is to create a 2 column matrix containing one column of
frequencies
%and one column of scale factors for each frequency.  This second
column
%can be multiplied by the bar wave speed to get the plot shown in Ch.
3,
%Figure 3.8

data = load('dataz.txt');
xvals1 = data(:,1);
yvals1 = data(:,2);
freq = f;
Cns = yvals1*C_0;
lams = r_0./xvals1;
ks = xvals1./r_0;
wstart = 50e3;
winc = 4550;
wend = 4.6e6;
d(:,1) = [wstart+winc:winc:wend];   %Frequencies
d(:,2) = Cns;                       %Wave speeds at frequency
d(:,3) = ks;                        %Wave numbers at frequency
T = 400e-6;                         %Period, s
w0 = 2*pi/T;                        %Fundamental frequency, rad/s

%Take forward fft
e1 = (fft(x));
N = length(e1);

%Compute shift values for the positive frequencies
for n = 1:ceil(N/2)
    fr(n) = (1/N)*n*freq;
    if fr(n) <= max(d(:,1))
```

111

```
        Cn(n) = interp1(d(:,1),d(:,2),fr(n));
        if isnan(Cn(n)) == 1
            Cn(n) = C_0;
        else
            Cn(n) = Cn(n);
        end
    else
        Cn(n) = min(d(:,2));
    end
    frR(n) = fr(n)*2*pi;
    shift(n,:) = (frR(n)*Z_ch/C_0)*((C_0/Cn(n))-1);
end

u = ceil(N/2) + 1;
n = ceil(N/2);

%Get shift values for the negative frequencies
while u <= N
shift(u) = shift(n);
u = u+1;
n = n-1;
end

%Compute phase shift in frequency domain
G = cos(shift)+i.*sin(shift);
H = e1.*G;

%Take inverse fft and send it back to main program
y = ifft(H);
```
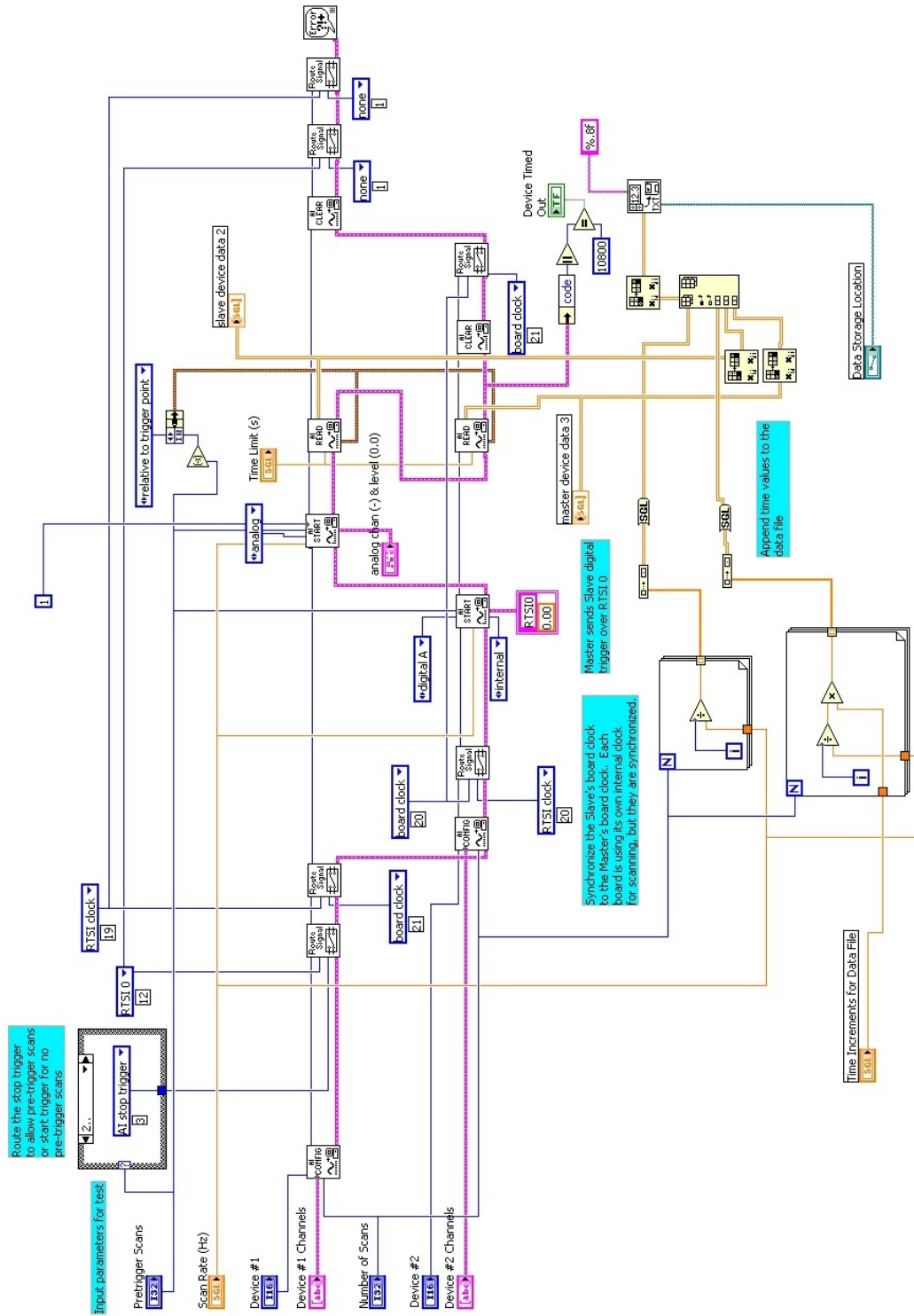
A.4   EDM code and settings

The EDM machine uses G-code, a common programming language used in numerically controlled machines. The master specimen can be machined using a series of linear interpolations (G01's) and circular interpolations (G02's and G03's). G01 is a code that tells the machine to start at the current location of the wire and travel to an endpoint defined relative to the starting point in a linear fashion. G02 is a code that tells the machine to start at the current location of the wire and travel in a clockwise fashion to an endpoint about some centerpoint, both defined relative to the starting point. G03 does the same thing as G02 except that it travels in a counterclockwise fashion. The actual code and machine parameters used are listed in Tables A.1 and A.2. This is for a master specimen with 4 mm gage length. Blocks 1 and 2 are used to index the machine to the desired starting position. Blocks 7 & 15 are used to control the gage length.

Machine Parameter	Value
Speed	3500 (μm/min)
Spark cycle	25
Spark energy	7
Wire speed	7
Wire tension	8
Water conductivity	5
Spark rate	80

Table A.1: EDM machine parameters

Block	Code	Dim.	Value	Dim.	Value	Dim.	Value	Dim.	Value
1	G01	X	0	Y	-6000				
2	G01	X	6000	Y	0				
3	G01	X	0	Y	402				
4	G02	X	3229	Y	2261	I	2406	J	0
5	G01	X	3072	Y	-1118				
6	G03	X	2805	Y	-495	I	2805	J	7708
7	G01	X	4000	Y	0				
8	G03	X	2805	Y	495	I	0	J	8203
9	G01	X	3072	Y	1118				
10	G02	X	3229	Y	-2261	I	823	J	-2261
11	G01	X	0	Y	-803				
12	G02	X	-3229	Y	-2261	I	-2406	J	0
13	G01	X	-3072	Y	1118				
14	G03	X	-2805	Y	495	I	-2805	J	-7708
15	G01	X	-4000	Y	0				
16	G03	X	-2805	Y	-495	I	0	J	-8203
17	G01	X	-3072	Y	-1118				
18	G02	X	-3229	Y	2261	I	-823	J	2261
19	G03	X	0	Y	402				
20	M02								
*All dimensions in microns									

Table A.2: G-code program used in EDM process

APPENDIX B

EXPERIMENTAL PROCEDURES

Prior to conducting experiments, the strain gage signal conditioning unit must be turned on and allowed to warm up for approximately 15 minutes. The zero detector on the unit should also be turned on. All active and compensation strain gages should be checked for proper wiring. At this point, the MultiDAQ virtual instrument should be opened up on the desktop and all experimental parameters should be verified. A file name can be created for the data that will eventually be collected and stored. To prepare each channel of the signal conditioning unit, the channel gain should first be turned to 1 and the RTO adjusted until the lights go off. Next, the channel gain should be turned to 1000 and the RTI adjusted until the lights go off. Then, the channel gain should be set to the desired channel gain. The excitation can then be turned on and the channel balanced until the lights go off. This process should be repeated for each channel. Finally, probes from a volt meter can be inserted into the receptacles on each channel and the incident or transmitter bar can be flexed to check that loading the strain gage produces a voltage change.

Once the data acquisition system is prepared, the hollow bullet should be reloaded to the chamber end of the barrel. The specimen can then be inserted between the two bars. At this time, the alignment at the specimen-bar interface should be carefully

116

examined. Next, the anvil should be pulled in the direction of impact to ensure there is no relaxation in the system. With the bars pulled tight, the anvil should just barely register against the recess in the rubber pad. If not, the clamp on the free end of the transmitter bar should be adjusted appropriately. The gas gun chamber should then be charged to the appropriate pressure. Once all of these items are completed, a few rechecks should be completed. The anvil end of the incident bar should be checked for tightness. The balance of the strain gage should be adjusted once again. Finally, the chamber pressure should be checked and adjusted if necessary.

Once these steps have been taken, the system is prepared for the test. The arrow in the virtual instrument should be clicked to run the program. Once clicked, the program waits for the appropriate trigger conditions to be met. The solenoid valve should be activated immediately. Upon impact, the data will be collected and stored on the desktop for post processing using the MATLAB® code listed in App. A.

APPENDIX C

FEASIBILITY STUDY OF AN ALTERNATIVE METHOD

C.1   Introduction

Prior to designing the split Hopkinson tension bar, a potential alternative method was examined for studying dynamic stress-strain response. The concept uses a fixture shaped like the Greek letter θ to apply a dynamic tensile load to a test specimen. An elastodynamic finite element model coupled with experimental work was used to study the feasibility of this method.

C.2   Initial design considerations

Several design criteria must be met in order to test materials at high rates of strain. The apparatus must be capable of applying a completely uniaxial load. The time duration of the load must be adequate for the specimen to achieve equilibrium. Also, the load must produce sufficient strains in the specimen to cause failure. The strain history experienced by the specimen must be linear in nature to result in a constant strain rate.

In order to meet these criteria, a shape was chosen that was initially introduced by Durelli [28]. Durelli developed a specimen that was in the shape of the Greek letter, θ as

shown in Fig. C.1. When an external compressive load is applied to the specimen, the central web undergoes a tensile deformation. Durelli used this shape to study static stresses and strains of a photoelastic material. For the static case, the forces experienced in the web are directly related to the applied compressive forces. Thus, the stress-strain response in the specimen can be found by measuring the strain directly on the specimen and calculating the stress based on the applied load. This is an attractive option because as the load increases, the configuration becomes progressively more stable. The question is whether or not this can be adapted to study dynamic material response.
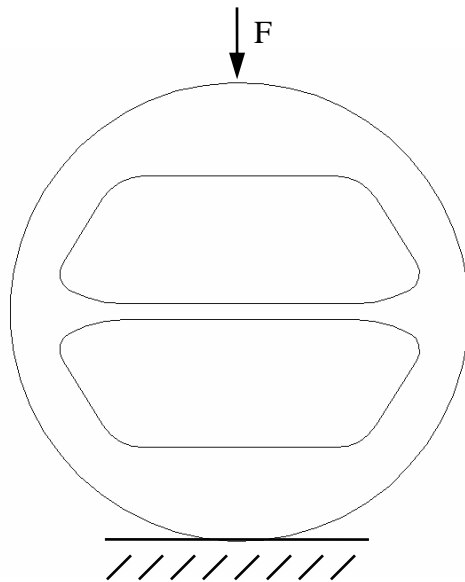

Figure C.1: Durelli's "theta" specimen

C.3   Feasibility study

In the dynamic scenario, it is very difficult to apply equal and opposite loads to this configuration simultaneously. Preliminary elastodynamic finite element simulations suggested that when the load is applied asymmetrically, or when the load at the top is not synchronous with the load at the bottom, the central web tends to oscillate and produce flexural deformations. A series of simulations were done in an effort to design a fixture that would produce a uniaxial load in the central web from an asymmetric external load. The simulations were also used to determine if the fixture could be constructed of a material such as aluminum and could accept a specimen of another material type.

C.3.1   Finite element simulations

The geometry was modeled in Solid Edge®. An initial graphics exchange specification (IGES) file was used to transform the geometry into a neutral one that could be interpreted by ANSYS®. This file was loaded into ANSYS® and adjusted to be a 2-dimensional model. The model was meshed using quadrilateral plane stress elements (PLANE 82). These were chosen for their ability to represent curved boundaries and ability to be very irregularly shaped without adversely affecting the results. A flow-through mesh was used at the boundary between the fixture and the specimen in order to avoid the complexities associated with modeling contact. A preliminary experiment was conducting using a drop tower to determine a typical force history. An aluminum beam

was placed in the drop tower, and impacts were conducted at various velocities. The recorded tup force history is shown in Fig. C.2.
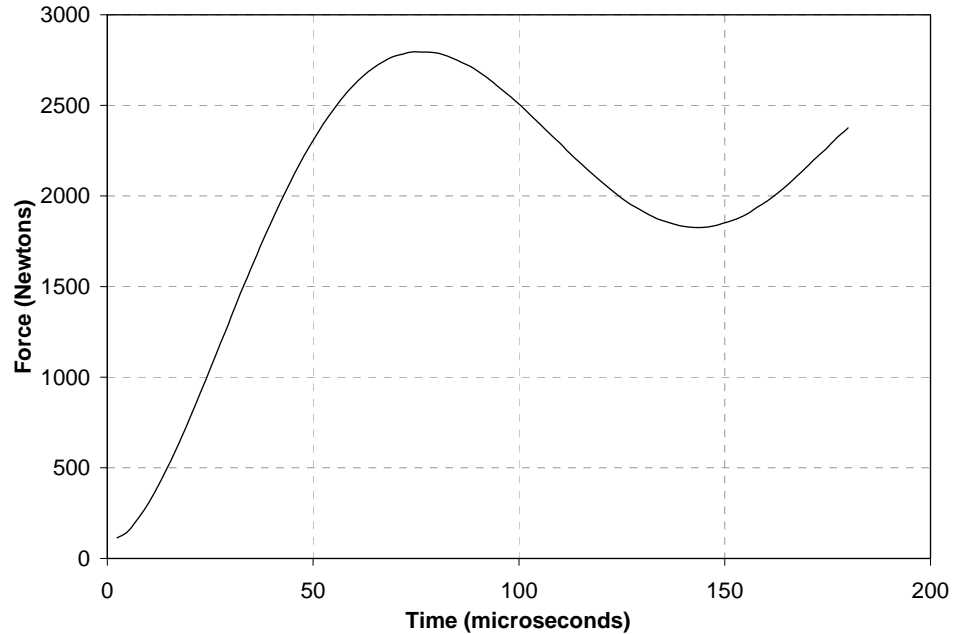

Figure C.2: Tup force history

Once the tup force history was determined, various geometries were studied. In the model, no boundary conditions were used in order to simulate the inertial nature of the experiment. The first iteration was the exact theta shape used by Durelli but modified to accept a different material in the web.

Figures C.3 and C.4 show design iteration #1. In the plot, the stress versus time is shown at the bottom and top of the central web on the vertical line of symmetry. It is evident that the stress is briefly uniaxial, but after a short time, the oscillations begin. Thus, there is a considerable amount of bending stress.
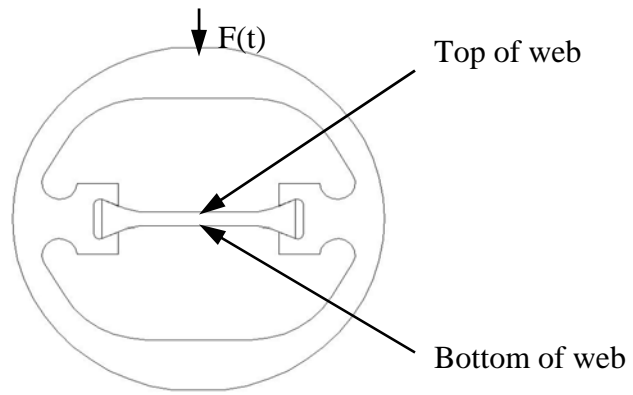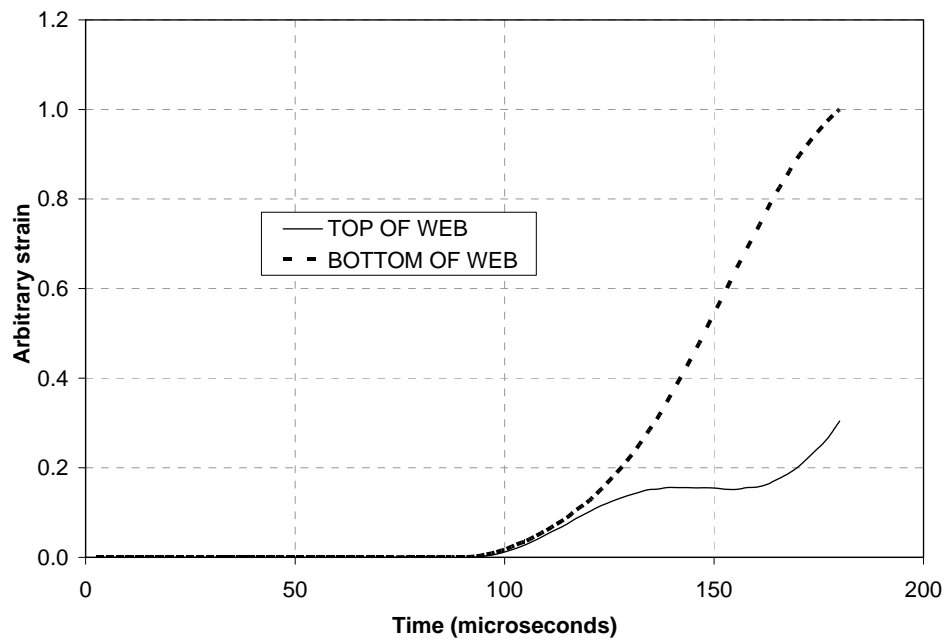
121

Figure C.3: Design iteration #1

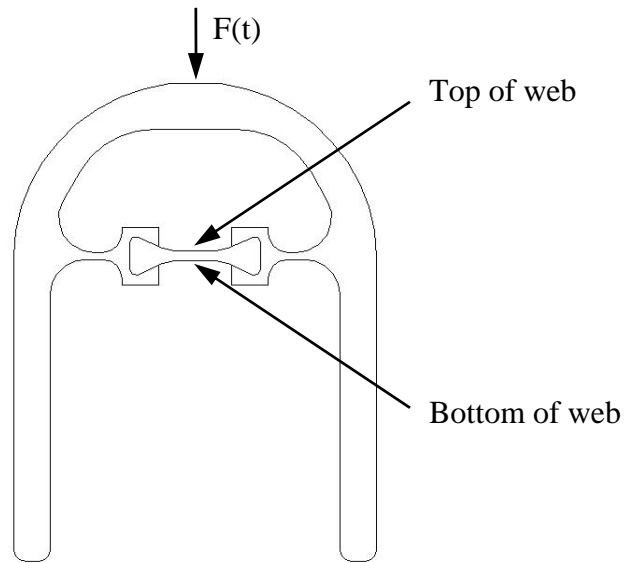Figure C.4: FE results for iteration #1
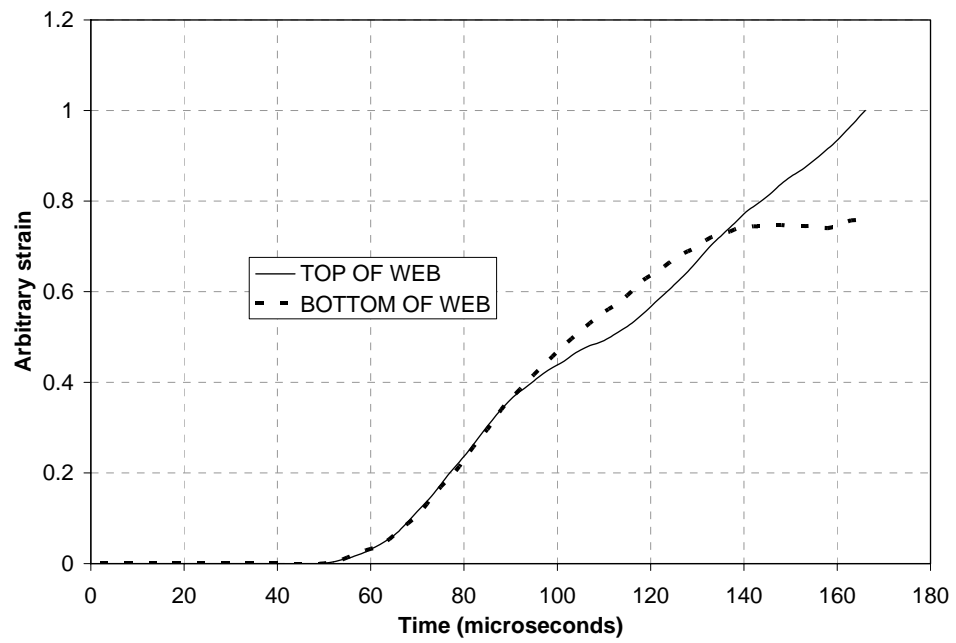
122

Figure C.5: Final design iteration

Figure C.6: FE results for final design iteration

123

After a thorough series of design iterations, the shape (shown in Fig. C.5) was capable of sustaining a near-uniaxial load for approximately 80 microseconds. Instead of the original vertically symmetric shape, the last iteration had two legs, more like the shape of an A. Since there is a discontinuity at the interface between the specimen and the fixture, there are reflected waves. The legs allow these reflected waves to propagate away from the specimen. By the time the waves reach the supports, the specimen has already failed, thus not allowing the supports to play a role in the loading.

C.3.2   Experimental procedure

Once a suitable geometry was found in the simulation process, it was machined from 6061-T651 aluminum alloy. This material gave adequate strength and stiffness properties to test the pure epoxy specimens in the initial phases of the method development. In addition, the elastic impedance of the fixture was not too largely mismatched from that of the specimen. This ensures that most of the energy is transmitted from the fixture to the specimen. To fabricate the specimen itself, the aluminum fixture was used as a mold, and the epoxy was poured directly into it. Once, cured, the epoxy was removed and machined to the proper dimensions.
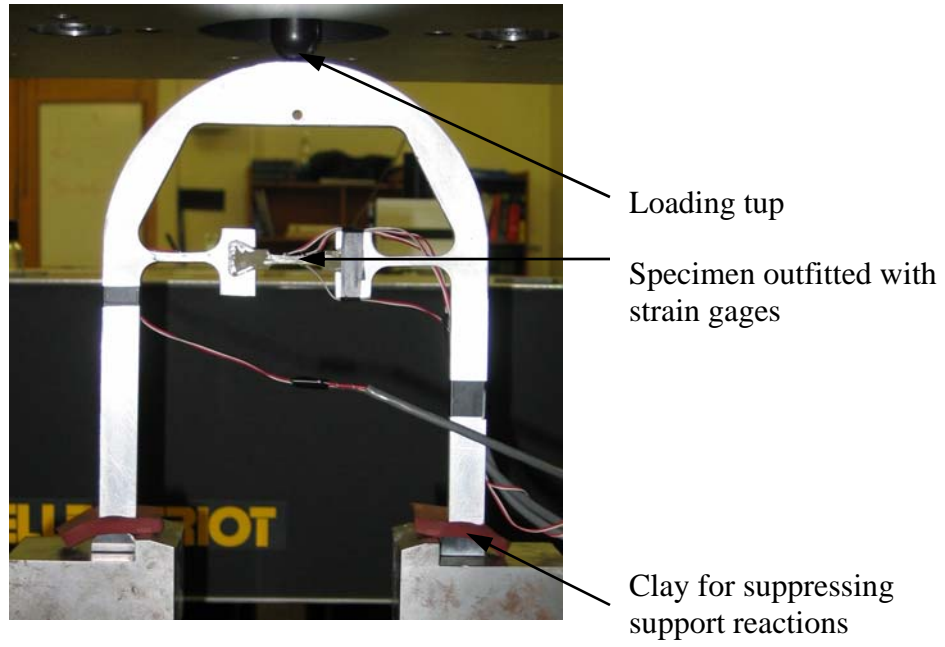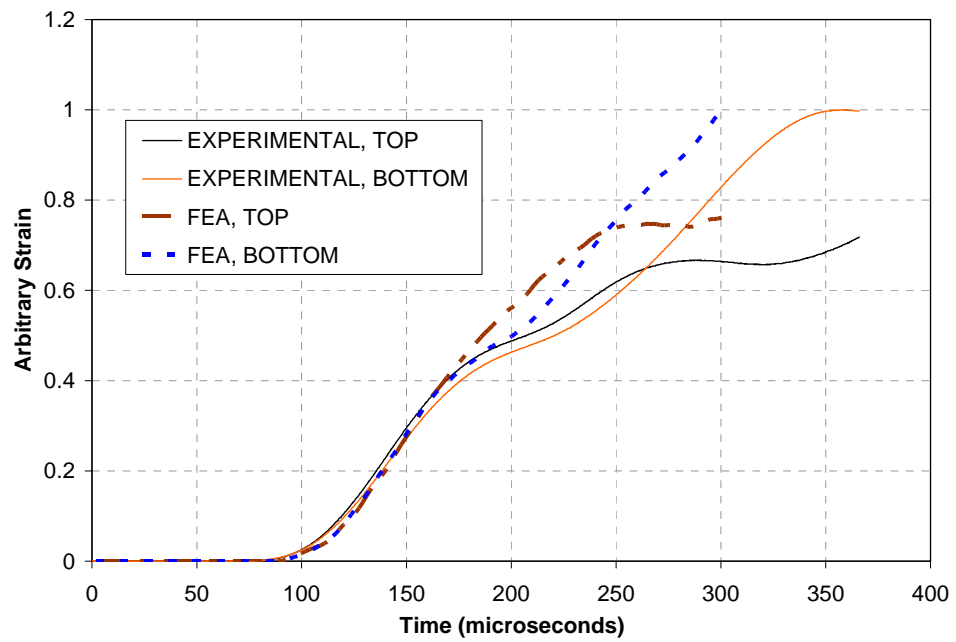
Figure C.7: Fixture and specimen

Figure C.8: Experimental comparison with FEA

125

Good agreement was observed between the experimental and the simulated tests for the initial 100 microseconds as seen in Fig. C.8. Several aspects of this geometry that were notable include that it maintained linearity for a considerable amount of time (>80 microseconds). It also maintained a uniaxial state of stress for a considerable amount of time (>80 microseconds).

C.4   Limitations

In order to fully characterize a material, it is necessary to measure the stress as well as strain. While the strain can be measured directly on the specimen, there is currently no clear way to measure the specimen stress in this configuration. The impedance mismatch between the fixture and the specimen makes it difficult to know exactly how much stress is transmitted at the interface between the grip and the specimen. Thus, the tup load cannot be used to compute stress. One potential technique for measuring stress is measuring surface particle velocities. The stresses can be computed based on the particle velocities using the relationship $\sigma = \rho C V$. The disadvantage of this is that it requires expensive optical equipment to implement. Also, there are uncertainties associated with the calculation of the elastic wave speed, C.

C.5   Conclusions

It has been demonstrated that this could potentially load a specimen at a constant rate of strain for a suitable duration of time. Based on the reasonable agreement in the

trends of the simulated versus experimental data, this model could further be studied to obtain a more optimal shape given the desired criteria. Even though there are currently shortcomings in the ability to measure stress, this overall concept could be an attractive load fixture for studying dynamic stress-strain response because of its ease of implementation.